

Microfluidic and X-ray techniques for investigations of nanoparticle nucleation and growth

DISSERTATION

zur Erlangung des akademischen Grades
einer Doktorin der Naturwissenschaften (Dr. rer. nat.)
in der Bayreuther Graduiertenschule für Mathematik und Naturwissenschaften
(BayNAT)
der Universität Bayreuth

vorgelegt von

Maria Herbst, M.Sc.

aus Berlin

Bayreuth, 2019

Die vorliegende Arbeit wurde in der Zeit vom 01. Oktober 2014 bis zum 30. April 2017 am Lehrstuhl für Physikalische Chemie I der Universität Bayreuth und vom 01. Mai 2017 bis zum 30. Juni 2019 am Institut für Neutronenstreuung und Weiche Materie (JCNS-1/ICS-1) am Forschungszentrum Jülich unter der Betreuung von Prof. Dr. Stephan Förster angefertigt.

Vollständiger Abdruck der von der Bayreuther Graduiertenschule für Mathematik und Naturwissenschaften (BayNAT) der Universität Bayreuth genehmigten Dissertation zur Erlangung des akademischen Grades einer Doktorin der Naturwissenschaften (Dr. rer. nat.).

Dissertation eingereicht am:	15.08.2019
Zulassung durch das Leitungsgremium:	08.10.2019
Wissenschaftliches Kolloquium:	25.11.2020
Amtierender Dekan:	Prof. Dr. Markus Lippitz

Prüfungsausschuss:

Prof. Dr. Stephan Förster	(Erstgutachter)
Prof. Dr. Markus Retsch	(Zweitgutachter)
Prof. Dr. Birgit Weber	(Vorsitz)
Prof. Dr. Seema Agarwal	

- Für meine Kinder -

Summary

The present work deals with *microfluidic and X-ray techniques for investigations of nanoparticle nucleation and growth*. Mainly during this work, the nucleation and growth kinetics of nanoparticles were investigated. Furthermore, microfluidic chips were developed and fabricated to observe medical and biological processes in vitro under dynamic conditions. The focus of this thesis is on the kinetic studies of zinc oxide and palladium nanoparticles, which were performed in situ during the respective synthesis. This was done partly by a combination of microfluidic systems with analytical methods, which include X-ray scattering and optical spectroscopy.

The first part of this work involves the investigation of the nucleation and growth kinetics of zinc oxide nanoparticles using in situ SAXS / WAXS / UV-Vis experiments. Here, the synthesis of Ehlert et al. was transferred to a microfluidic system using the thermal decomposition reaction of zinc oleate.

First, an experimental setup was developed that allows one to set the desired reaction temperature and to apply as many as possible parallel analysis and characterization methods during nanoparticle synthesis. In this way, the nucleation and growth kinetics of these amorphous zinc oxide nanoparticles were investigated by means of small angle X-ray scattering, wide-angle X-ray scattering and UV-Vis spectroscopy at a synthesis temperature of 40 °C and 50 °C.

There were problems in carrying out the fluorescence spectroscopy measurements parallel to the X-ray scattering methods. Even in a completely darkened room, the measurement results were disturbed and falsified by the warning lamp of the X-ray scattering apparatus, and therefore the fluorescence data in the evaluation had to be omitted.

The data from the kinetic study showed that the growth rate and the particle size increase with increasing temperature. As an additional characterization method, the transmission electron microscope was used to study the nanoparticles after synthesis in terms of their particle size and shape.

The second part of the thesis deals with the investigation of the growth kinetics of palladium nanoparticles by small angle X-ray scattering. Since the solvent - oleylamine - of this nanoparticle synthesis is compatible with PDMS, it was planned to transfer the synthesis of Sun et al. to a microfluidic system.

Initial preliminary experiments in two-dimensional PDMS glass microfluidic chips have successfully led to monodisperse, spherical palladium nanoparticles. But there was a problem with the exact temperature control during the synthesis. Because of this, the same experimental setup should be used like in the microfluidic synthesis of the zinc oxide nanoparticles.

Gas formation during synthesis interfered with the continuous uptake of palladium nanoparticle growth by in situ SAXS measurements. As a result, classical flask synthesis has been scaled down to a "closed quartz capillary synthesis" in order to lose as little data as possible.

The palladium nanoparticle synthesis according to Sun et al. was carried out at two different reaction temperatures (70 °C and 90 °C) in a heating cell of Linkam at the Synchrotron Petra III/DESY in Hamburg at the beamline P03. The concentration of BTB and the heating rate were changeable factors during the experiments. It could also be shown here that an increase in the reaction temperature leads to an increase in the growth rate and the particle size.

Nevertheless, it turned out that the heating rate has no significant influence on the size of the palladium nanoparticles or their growth rate. In addition, it was possible to observe that a reduction in concentration leads to an increase in the growth rate. The transmission electron microscope was also used in these experiments as an additional characterization method for determining the particle shape and size.

The third and last part of this thesis deals with the development of complex microfluidic biochips to investigate blood agglomeration and biosynthesis of platelets.

During a cooperation between the working group of Prof. Dr. S. Förster, the research group of Dr. M. Bender (Experimental Biomedicine, University Hospital Würzburg) and Prof. Dr. S. Gekle (Theoretical Physics, University of Bayreuth) two-dimensional microfluidic chips made from PDMS and glass were designed, developed and produced in order to perform stenosis experiments on the one hand and closely observe the formation of megakaryocytes in platelets in so-called bioreactors on the other hand. The microfluidic chips made it possible to perform these experiments in vitro under dynamic conditions.

The medical and biological analyses of the experiments, which were partly done together, are being carried out by Ruth Kranz in her doctoral thesis.

Zusammenfassung

Die vorliegende Arbeit behandelt *mikrofluidische und Röntgentechniken zur Untersuchung Nanopartikeln hinsichtlich des Keimbildungs- und Wachstumsprozesses*. Einerseits wurden die Keimbildungs- und Wachstumskinetik von Nanopartikeln untersucht, andererseits wurden Mikrofluidik-Chips entwickelt und angefertigt, um medizinische und biologische Prozesse in vitro unter dynamischen Bedingungen zu beobachten. Der Fokus dieser Doktorarbeit bezieht sich auf die kinetischen Untersuchungen von Zinkoxid- und Palladium-Nanopartikeln, die in situ während der jeweiligen Synthese durchgeführt wurden. Dies wurde zum Teil durch eine Kombination von mikrofluidischen Systemen mit analytischen Methoden, zu denen Röntgenstreuung und UV-Vis-Spektroskopie gehören, umgesetzt.

Der erste Teil dieser Arbeit beinhaltet die Untersuchung der Keimbildungs- und Wachstumskinetik von Zinkoxid-Nanopartikeln mit Hilfe von in situ SAXS/WAXS/UV-Vis - Experimenten. Hierbei wurde die Synthese von Ehlert et al. unter Verwendung der thermischen Zersetzungsreaktion von Zinkoleat auf ein mikrofluidisches System übertragen. Zuerst wurde ein experimenteller Aufbau entwickelt, der es einem ermöglicht die gewünschte Reaktionstemperatur einzustellen und möglichst viele parallel zueinander durchzuführenden Analyse- und Charakterisierungsmethoden während der Nanopartikelsynthese anzuwenden.

Auf diese Weise konnten die Keimbildungs- und Wachstumskinetik dieser amorphen Zinkoxid-Nanopartikel bei einer Synthesetemperatur von 40°C und 50°C mittels Röntgenkleinwinkel- und Röntgenweitwinkelstreuung, sowie der UV-Vis-Spektroskopie untersucht und ausgewertet werden. Neben der Temperatur wurde auch die Konzentration des Zinkoleats bei den durchgeführten Experimenten variiert.

Probleme gab es bei den Messungen der Fluoreszenzspektroskopie parallel zu den Röntgenstreuungsmethoden. Selbst in einem völlig abgedunkelten Raum, wurden die Messergebnisse durch die Warnlampe der Röntgenstreuungsapparatur gestört und verfälscht, weshalb auf die Fluoreszenzdaten bei der Auswertung verzichtet werden musste.

Mit den Daten der kinetischen Untersuchung konnte gezeigt werden, dass mit steigender Temperatur die Wachstumsgeschwindigkeit und die Partikelgröße zu nimmt. Als zusätzliche Charakterisierungsmethode diente das Transmissionselektronenmikroskop, mit dem die Nanopartikel nach der Synthese hinsichtlich ihrer Partikelgröße und -form untersucht worden sind.

Der zweite Teil der Doktorarbeit befasst sich mit der Untersuchung der Wachstumskinetik von Palladium-Nanopartikeln mittels Röntgenkleinwinkelstreuung. Da das Lösungsmittel – Oleylamin – dieser Nanopartikelsynthese kompatibel mit PDMS ist, war es geplant die Synthese von Sun et al auch auf mikrofluidische Chips zu übertragen. Erste Vorversuche in zweidimensionalen PDMS-Glas-Mikrofluidik-Chips führten erfolgreich zu monodispersen, sphärischen Palladium-Nanopartikeln.

Es gab jedoch ein Problem bei der exakten Temperaturkontrolle während der Synthese. Aufgrund dessen sollte der gleiche experimentelle Aufbau wie bei der mikrofluidischen Synthese der Zinkoxid-Nanopartikel verwendet werden. Gasbildung während der Synthese störte jedoch die kontinuierliche zeitliche Aufnahme des Wachstums der Palladium-Nanopartikel mittels in situ SAXS-Messungen. Aufgrund dessen wurde die klassische Kolbensynthese runterskaliert zu einer „Synthese in einer geschlossenen Quarz-Kapillare“, um möglichst wenige Daten zu verlieren.

Die Palladium-Nanopartikelsynthese nach Sun et al. wurde bei zwei unterschiedlichen Reaktionstemperaturen (70°C und 90°C) in einer Heizzelle von Linkam am Synchrotron Petra III/DESY in Hamburg an der Beamline P03 durchgeführt. Die Konzentration von BTB und die Heizrate waren veränderbare Faktoren während der Experimente.

Es konnte hier ebenso gezeigt werden, dass eine Erhöhung der Reaktionstemperatur zu einem Anstieg der Wachstumsgeschwindigkeit und der Partikelgröße führt. Es stellte sich jedoch heraus, dass die Heizrate keinen merklichen Einfluss auf die Größe der Palladium-Nanopartikel oder deren Wachstumsrate hat.

Zudem konnte die Beobachtung durchgeführt werden, dass eine Verringerung der Konzentration zu einer Erhöhung der Wachstumsgeschwindigkeit führt. Das Transmissionselektronenmikroskop diente auch bei diesen Experimenten als zusätzliche Charakterisierungsmethode zur Bestimmung der Partikelform und -größe.

Der dritte und letzte Teil dieser Arbeit befasst sich mit der Entwicklung komplexer mikrofluidischer Biochips zur Untersuchung der Blutagglomeration und Biosynthese von Blutplättchen.

Während einer Kooperation zwischen dem Arbeitskreis von Prof. Dr. S. Förster, der Arbeitsgruppe von Dr. M. Bender (Experimentelle Biomedizin, Universitätsklinikum Würzburg) und Prof. Dr. S. Gekle (Theoretische Physik, Uni Bayreuth) wurden zweidi-

mensionale Mikrofluidik-Chips aus PDMS und Glas design, entwickelt und angefertigt, um einerseits Stenose-Experimente durchzuführen und andererseits in sogenannten Bioreaktoren die Bildung von Megakaryozyten zu Thrombozyten näher zu beobachten. Die mikrofluidischen Chips ermöglichen es, diese Experimente in vitro unter dynamischen Bedingungen durchzuführen.

Die medizinische und biologische Analyse der auch zum Teil gemeinsam durchgeführten Versuche wird durch Ruth Kranz in ihrer Doktorarbeit vorgenommen.

Glossary

a.u.	arbitrary unit
BSA	bovine serum albumin
BTB	borane tert-butylamine complex
c_{crit}	critical concentration
c_{sat}	saturation concentration
equ.	equation
GFP	green fluorescent protein
HEPES	4-(2-hydroxyethyl)-1-piperazineethanesulfonic acid
IR	infra red
Oam	oleylamine
$\text{Pd}(\text{acac})_2$	palladium acetylacetonate
PDMS	polydimethylsiloxane
prec	precursor
rel.	relative
SAXS	small angle X-ray scattering
t	time
T	temperature
ΔT	heating rate
TBAH	tetrabutylammonium hydroxide
TEM	transmission electron microscopy
THF	tetrahydrofuran
UV-Vis	ultraviolet-visible
VWF	von Willebrand factor
WAXS	wide angle X-ray scattering

Contents

Summary	I
Zusammenfassung	III
Glossary	VI
1 Introduction	1
1.1 Motivation and aim of this thesis	2
1.2 Organization of this thesis	4
2 Theoretical Fundamentals	5
2.1 Nanoparticles	5
2.1.1 Production of Nanoparticles	5
2.1.2 Nucleation and Particle growth	6
2.1.2.1 LAMER Model	6
2.1.2.2 Thermodynamics of nucleation	8
2.1.2.3 Kinetics of the nanoparticle formation reaction	10
2.1.3 Semiconductor Nanoparticles	12
2.1.4 Metal Nanoparticles	14
2.2 Microfluidics	15
2.2.1 Physicle basics	15
2.2.2 Microfluidic devices	16
2.2.3 Microfluidic nanoparticle synthesis	18
2.2.3.1 Mixing in microfluidic channels	19
2.2.3.2 Fick's laws of Diffusion	20
2.2.4 Bio fluid mechanics	22
2.3 Investigation methods of nano- and microstructures	23
2.3.1 X-ray Scattering	23
2.3.1.1 Physical Basics of X-ray Scattering	24
2.3.1.2 Scattering Intensity of Isotropic Systems	26
2.3.1.3 Form Factor	27
2.3.1.4 Fractal Structures	28
2.3.2 Transmission Electron Microscopy	29
2.3.2.1 Physical Basics of the TEM	29
2.3.2.2 Construction of the TEM	30
2.3.3 UV-Vis spectroscopy	31

3	Results and Discussion	33
3.1	Investigation of nucleation and growth kinetics of ZnO nanoparticles by in situ SAXS/WAXS/UV-Vis-experiments	33
3.1.1	Microfluidic synthesis of ZnO nanoparticles	33
3.1.2	Development of the experimental construction	34
3.1.3	Small Angle X-ray Scattering	37
3.1.4	Nucleation and growth model	44
3.1.5	Crystallinity	48
3.1.6	UV-Vis spectroscopy	51
3.1.7	Transmission electron microscopy	53
3.2	Investigation of the growth kinetics of Pd nanoparticles by in situ SAXS-experiments	55
3.2.1	Synthesis of Pd nanoparticles	55
3.2.2	Development of the experimental construction	56
3.2.3	Small Angle X-ray Scattering	59
3.2.4	Nucleation and growth model	66
3.2.5	Transmission electron microscopy	70
3.3	Development of microfluidic chips for studying biological and medical processes	72
3.3.1	Design development and producing of microfluidic chips for performing and monitoring thrombus formation	72
3.3.1.1	Description of the experiments	72
3.3.1.2	Discussion of the results	73
3.3.2	Design development and production of microfluidic bioreactors	80
3.3.2.1	Description of the experiments	80
3.3.2.2	Discussion of the results	81
4	Conclusion and future perspective	85
5	Experimental Methods	88
5.1	Materials	88
5.2	Synthesis regulations	88
5.2.1	Zinc oxide nanoparticles	88
5.2.1.1	Syntheses of zinc oleate	88
5.2.1.2	Syntheses of zinc oxide nanoparticles	89
5.2.2	Palladium nanoparticles	89
5.3	Microfluidic device fabrication	90
5.3.1	Production of moldings by Photolithography	90

5.3.2	Production of channel structure templates by softlithography	91
5.3.3	Device handling	91
5.3.4	Producing of heating foils	92
5.4	Instrumentation	93
5.4.1	Microfluidic SAXS/WAXS/UV-Vis - Ganesha	93
5.4.2	Synchrotron Small-Angle X-ray Scattering	93
5.4.3	SAXS/WAXS Data Analysis	93
5.4.4	3D-printing	94
5.4.5	Transmission Electron Microscopy	94
5.4.6	Optical microscopy	94
5.4.7	Infrared camera	94
	References	95
	List of Figures	103
	List of Tables	109
	Scientific Contributions	110
	Acknowledgements	111
	Declaration/Eidesstattliche Erklärung	113

1 Introduction

Aggregation is an accumulation of two or more individual atoms or molecules.^[1,2] Their formation is a fundamental assembly process governed by principles in the nanometer to the micrometer length scale and their understanding is of great interest. The investigation of these principles requests the combination of advanced analysis techniques that extend into the relevant length scales.^[3] For this purpose, X-ray scattering methods and microfluidic techniques have been primarily used during this thesis.

X-ray scattering is an analysis and characterization method. It is distinctive in its ability to investigate materials in real time and under realistic sample environments, enabling researchers to understand morphology at nanometer and angstrom length scales using complementary small and wide angle X-ray scattering (SAXS, WAXS), respectively.^[4]

Microfluidics is the science and technology that deals with systems of very small volumes of liquids (10^{-9} to 10^{-18} litres), using channels in the size range of 10 μm to 100 μm .^[5] Microfluidics embraces not only the study of micro systems, but also the design, fabrication and application of so-called chip laboratories (lab-on-a-chip). These are used to study microfluidic systems that have been developed, for example in chemistry, medicine and biology.^[6]

In the field of chemistry in recent years, research of nanoparticle synthesis in microfluidic systems has increased.^[7-10] Some of the advantages of microfluidics in nanoparticle syntheses are significantly smaller amount of chemicals and much easier controllable reaction conditions. In comparison to classical flask synthesis, microfluidics offers benefits in terms of a better control of particle size, size distribution, crystal structure and the shape of nanoparticles.^[7] In addition microfluidic is a method which allows studying fast chemical reactions, including nanoparticle syntheses, in millisecond time scale.^[11]

Nanoparticles feature some unique physicochemical properties due to their size, shape and structure, for example quantum size effect, interface effect, and large specific surface. In the past decades they also have shown extensive industrial applications in new energy, catalysis, optoelectronic information, high-density magnetic recording media and sensors, particularly for metallic and semiconductor nanoparticles.^[12-14]

Because of the importance of nanoparticles, investigations of their nucleation and growth kinetics have motivated several studies by different research groups. Despite this increased interest a broad understanding of the formation mechanism of nanopar-

ticles starting from the precursor reaction with subsequent nucleation and growth is still an interesting and challenging question.^[15] For a better understanding and investigation of these processes, microfluidics is a good opportunity to enable performing nanoparticle syntheses and applying simultaneous analysis and characterization methods.

In biology and medicine, microfluidics is becoming more and more important. Analysis techniques with a very high throughput, high sensitivity and resolution have been needed. Microfluidics offers this possibility.

In the 1990s, the Defense Advanced Research Projects Agency (DARPA) of the US Department of Defense supported a number of programs to develop field-deployable microfluidic systems to serve as detectors for chemical and biological weapons.^[5]

Also the number of patients requiring a blood transfusion increases. So far, only humans can serve as donors. Microfluidics provides the ability to model human bone marrow composition systems to obtain platelets procurement in vitro to meet the growing need for transfusion.^[16-18]

1.1 Motivation and aim of this thesis

This present thesis includes the in situ investigation of the nucleation and growth kinetics of zinc oxide and palladium nanoparticles by different analyze and characterization methods (first and second part of this work) as well as the development and fabrication of microfluidic chips for studying biological and medical processes (third part of this work).

The first part of this work deals with the nucleation and growth kinetics of amorphous zinc oxide nanoparticles according to the high temperature synthesis method of Ehlert *et al.*^[19] Zinc oxide nanoparticles belong to the semiconductor nanoparticles which have, due to their properties, numerous application possibilities and have therefore been intensively researched over the past decades.

One of the most important attribute is the increase of the band gap by decreasing the particle size. Fundamental theoretical understanding of the size-dependent properties of zinc oxide nanoparticles and different syntheses of monodispersed semiconductor nanoparticles has been published in large numbers.^[19-21]

In recent years, new methods of investigations have been developed to study the classical theories, such as nucleation theory, experimentally. This includes the simultaneous investigation of nanoparticles by in situ small- and wide-angle X-ray diffraction (SAXS, WAXS) as well as in situ UV-Vis spectroscopy to receive information about the nucleation and growth of the nanoparticles just as knowledge about the energetically structure.^[15,22-24]

During this work amorphous zinc oxide nanoparticle in dilute solution in view of nucleation and growth of these semiconductor particles and their energetically changes by time-resolved in situ small- and wide-angle X-ray scattering (SAXS, WAXS) and UV-Vis spectroscopy using a stopped-flow microfluidic device was systematic studied.

This lab-based equipment allowed investigations of the influence of temperature and precursor concentration on the temporal evolution of the particle size as well as on the energetic and optical properties of these zinc oxide nanoparticles. For the really early stages synchrotron SAXS experiments at the DESY Petra III P03-beamline were necessary.

The second part of this thesis deals with the growth kinetics of palladium nanoparticles. Palladium belongs to the group of platinum metals and is known as an expensive noble metal.^[25] Despite the high material costs, palladium nanoparticles are extensively studied, as they have many applications in catalysis and in the automotive industry in exhaust-gas catalytic converters and fuel cells.^[25-28]

In the course of this work the high temperature palladium nanoparticle synthesis by Mazumder and Sun^[27] should also be performed microfluidically and simultaneously analyzed and characterized by X-ray scattering methods.

At this juncture there was the problem that the formation of gas bubbles destroyed the continuous flow or even for the stop-flow method, the continuous phase in the X-ray and thus disturbed this method of investigation. By reason of this, a 1 mm quartz capillary served as the reaction vessel, allowing to synthesize this palladium nanoparticles in a heatable capillary holder and perform in situ SAXS-experiments. These were carried out at the DESY Petra III P03-beamline.

The third part of this thesis deals with developing complex microfluidic biochips to investigate blood agglomeration and biosynthesis of platelets. During a cooperation with Dr. Markus Bender and his team, a working group of the Department of Experimental

Biomedicine at the University Hospital Würzburg, microfluidic chips were designed and fabricated for experiments in the field of biology and medicine.

Microfluidic chips have been designed and fabricated to model stenosis, for example in order to study thrombus formation and stability in vitro under dynamic conditions. Ruth Kranz (Experimental Biomedicine at the University Hospital Würzburg) will also be writing a part of her dissertation on this topic, but she is mainly referring to the biological and medical analysis of the experiments and not to the technical part of this cooperation I was focusing on.

Microfluidic bioreactors have been designed and fabricated to study proplatelets, long cytoplasmic extensions with the appearance of beads linked by cytoplasmic bridges, from which platelets pinch off. Microfluidics offers the possibility to carry out the experiments under dynamic conditions, which has a positive effect for example on the number of platelets forming in comparison to the static conditions in culture^[17,18] and is a possible step in the direction of platelet supply independent from human donors.

1.2 Organization of this thesis

The thesis is divided in two significant parts. The first part gives the reader an understanding to the theoretical background and experimental methods which are important to this work. In the course of this, the second chapter gives an overview about the used X-ray scattering methods, informs about the nanoparticles which were synthesized during this work, the synthesis methods and nucleation and particle growth and explains the principles of microfluidics, microfluidic devices and microfluidic nanoparticle synthesis.

In the second part, chapter 3 discusses the results of the particular projects of this work in detail. This chapter includes the investigation of nucleation and growth kinetics of ZnO nanoparticles by in situ SAXS/WAXS/UV-Vis-experiments (chapter 3.1), the investigation of the growth kinetics of Pd nanoparticles by in situ SAXS-experiments (chapter 3.2) and the development of microfluidic chips for studying biological and medical processes (chapter 3.3). Finally, chapter 4 summarizes the significant results of this thesis and also provides ideas for future works and chapter 5 describes the used materials and methods.

2 Theoretical Fundamentals

The following pages give an overview of the theoretical fundamentals of nanoparticles, microfluidics and the during the work used analytics and characterization methods. The chapter "Nanoparticles" deals with semiconductor and metall nanoparticles as well as synthesis methods and explains the theory about nucleation and particle growth. The physical basics of Microfluidics as well as some information about microfluidic devices and microfluidic nanoparticle synthesis are embraced in chapter "Microfluidics". In the chapter "Investigation methods of nano- and microstructures" X-ray scattering methods are addressed in more detail concerning their experimental setup and physical fundamentals as well as the transmission electron microscopy and UV-Vis spectroscopy.

2.1 Nanoparticles

Nanoparticles are smallest particles whose characteristic size ranges from 100 nm to 1 nm. Because of this, their physical and chemical properties also differ significantly from those of larger particles.^[29] The reduction of the particle diameter into the nanometer range leads to an increase in the surface-volume ratio. This is the reason why the surface properties dominate with nanoparticles - unlike in the macroscopic system, in which the bulk properties predominate.^[1]

For example, nanoparticles have a lower melting point, absorb light at low wavelengths, and have different mechanical, electronic, and magnetic properties than macroscopic particles of the same material.^[29] Therefore, there is a great deal of interest in the research and application of nanoparticles: catalysis^[30], data storage^[31], solar industry^[32] and medicine^[31,32] to refer just a few examples.

This chapter is intended to provide an overview of the general production of nanoparticles, as well as inform on nucleation and particle growth and the nanoparticle classes, semiconductor and metal nanoparticles, which where investigated during this work in form of ZnO an Pd nanoparticles.

2.1.1 Production of Nanoparticles

Basically, there are two different ways of producing nanoparticles. A distinction is made between the *top-down* method and the *bottom-up* method, as shown in figure 2.1. *Top-down* is the mechanical-physical reduction of the original material.

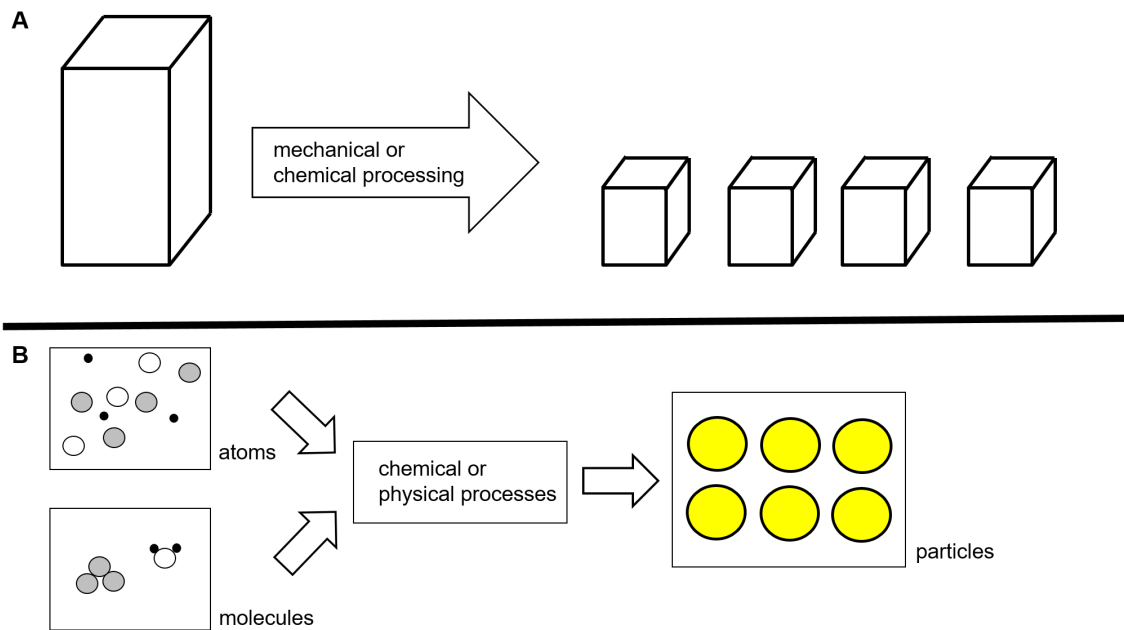


Figure 2.1: Schematic illustrations of the top-down (A) and bottom-up (B) method to produce nanoparticles

This method starts from large pieces of material to produce the intended structure, like it is shown in figure 2.1 A. This includes, for example, milling processes for metallic and ceramic nanomaterials. Compared with the *bottom-up* approach, this production variant of the nanoparticles has a broad particle size distribution. However, the advantage of this method is that it can be done on a large scale.

The *bottom-up* method is based on physico-chemical principles of molecular and atomic self-assembly, allowing control over particle size and shape, and size distribution. Examples of such synthetic approaches are sol-gel methods, aerosol methods and precipitation reactions. Difficulties in the bottom-up approach, however, are in the control and control of the synthesis and drying steps, as well as the implementation on a larger scale.^[1,33,34]

2.1.2 Nucleation and Particle growth

2.1.2.1 LAMER Model

Colloid chemical systems have been developed for the synthesis of monodisperse nanoparticles. Classically, the formation of nanoparticles is explained using the *LAMER model*. For the preparation of monodisperse sulfur hydrosols, Viktor LaMer described a theory for the nucleation and growth mechanism in 1950.^[35]

Figure 2.2 shows a graph by which LaMer explained these mechanisms. The *LAMER*

model is in three stages divided.^[35,36]

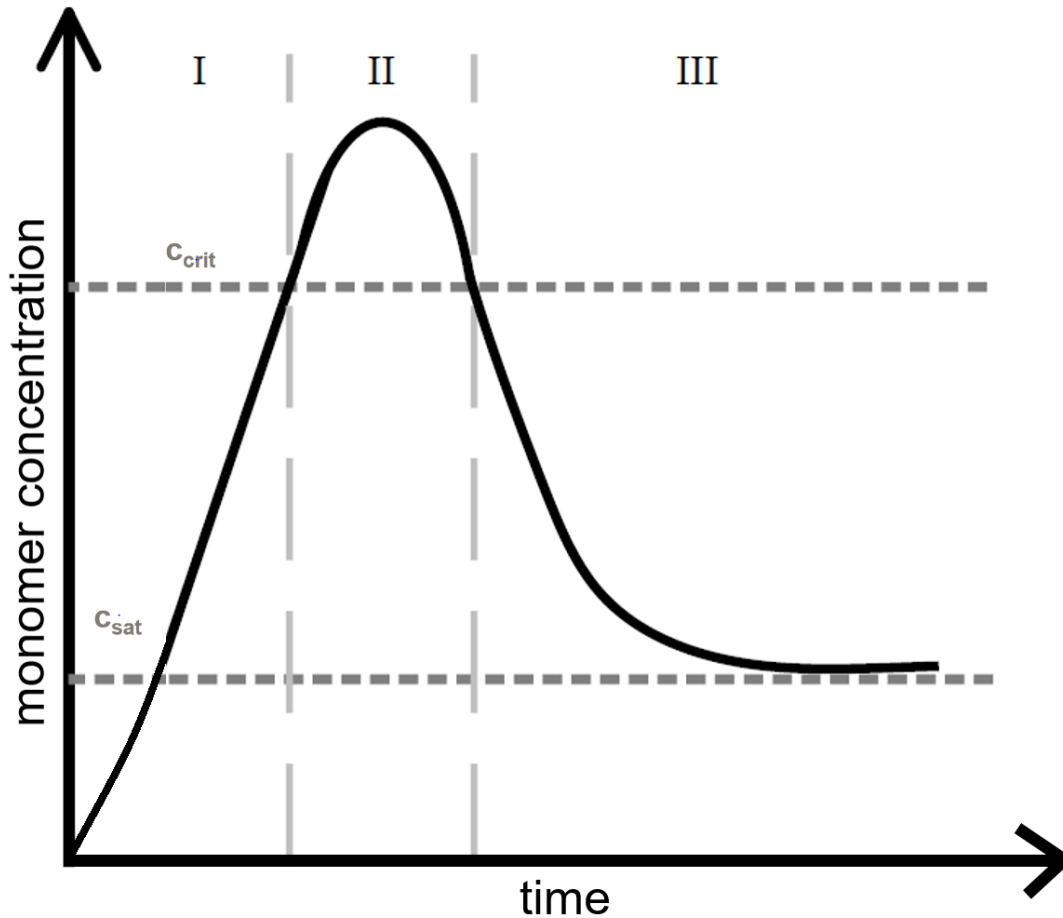


Figure 2.2: LAMER model for the synthesis of monodisperse nanoparticles with primary stage (I), nucleation (II) and growth (III)

In a primary stage (I), the monomer concentration increases until it reaches a critical value (c_{crit}). For example, if the monomers are metal ions, they will be reduced. As the reaction progresses, the concentration of metal atoms increases and a saturation concentration (c_{sat}) is reached.

At the point of critical concentration of the monomers, supersaturation of the solution has been achieved, thereby exceeding an energy barrier and initiating spontaneous nucleation (II). Thermodynamically, this energy barrier is interpreted by the free GIBBS energy^[36]:

$$\Delta G = 4 \cdot \pi \cdot r^2 \cdot \gamma + \frac{4}{3} \cdot \pi \cdot r^3 \cdot \Delta G_v \quad (2.1)$$

with r as the particle radius, γ as the surface tension, and ΔG_v as the change in the free energy between the monomers in solution and the volume unit in the bulk crystal. Within a very short time a large number of nuclei are formed at stage II.

Due to the nucleation process, the monomer concentration falls below the critical value, which is why the nucleation rate falls to zero and there is a break in the formation of new nuclei.^[35]

During the third stage (III) the growth process takes place.^[36] As a result of the consumption of the monomers, as shown by the further fall in their concentration in figure 2.2, the nucleation nuclei grow as long as there is supersaturation in the solution. According to LaMer, monodisperse nanoparticles can be synthesized when nucleation and growth take place separately, with a high rate of nucleation and a slow growth process being beneficial.^[35]

2.1.2.2 Thermodynamics of nucleation

The nucleation is initiated by a phase transition, which changes the free enthalpy G of the system. This can be described by means of the following equation 2.2:

$$dG = -SdT + Vdp + \gamma dA + i\mu_i dn_i \quad (2.2)$$

with S as the entropy, T as the temperature, V as the volume, p as the pressure, γ as the surface tension, A as the surface, μ as the chemical potential and n as the amount of substance. Under isothermal ($dT = 0$) and isobaric ($dp = 0$) conditions, as well as considering only one component, equation 2.2 simplifies to equation 2.3:

$$dG = \gamma dA + \mu dn \quad (2.3)$$

For small particles with a radius r the following conditions apply:

$$A = 4 \cdot \pi \cdot r^2 \rightarrow dA = 8\pi r dr \quad ,$$

$$V = \frac{4}{3}\pi r^3 \rightarrow dV = 4\pi r^2 dr \quad ,$$

$$dV = v_m dn$$

with v_m as the molar volume. By substituting these equations, the relationship described in equation 2.4 is obtained

$$dA = 8\pi r dr = \frac{8\pi r dV}{4\pi r^2} = \frac{2dV}{r} = \frac{2v_m dn}{r} \quad (2.4)$$

By substituting equation 2.4 into equation 2.3, the following relationship is established:

$$dG = \left(\frac{2\gamma v_m}{r} + \mu \right) dn \quad (2.5)$$

In equilibrium it is essential that $dG = 0$ and therefore also

$$\frac{dG}{dn} = \frac{2\gamma v_m}{r} + \mu = 0 \rightarrow \mu = -\frac{2\gamma v_m}{r} \quad . \quad (2.6)$$

Since the chemical potential μ corresponds to the supersaturation, the following relationship can be formulated:

$$\mu = \mu_{\text{bulk}} - \mu_{\text{sol}} = \Delta G_{\text{sup}} \quad (2.7)$$

where μ_{bulk} describes the chemical potential in the bulk, μ_{sol} the chemical potential in the solution and ΔG_{sup} the change in the free energy in the supersaturation.

From the equation $\Delta G_{\text{sup}} = R \cdot T \cdot \ln S$ the value for the critical nucleation radius R_{crit} is given by inserting into equation 2.3:

$$RT \ln S = -\frac{2\gamma v_m}{r} \rightarrow R_{\text{crit}} = \frac{2\gamma v_m}{RT \ln S} \quad . \quad (2.8)$$

In addition to the critical nucleation radius, the critical enthalpy of formation G_{crit} is crucial for the formation of nanoparticle nuclei.

This results from equation 2.3 as follows using equation 2.8:

$$\begin{aligned} G_{\text{crit}} &= \gamma 4\pi \left(\frac{\gamma 2v_m}{\mu} \right)^2 + \frac{\mu}{v_m} \frac{4\pi}{3} \left(\frac{\gamma 2v_m}{\mu} \right)^3 \\ G_{\text{crit}} &= \frac{\gamma^3 16\pi v_m^2}{\mu^2} - \frac{\gamma^3 32\pi v_m^2}{3\mu^2} \\ G_{\text{crit}} &= \frac{\gamma^3 16\pi v_m^2}{3\mu^2} \\ G_{\text{crit}} &= \frac{\gamma 4\pi}{3} (R_{\text{crit}})^2 \quad . \end{aligned}$$

Substituting equation 2.8 yields:

$$G_{\text{crit}} = \frac{\gamma^3 \cdot 16 \cdot \pi \cdot v_m^2}{3 \cdot (R \cdot T \cdot \ln S)^2} \quad . \quad (2.9)$$

By reaching a critical radius R_{crit} and a critical formation enthalpy G_{crit} , stable nuclei of nanoparticles can be formed. As it can be seen from the following equation, the change in the free enthalpy in nucleation is composed of a volume fraction G_V and an interfacial fraction G_G :

$$\Delta G = -\Delta G_V + G_G$$

$$\Delta G = -\frac{4}{3}\pi r^3 \cdot \Delta G_V + 4\pi r^2 \cdot \sigma \quad (2.10)$$

During a nucleation, a new interface is created, for its creation energy has to be applied, the so-called interfacial energy. Only when a nucleus has been formed, which radius is larger than the critical nucleation radius R_{crit} , its can grow and thereby minimize the free enthalpy. The released volume energy is proportional to the nucleus size. nuclei whose size is smaller than the critical nucleation radius R_{crit} lower the enthalpy of the system by dissolving again.^[36,37] It can also be seen from equation 2.8 that the critical nucleation radius is anti-proportional to the temperature.

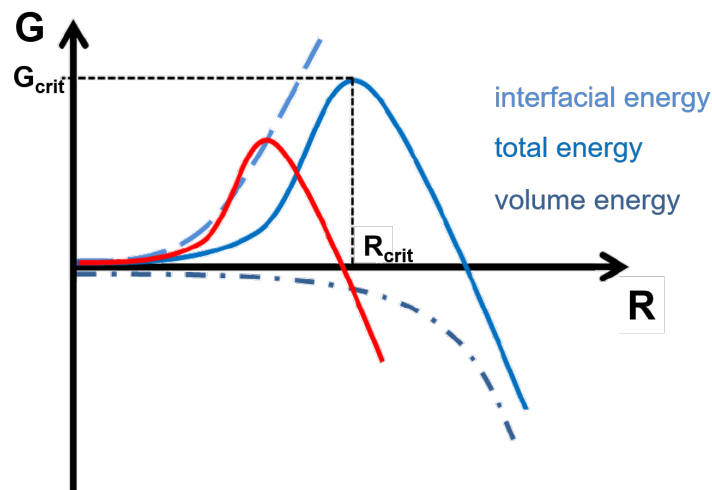


Figure 2.3: Schematic illustration of the nucleation-dependent formation enthalpy curve, whereby nucleation starts earlier at high temperatures (red curve) than at lower temperatures (blue curve)

As the temperature of the reaction system increases (red line in figure 2.3), the size that a seed must reach in order to grow is less than at low temperatures (blue curve in figure 2.3).

2.1.2.3 Kinetics of the nanoparticle formation reaction

Chemical kinetics deals as a topic of physical chemistry with the velocity of chemical reactions. It is examined how fast the starting materials are consumed and the products are formed. The following equation serves as an example of an formational reaction:



The reaction rate is defined as a change of the concentration of a species with time. The rate of formation is as follows:

$$j_{AB} = \frac{d[AB]}{dt} \quad (2.12)$$

where j_{AB} describes the rate of formation of the nanoparticles, $d[AB]$ the change in the concentration of these particles and dt the time change.

In addition, the formation reaction of these AB nanoparticles can be described as a second-order reaction since the following relationship applies:

$$j_{AB} = k_1 [A^{2+}] [B^{2-}] \quad (2.13)$$

where k_1 stands for the rate constant, $[A^{2+}]$ for the concentration of the cations and $[B^{2-}]$ for the concentration of the anions.

The rate of chemical reactions increases with increasing temperature, since the rate constant k depends on the temperature, which can be expressed by the Arrhenius equation:

$$k = A \cdot e^{-\frac{E_A}{R \cdot T}} \quad (2.14)$$

where A is a pre-exponential factor, E_A is the activation energy, R is the universal gas constant, and T is the temperature.^[37]

As described in the previous chapter, the formation of nanoparticles consists of several steps. First, nucleation occurs before these nuclei grow into nanoparticles. The nucleation rate j_{nuc} describes the nuclei formed per volume and time and is also described in the Arrhenius approach:

$$j_{nuc} = \beta \cdot [AB] \cdot \frac{V}{v_m} \cdot e^{\frac{\Delta G_c}{k \cdot T}} \quad (2.15)$$

In equation 2.15 β describes a prefactor, ΔG_c the change of the free enthalpy, V the volume of a new nucleus ($\frac{4\pi r^3}{3}$), v_m the molar volume and k the Boltzmann constant. The prefactor β and the change in the free enthalpy ΔG_c are described in more detail in equations 2.16 and 2.17:

$$\beta = \frac{4kT}{9\eta v_m} \quad (2.16)$$

$$\Delta G_c = \frac{16\pi\gamma^3 v_m^2}{3(kT)^2 (\ln S)^2} \quad (2.17)$$

with η as the viscosity, γ as the interfacial energy and S as the supersaturation $\left(\frac{[AB]}{[AB]_{sat}}\right)$. Once a stable nucleus has formed, its growth process begins.

The growth rate can be formulated as follows:

$$j_{growth} = 4 \cdot \pi \cdot R^2 \cdot k_{growth} \cdot \frac{[AB]}{v_m} \cdot \left(S - e^{[-\frac{R^*}{R}]}\right) \quad (2.18)$$

where R is the radius of a new nanoparticle nucleus ($\frac{R^*}{\ln S}$), k_{growth} the growth rate constant and R^* the capillary radius ($\frac{2\gamma v_m}{kT}$).

Once a steady-state equilibrium has been established, the formation and decomposition reactions are equally fast and are described in a simplified manner by the temporal change in the concentration of the nanoparticles. Thereby, the following equation can be obtained:^[36]

$$j_{AB}(t) + j_{nuc}(t) + j_{growth}(t) = \frac{d[AB]}{dt} \quad (2.19)$$

2.1.3 Semiconductor Nanoparticles

Semiconductor nanoparticles are nanoparticles composed of compound semiconductors. Many compositions are already known^[38-40], some examples are listed in table 2.1:

Table 2.1: Examples of semiconductor nanoparticles

Composition	Examples of semiconductor nanoparticles
II - VI	CdSe, CdS, ZnSe, ZnS, ZnO
III - V	InP, InAs, GaAs
IV - VI	PbS, PbSe,

Due to their size-dependent chemical and physical properties, the importance of semiconductor nanoparticles has increased in recent years.

Solar cells, optical-electronic components and laser printers are just a few of the numerous fields of application.^[13,41,42] The shape of the nanoparticles is classified by their dimension, for example, there are two-dimensional slices, one-dimensional rods and so-called zero-dimensional isotropic spheres and cubes. The zero-dimensional nanocrystals are also called *Quantum Dots*.^[38,42]

A special feature of *Quantum Dots* is that their emission wavelength can be changed by changing the size of the particles. The confinement effect is the principle for this.^[41] The energies of the electron and electron hole levels are sensitive to the scope of the confinement. A strong confinement regime occurs when the particle radius of the nanocrystals is much smaller than the Bohr radius of the electron, the Bohr radius of the electron hole and the exciton boring radius. In such a case, the electrons and their holes are severely limited by the boundaries of the nanoparticles.

The bandgap E_g of semiconductor nanoparticles increases as the particle size decreases. This effect is also called a quantum size effect. In addition, the phenomenon of the confinement effect leads to discrete energy levels. In comparison, in macroscopic semiconductors valence and conduction bands are present.^[32,42] This can be seen in figure 2.4.

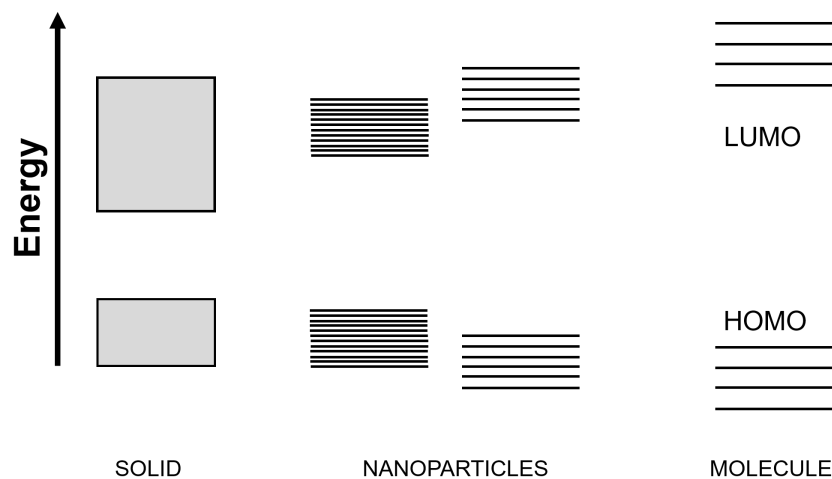


Figure 2.4: Schematic representation of the energy level diagrams for macroscopic semiconductors (solids), nanoparticles and molecules. It can be seen that nanoparticles have an increased bandgap and quantified energy states

The semiconductor nanoparticles studied during this thesis are zinc oxide (ZnO) nanoparticles. ZnO is a colorless semiconductor and an UV-absorber.^[43,44] Applications for this nanoparticles are in solar cells, photocatalysis, UV-blocker, gas-sensors and ointments.^[19,40,44]

They are also used as a cheap and safe method for fluorescent labels for anti fake labeling in the security safeguarding for merchandise and in nanopharmaceutical products for imaging. ZnO nanoparticles belong to the most studied metal oxide material.^[40]

Zinc oxide is one of the most important zinc compounds and contains zinc in the +2 oxidation state. It is an easily soluble compound that crystallizes in the wurtzite type (see figure 2.5).

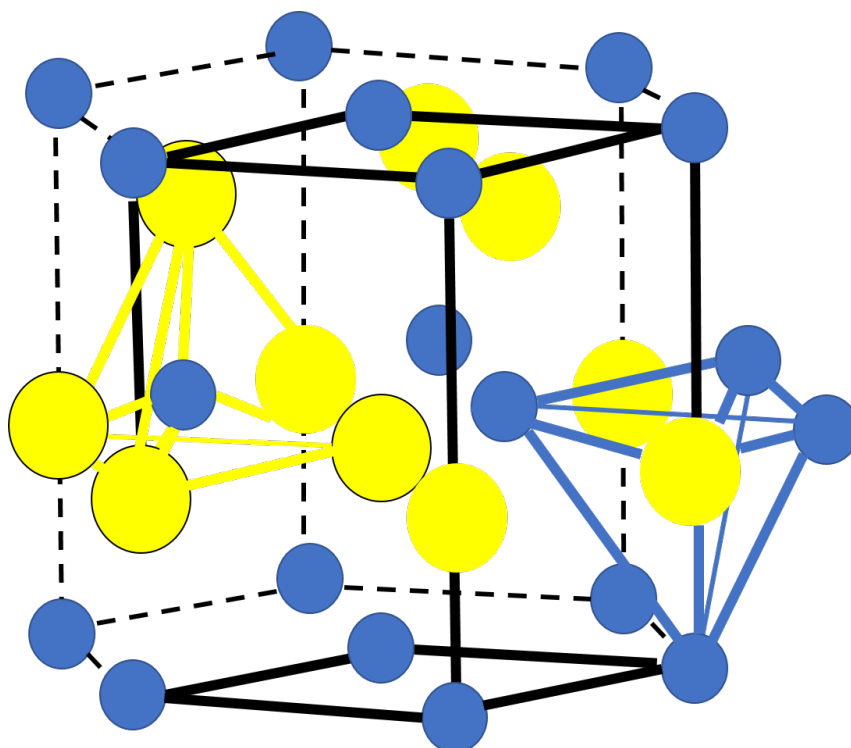


Figure 2.5: Schematic representation of the wurtzite crystal structure

2.1.4 Metal Nanoparticles

Metal nanoparticles are small compounds represent the transition from metal to solid.^[45] Compared to macroscopic metals, metallic nanoparticles have altered properties, which can be explained by their small size and high surface-to-volume ratio.

Metal nanoparticles are certain to the building blocks of the next generation of electronic, optoelectronic and chemical sensing devices.

They are interesting nanoscale systems, because of the ease with which they can be synthesized and modified chemically.^[46]

During this work, kinetic studies were performed on the synthesis of palladium nanoparticles. Palladium belongs to the light platinum metals and is thus an actually inert precious metal. Finely distributed it has the highest absorption capacity of all elements for hydrogen and thus has good catalytic properties.^[44] That is one reason why interest in the research of palladium nanoparticles has increased recently.

This can be justified because of the wide-ranging and numerous fields of application of these metal nanoparticles: They serve as an alternative to platinum, because it also catalyzes numerous chemical reactions^[27]. In addition, these nanoparticles are used in the automotive industry, for example in exhaust-gas catalytic converters and fuel cells.^[25-28]

2.2 Microfluidics

Microfluidics is a science that, as the name implies, deals with the behavior of small amounts of liquids or gases in channel systems with a dimension from 1 μm up to 1 mm.^[5,6,12] Microfluidics manipulates very small amounts (10^{-9} to 10^{-18} litres) of fluids in laboratories chip (lab-on-a-chip) and finds many applications in medicine, biology and chemistry.^[5,6,47] This chapter is divided in three parts and deals with the concepts and physics of microfluidics, microfluidic devices and some applications in the field of nanoparticle synthesis and biofluids.

2.2.1 Physicle basics

The macroscopic behavior of liquids is explained by means of hydrostatics and hydrodynamics. The microfluidic behavior often has low velocities and small amounts of fluid.^[6,47] At such low volumes, the behavior of liquids changes. By means of the REYNOLDS number (Re) the physical difference between the macro- and the microfluidics can be explained:

$$Re \equiv \frac{\text{inertial force } f_i}{\text{viscous force } f_v} = \frac{\rho \cdot v \cdot l}{\eta} \quad (2.20)$$

where ρ is the density of the fluid, v is the flow rate, l is the characteristic length in a fluidic system and η is the viscosity of the fluid.^[6,12,47]

In microfluidics, Re is typically less than 1, and $Re \approx 1000$ is set as the "critical limit" to macrofluidics. For large Reynolds numbers, the inertial forces dominate as we know them from everyday life. At low Re , however, the viscous forces dominate.^[6]

The dominance of the viscous forces has the consequence that well-known macrophenomena such as turbulence are eliminated at small Re . The liquid flows laminar (2.6 A). The flow lines (lines of equal velocity) no longer intersect each other like in

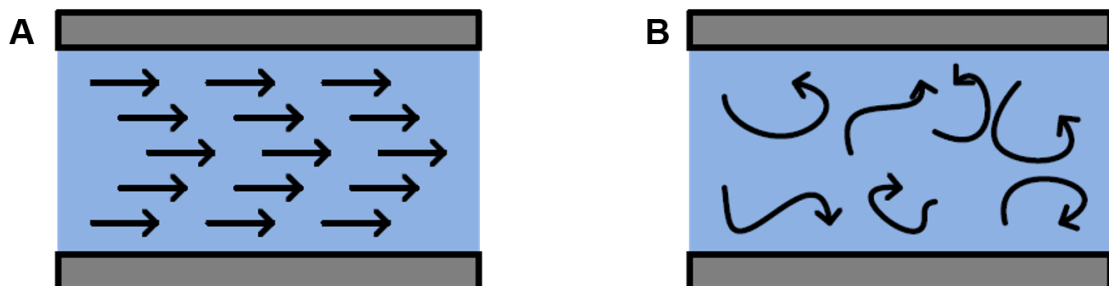


Figure 2.6: Schematic illustrations of the difference between laminar flow (A) and turbulence (B)

case of turbulence, as it is sketched in figure 2.6 B. Consequently, the various layers flow side by side (parallel to the channel wall) without turbulence and this allows only a diffusive mixing of different liquid components in microfluidic devices.^[6,47]

Perpendicular to the flow direction, the impulse, mass and heat transport are carried out by diffusion and heat conduction. Like it is shown in figure 2.6 A, there is a parabolic velocity profile in the laminar flow. Contrary to some assumptions that the flow velocity at the channel walls is zero, there is often some slip between liquid and channel material. This depends on the surface condition of the substrate and the rheological property of the liquid.^[48]

In addition, microfluidics is characterized by a large ratio between the contact surface between the liquid and the channel wall and characterized by the volume enclosed by the channel. Because of this, there are strong interactions between the channel wall and the liquid.^[6]

2.2.2 Microfluidic devices

Microfluidic reactors deal with the flow of smallest quantities of liquid in channels in the magnitude of μm -range. For the first time, such reactors were developed in the 1990s.^[5] In a relatively short time, there was a rapid development in design, the manufacturing process and the fields of application. The latter include pharmaceutical and biotechnology, as well as the chemical industry with applications such as in synthesis, diagnostics, crystallization and rapid chemical analyzes.^[7]

The fabrication of microfluidic chips can be divided into three steps:

1. Development of the desired design
2. Micro-structuring of wafers and polymer substrates into microchannels
3. Assembly of micro-components to the microfluidic device

The design of the channels in the microfluidic chip is functionally dependent. Channels for catalytic reactions have a different appearance than channels that are to be used for example as a micromixer or microsensor.^[7]

The focus of the design of the microfluidic channels is also on the number of in-flow channels. This influences the focusing of the solution in the microfluidic channel and thus can also change the location and time of the mixing of the substances.

Figure 2.7 shows schematic illustrations of exemplary channel designs for the various focusing options.

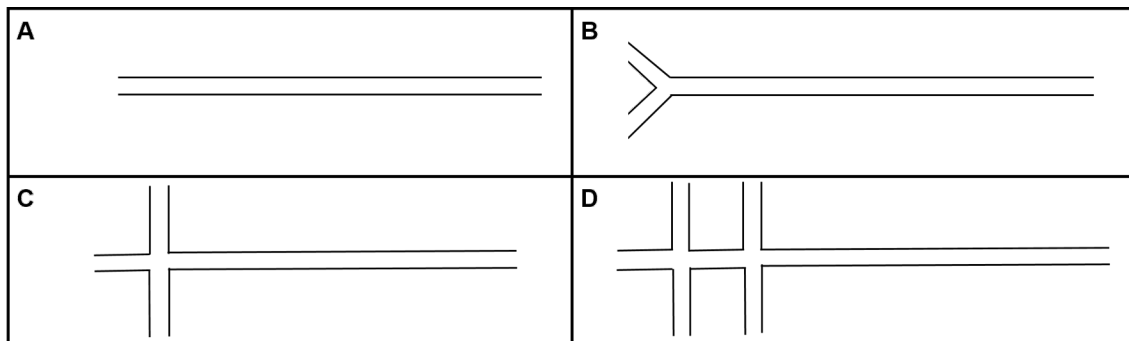


Figure 2.7: Schematic illustrations of different channel designs with main focus on the possibilities of focusing the solutions in the microfluidic chip

If only one main channel is used, like it is shown in figure 2.7 A, the solution is not focused in the microfluidic chip and there is no mixing in the microfluidic device possible. The substance fills the entire channel and thus is not only in the middle of the channel, but also on the channel walls.

The simplest channel design for mixing of two substances is the Y-shape design in figure 2.7 B. Here, the mixing process begins as soon as the substances meet.

Figure 2.7 C shows the use of two secondary channels. The solution in the main channel is simply focused through the solution, which passes through the secondary channels via the mixing cross to the solution in the main channel. In this design, the contact between the substance from the main channel is prevented with the channel wall.

A microfluidic channel design with double focusing is shown in figure 2.7 D. This can be achieved by using channel systems with a total of four sub-channels or two sub-channel systems. It should be noted that the use of multiple focusing also changes the design of two-dimensional to three-dimensional MF chips.

Since the mixing channels of the sub-channels are arranged from different levels around the main channel, the flow is better focused in the main channel. The goal of this channel design is that fewer particles can be deposited on the channel walls.

For the micro-structuring of wafers and polymer substrates into microchannels, the so-called rapid prototyping method^[49,50] is used. In this case a combination of pho-

tolithographic and soft lithographic production is usually used. The begin of the rapid prototyping method is designing the CAD model of a planed device structure. After this it is printed on a UV semi transparent mask usually and are used for the photolithographic process for the production of silicon masters. For very small structures, the desired design is transferred to a chrome mask. This is low reflective chrome oxide on soda lime glass or fused silica.

To manufacture a microfluidic device by rapid prototyping in PDMS, a master structure containing the positive relief of the desired microstructure is fabricated via photolithography using commercially available photoresists, such as SU-8^[51-54]. The device master is reusable and can be replicated over many cycles and thus allows rapid prototyping at low cost. A detailed description of the master preparation is written in chapter 5.3.1.

The assembly of micro-components to the microfluidic device is material dependent, which is why welding, gluing or even treating the material with UV light or plasma for the desired bond generation are just a few ways to unify the components. A large number of working groups produce microfluidic chips from polydimethylsiloxane (PDMS).^[49,55-57] As the rapid prototyping process continues, the microchannels in PDMS can be formed by replica molding.

Since the PDMS changes only minimally after curing (less than 1 %), the design features can be replicated down to the nanoscale. Thereafter, for a two-dimensional microfluidic chip the open PDMS replica is sealed with a glass slide that is covalently bonded to the PDMS surface in a condensation reaction between the silanol groups on the PDMS and the glass surface that have been previously generated in an air or oxygen plasma.^[58] A detailed description of this template production is written in chapter 5.3.2.

2.2.3 Microfluidic nanoparticle synthesis

The number of working groups that perform nanoparticle syntheses in microfluidic systems is increasing.^[7] For example, Cu-NP^[8], TiO₂-NP^[59], SiO₂-NP^[60], CdSe-NP^[61,62], CdS^[11] and Au-NP^[15,63] have already been synthesized. Most microfluidic nanoparticle syntheses known in the literature are droplet syntheses and/or room temperature syntheses.

A recent development in the field of microfluidic nanoparticle syntheses is the implementation of high temperature synthesis. Due to the high temperatures, the choice of materials for the microfluidic chips is a challenge, since a temperature and solvent

resistance is required. The mixing of the reaction educts of a microfluidic nanoparticle synthesis takes place in the microfluidic reactor. Significantly lower amounts of chemicals are required^[7] and it is possible to apply analysis and characterization methods already during the synthesis, which is not possible with classical flask synthesis.

2.2.3.1 Mixing in microfluidic channels

Since the liquid flow in microchannels is a diffusion-based laminar flow due to the low Reynolds number, liquids can also be mixed only by diffusion in such channels.^[6,64,65] Although in macroscopic systems diffusion mixing is slower than turbulence, this is not true for a blending in microfluidic systems. Because of the small size of the microfluidic channels, diffusion is not a slow process because the rule of thumb is "*100 times faster if the system is 10 times smaller*".^[64]

This is also evident in the equation 2.21 for the diffusion time

$$t_{\Delta x} = \frac{\Delta x^2}{2 \cdot D} \quad (2.21)$$

where $t_{\Delta x}$ is the diffusion time, D the diffusion coefficient and Δx the diffusion distance. Microfluidic mixing differs between active and passive mixing.

Active microfluidic mixers enhance the mixing performance by stirring or agitating the fluid flow using some form of external energy supply. For example these include ultrasonic, dielectrophoretic force actuation, electrokinetic time-pulsed actuation, pressure perturbation and thermal actuation.

In contrast, passive micromixers require no energy input other than the pressure head used to drive the fluid flows at a constant rate and contain no moving parts.^[65] The small channel sizes and the lack of turbulence in microfluidic systems has led to the development and publication of several passive mixer designs, often operating under pressure-driven flow.^[66]

Lamination, zigzag channels, intersecting channels, surface-chemistry technology and twisted channels are just a few examples of the major forms of passive microfluidic mixing.^[65]

In the synthesis of the ZnO nanoparticles of this work a passive microfluidic mixture was applied. For this a microfluidic design with intersecting channels (Y-shaped) was used.

2.2.3.2 Fick's laws of Diffusion

Diffusion is the movement of molecules or atoms from a region of higher concentration to a region of lower concentration as a natural physical process due to Brownian molecular motion. Over time, it leads to a complete mixing of two or more substances through the even distribution of the mobile particles, thus increasing the entropy of the system.^[37]

For diffusion currents the driving force is the local difference in the concentration c of the diffusing particles.^[67,68] This movement is measured by its diffusion flux J and describes the number of molecules N , which are passing through a unit area A per unit time t ^[37]

$$J = \frac{dN}{dt} \quad . \quad (2.22)$$

According to the *Fick's first law of diffusion*, the particle transport J is proportional to the concentration gradient dc/dx ^[37,67,68]

$$\frac{dN}{dt} = J = -D \cdot \frac{dc}{dx} \quad . \quad (2.23)$$

This equation states that diffusion is faster, the more the concentration changes with location. At a homogeneous concentration ($dc/dx = 0$), no diffusion takes place.

The proportionality constant in equation 2.23 is the diffusion coefficient D , which can also be described with the *Stokes-Einstein equation* for a spherical particle with a radius R as follows:

$$D = \frac{k_B \cdot T}{6 \cdot \pi \cdot \eta \cdot R} \quad (2.24)$$

where k_B is the Boltzmann constant, T the temperature and η the viscosity of the solvent.

The rate of diffusion is obtained via the Einstein-Smoluchowski equation and the mean displacement square $\langle x^2 \rangle$:

$$\langle x^2 \rangle = 2 \cdot D \cdot t \quad . \quad (2.25)$$

The diffusion rate of one particle over the distance Δx can thus be calculated according to:

$$\frac{\Delta x}{t_{\Delta x}} = \frac{2 \cdot D}{\Delta x} \quad . \quad (2.26)$$

Via the diffusion coefficient D , the diffusion rate depends on the temperature T and the viscosity η of the solvent.

By changing this equation 2.26, equation 2.21 is obtained and the diffusion time $t_{\Delta x}$ of a particle over the diffusion distance Δx can be considered.

The diffusion equation, which is also called *Fick's second law of diffusion*, establishes a relationship between the rate of concentration change at a given point and the spatial variation in concentration at that point and follows directly from *Fick's first law of diffusion*^[37]

$$\frac{\delta c}{\delta t} = D \cdot \frac{\delta^2 c}{\delta x^2} \quad . \quad (2.27)$$

The diffusion equation 2.27 is a differential equation of the second order with respect to the location and first order with respect to time. To solve this equation, it must therefore be specified two boundary conditions for the spatial variable and an initial condition for the time^[37]:

1. At $t = 0$, all N_0 particles are within an area A in the yz -plane (at $x = 0$).
2. The concentration must be finite everywhere.
3. The entire amount of substance is always $n_0 = \frac{N_0}{N_A}$.

From conditions 2 and 3, it follows that the flow at the boundaries of the system must be zero. This gives the following equation

$$c(x, t) = \frac{n_0}{A \cdot (\pi \cdot D \cdot t)^{0.5}} \cdot e^{-x^2/4Dt} \quad . \quad (2.28)$$

2.2.4 Bio fluid mechanics

Bio fluid mechanics is a branch of bionics, which deals with methods and phenomena of locomotion of living things in the air and in the water. But also pulsating currents are treated in cycles, which also includes the bloodstream.^[69] This is driven by the heart, the central pump of this circulation system. Peripheral blood vessels - arteries, veins and capillaries - are also components of this system.^[70]

A very interesting part of the bloodstream is the arterial circulation, which is characterized by pulsating inlet flows, secondary flows in the vein curvatures and branches as well as the quasi-stationary flow in the arterioles and capillaries with the gas and metabolic exchange.^[69] The Reynolds numbers of blood flow in the arteries is in the range from 100 to several thousand.^[70-72]

The flow pulse of the heart causes a periodic laminar flow in the smaller arteries and a transitional flow in the larger arteries. The transition to turbulent arterial flow is initiated by temporary inflection point profiles. These occur in the transient return flow in the vicinity of the blood vessel wall during the relaxation phase of the heart. The time of a cardiac cycle, however, is not sufficient to establish a developed turbulent flow. The smaller the branching of the arteries, the lower is the influence of the pulsating flow of the heart.^[69]

Due to deposits on the blood vessel walls an arteriosclerosis occurs, thus increases flow separation at the branching of the arteries and a turbulent flow with increased flow losses will set in the pronounced inflection point profiles. Arteriosclerosis of the artery walls occurs in the areas of the arterial branches, where temporarily decreasing wall elasticity due to flow separation results in decreasing elasticity. The deposition process begins with the deposition of fat cells into the intima layer of the arterial wall, which eventually forms plaques of excess cells, lipids and calcium. These can break up and form thrombi. If it comes to a closure of the artery, it is called a stenosis.^[69]

Observing and investigating the formation of a stenosis and the formation of thrombi is an interesting and important field of research, since there are many people suffering from arterial diseases. In order to a better understanding and managing these diseases, microfluidic channels give the opportunity to do experiments under conditions, which are similar to the biological system. On the one hand they consist of a flexible and nevertheless stable material, on the other hand they offer the possibility of carrying out the experiments under dynamic conditions.

2.3 Investigation methods of nano- and microstructures

In order to be able to investigate structures in the nanometer and micrometer range, methods are needed that provide information on the properties - such as the size, shape, crystallinity and color - of the materials to be investigated. The characterization methods used during this work are described in this chapter.

2.3.1 X-ray Scattering

X-ray scattering is a method for analyzing and characterizing particles, for example in terms of their size and the associated size distribution, their shape and their crystalline structure. X-rays are electromagnetic waves in the wavelength range of 10^{-4} to 5 nm.^[4,73] In the present work, two forms of X-ray scattering were used: *small-angle X-ray scattering* (SAXS) and *wide-angle X-ray scattering* (WAXS).

The small-angle X-ray scattering uses monochromatic X-rays for the investigation of matter while confining itself to small scattering angles ($\theta_{\max} \approx 4^\circ$). The distances source-sample and sample-detector are both very large. Typical sizes of examined objects are in the range between 1 nm and 500 nm.^[73]

Using wide-angle X-ray scattering even smaller structures are investigated, such as crystal lattices at the atomic level. The scattered X-rays are interpreted at wider angles. The obtained WAXS pattern enables the analysis of structures below nanometer size ($d < 1$ nm) such as atoms and interatomic distances which scatter towards wider angles.^[74]

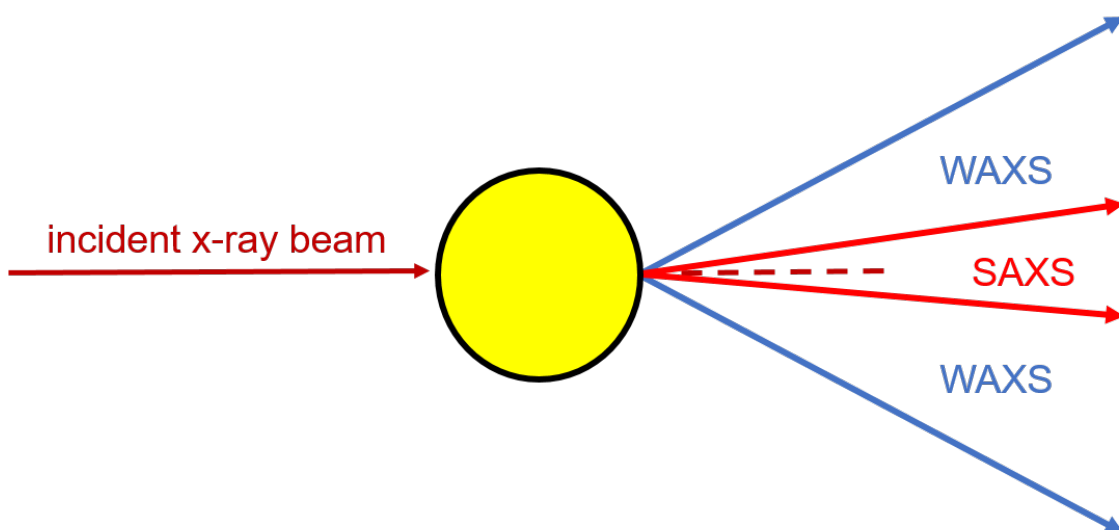


Figure 2.8: Schematic illustrations of the difference between SAXS and WAXS

The distance between sample and detector is smaller than in case of SAXS measurements. This chapter deals with the physical basics of X-ray scattering and information on form factor and structure factor.

2.3.1.1 Physical Basics of X-ray Scattering

In an X-ray scattering process, there is an interaction between the incident X-ray beam and the electron shell of the atoms. Emitted coherent, secondary waves cause interference. By means of constructive and destructive interference of the diffracted radiation, characteristic diffraction patterns are obtained with a regular arrangement of scattering centers.^[75] In the case of constructive interference, the BRAGG-equation applies:

$$n \cdot \lambda = 2 \vec{r} \cdot \sin\theta \quad (2.29)$$

with n as a natural number for the diffraction order, λ for the wavelength, \vec{r} for the interplanar spacing and θ for the diffraction angle.

By means of figure 2.9, the scattering geometry is first defined to explain the theory of X-ray scattering. At two scattering centers with the distance r_{12} , a primary x-ray beam is incident with the wave vector \vec{k}_0 .

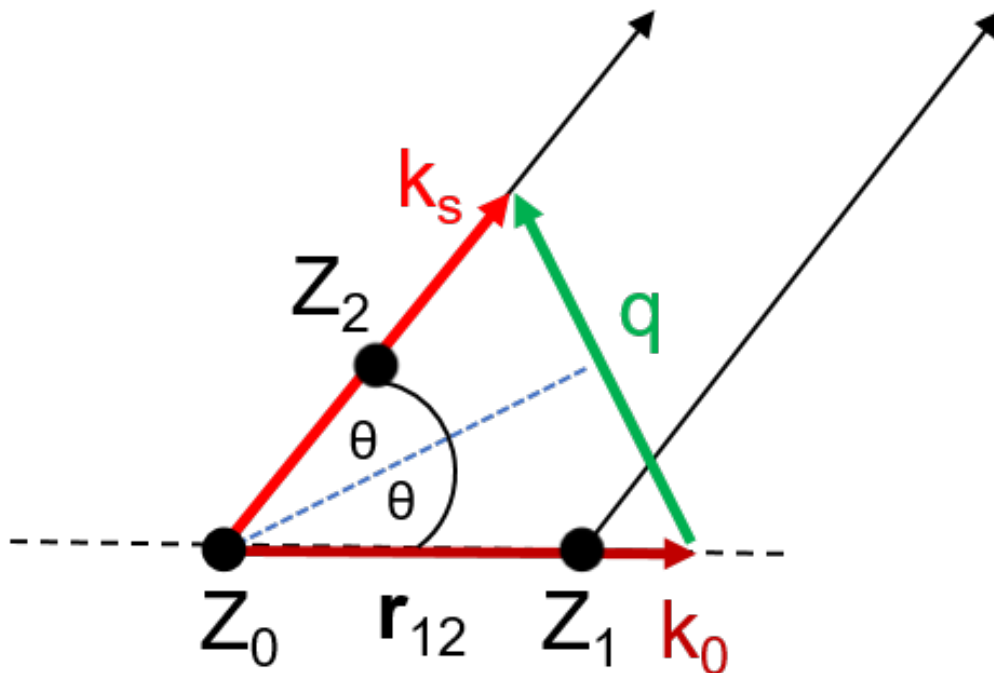


Figure 2.9: Schematic illustration of the scattering geometry

This is followed by an interference of the two waves scattered at the centers by the angle θ with the path difference Φ . This path difference Φ is determined by the difference of the distances $Z_0Z_1 - Z_0Z_2$ and therefore equation 2.30 follows^[73,76]

$$\Delta\Phi = \frac{2\pi}{\lambda} \cdot \left(\vec{r}_{12} \cdot \vec{k}_0 - \vec{r}_{12} \cdot \vec{k}_s \right) = \vec{r}_{12} \cdot \vec{q} \cdot \sin\theta \quad (2.30)$$

with \vec{r}_{12} for the radius vector between the two considered scattering centers, λ for the wavelength, \vec{k}_0 for the wave vector of the primary beam, \vec{k}_s for the wave vector of the scattered beam and θ for the diffraction angle.

The direction of the scattering experiment is indicated by the scattering vector \vec{q} , which is the difference of the wave vectors of the scattered beam \vec{k}_s and the incident X-ray beam \vec{k}_0 . For the absolute value of the scattering vector \vec{q} equation 2.31 follows:

$$\begin{aligned} \vec{q} &= \vec{k}_s - \vec{k}_0 \\ |\vec{q}| &= \frac{4 \cdot \pi}{\lambda} \cdot \sin\theta \quad . \end{aligned} \quad (2.31)$$

Due to the large number of electrons of the scattering objects, the scattering object is described by its electron density distribution. Each volume element provides a scattering amplitude proportional to the scattering amplitude A_e of a scattering center. The proportionality factor is the number of electrons in the considered volume element, also called electron density $\rho(\vec{r})$.^[73]

In order to obtain the scattering amplitude $A(\vec{q})$, the individual amplitudes of all scattering waves, described by the term $e^{-i\vec{q}\vec{r}}$, have to be summed up in phase.^[75]

All this results in the scattering amplitude $A(\vec{q})$:

$$A(\vec{q}) = A_e \cdot \int_V \rho(\vec{r}) e^{(-i\vec{r}\cdot\vec{q})} d\vec{r} \quad . \quad (2.32)$$

The scattering amplitude corresponds to the Fourier transform of the electron density distribution in the spatial domain.^[73] The real space is described by the location vector \vec{r} and the reciprocal space by the scattering vector \vec{q} .^[75]

The scattering intensity results from the formation of the square of the absolute value of the scattering amplitude

$$I(\vec{q}) = A(\vec{q}) \cdot A^*(\vec{q}) = I_e \cdot \iint_{VV'} \rho(\vec{r}) \rho(\vec{r}') e^{-i\vec{q} \cdot (\vec{r} - \vec{r}')} d\vec{r} d\vec{r}' \quad . \quad (2.33)$$

In contrast to the scattering amplitude, the scattering intensity is a measurable quantity. To calculate the quantitative scattering intensity, the intensity I_e of the secondary wave of the electron is needed.

From the Maxwell equations the classical formula of Thomson for unpolarized radiation for the scattering intensity of a free electron is obtained:^[73]

$$I_e(\Theta) = I_0 \cdot \frac{r_e^2}{d^2} \cdot \left(\frac{1 + \cos^2(2\theta)}{2} \right) \quad (2.34)$$

with I_0 for the primary beam intensity in consideration of the absorption, d for the sample-detector distance and r_e for the classical electron radius.

The scattering intensities in the X-ray scattering are normally normalized to the scattering intensity I_e .

Thus, the ratio of the scattering intensity of the entire sample to the scattering intensity I of a free electron is given under the same conditions and the same solid angle.^[73] This representation is called "electron units" [e.u.] and has two advantages:

1. It is an absolute size.
2. It reproduces the theory without the constant factor I_e .

2.3.1.2 Scattering Intensity of Isotropic Systems

Molecules in solutions are not fixed in a fixed orientation. They perform translative and rotational movements. Translational movements result in a constant phase factor for all scattering centers and do not change the scattering intensity. Rotational movements cause the particles to assume all possible orientations with equal probability. Moreover, if there is no remote ordering, such systems are called isotropic.^[73]

The scattering intensity as a function of the scattering vector can be simplified for unoriented systems with the following equation:^[75]

$$I(q) = 4 \cdot q \int_{r=0}^{\infty} p(\vec{r}) \cdot \frac{\sin(q \cdot r)}{q \cdot r} dr \quad (2.35)$$

This is done by summing up all intensities across all spatial arrangements. Where $p(r)$ represents the pair distribution function:

$$p(\vec{r}) = \gamma(\vec{r}) \cdot r^2 \quad (2.36)$$

For isotropic 2-phase systems (phase 1 \equiv particle; phase 2 \equiv solvent), the scattering intensity is given as follows:

$$I(\vec{q}) = (b_1 - b_2)^2 \cdot \rho_N \cdot P(\vec{q}) \cdot S(\vec{q}) \quad (2.37)$$

with b for the corresponding scatter length and $\rho_N = \frac{N}{V}$ for the number density, $P(\vec{q})$ for the form factor and $S(\vec{q})$ for the structure factor.

The form factor, as the name implies, indicates the shape of the particles and the structure factor indicates the spatial distribution.^[75]

2.3.1.3 Form Factor

The shape and size of particles can be described by the form factor. In this case, the particle form factor $P(\vec{q})$ of a sphere with the radius R applies

$$P(R, q) = A(R, q) \quad . \quad (2.38)$$

The equation for the scattering amplitude $A(\vec{q})$ of a homogeneous sphere can be set up the easiest, since in this case all orientations in space are equivalent and only dependent on the radius R :

$$A(R, q) = 3 \cdot \left[\frac{\sin(qR) - qr \cdot \cos(qR)}{(qR)^3} \right] \quad . \quad (2.39)$$

While calculating the form factor, it has to be noted that, in general, there is a size distribution of the particles. Therefore, the mean of the distribution $\langle \rangle$ is used, usually by means of the SCHULZ-ZIMM distribution.^[75]

For the function $f(R, q)$ the following equation applies:

$$\langle f(q, R) \rangle_R = \int_0^\infty f(q, R) R^m \cdot h(R) dR \quad (2.40)$$

with

$$h(R) = \frac{(z+1)^{z+m+1} \cdot R^z}{\bar{R}^{(z+m+l)} \cdot \Gamma(z+m+l)} \cdot e^{-\frac{(z+1) \cdot R}{\bar{R}}} \quad .$$

\bar{R} is the mean of the radius and for the weighting factor of the radius $m = 6$. The standard deviation is $\sigma_R = (z+1)^{-0.5}$ and there is a normalization of the distribution $\int_0^\infty h(R) dR = 1$.^[75]

2.3.1.4 Fractal Structures

During the last decades, it has widely been recognized that many structures common in experiments possess a rather special kind of geometry complexity.^[2] Benoit Mandelbrot was the first one who introduced fractal systems.^[2,77] He formulated the name fractal for complex shapes to express that they can be characterized by a non-integer (fractal) dimensionality.^[2]

This concept of fractals has been used in many systems like gels and aggregates. It summarizes and averages over very complex structural details. The fractal systems are described by two properties:^[77]

1. **Self-similarity:** The structure of the object is independent of the characteristic length scale of observation.
2. **Fractal dimension D :** It is defined as the exponent of the linear dimension R in the relation $M(R) \sim \left(\frac{R}{r_0}\right)^D$ and characterized mass fractals. Here is M the mass and r_0 the gauge of measurement.^[77]

Aggregation of similar particles represents an important class of growth phenomena producing complicated geometrical objects. Aggregation can take place particle by particle or the aggregates themselves are mobile and joined together to form larger clusters during their motion.^[2]

When the range of physical interest falls below 1000 Å, scattering techniques are the most appropriate way to study fractal structures and determine their fractal dimension D .^[77] During this work, small angle X-ray scattering has been used.

The form factor for the fractal structure is^[77]:

$$I(q) = (1 + a \cdot f(q)) \cdot P(q) \quad (2.41)$$

with a as a constant, $f(q)$ as the form factor of a fractal aggregate and $P(q)$ as the spherical form factor.

For the form factor of a fractal aggregate $f(q)$, the following relationship applies:

$$f(q) = \sin \left(\frac{(D-1) \cdot \arctan(X)}{(X \cdot (D-1) \cdot C^2)} \right) \quad (2.42)$$

with

$$X = q \cdot \frac{R_g}{C1},$$

$$\sqrt{D \cdot (D + 1)},$$

$$C2 = (1 + X^2)^{\frac{D-1}{2}}$$

where D is the fractal dimension, R_g is the radius of gyration of the aggregate and q is the scattering vector.

2.3.2 Transmission Electron Microscopy

Transmission electron microscopy (TEM) is one of the basic types of electron microscopes. It is an optical analysis method to image the surface of a sample by electrons instead of light. Compared to light microscopy, an electron microscope achieves a higher resolution at the same magnification. That is the reason why TEM can resolve smaller structures. Another advantage is the wider and higher magnification range.^[78,79]

2.3.2.1 Physical Basics of the TEM

The resolution limit of a microscope d_{\min} is determined by the wavelength λ of the radiation used. The smallest separable distance between two self-luminous object points d_{\min} is explained by Helmholtz about the relationship

$$d_{\min} = 0.6 \cdot \frac{\lambda}{n \cdot \sin(\alpha)} \quad (2.43)$$

with $\sin(\alpha)$ as a numerical aperture.^[80,81]

For a light microscope $d_{\min} = 200$ nm applies to visible light. In the case of a transmission electron microscope, an electron beam is used instead of a light beam. Due to the smaller wavelength of the electrons, a resolution of less than 0.2 nm is obtained according to equation 2.43.^[82]

TEM is an electron microscopic method to generate a transmitted light-electron image with a magnification of 100 to 500,000 times and a resolving power of 0.2 nm to 0.5 nm.^[83]

By the use of electron microscopes, it is possible to image samples up to a size in the atomic range with a very high resolution.^[84]

2.3.2.2 Construction of the TEM

The generation of the electron beam is as follows:

Electrons are emitted into an electron gun chamber by thermionic emission from a hairpin-shaped cathode, which is usually made of tungsten. A Wehnelt cylinder bundles and accelerates the electrons in the direction of the sample. Reactive gases may interact with the heated electron emitter.

Thereby the tungsten filament would burn out and that is the reason why vacuum is applied in the TEM. The control and focusing of the electron beam is made by using inhomogeneous magnetic fields, which are named lenses in analogy to light microscopes, like it is schematically shown in figure 2.10.

Then the beam is compacted in a condenser lens and projected onto the sample.^[78,79]

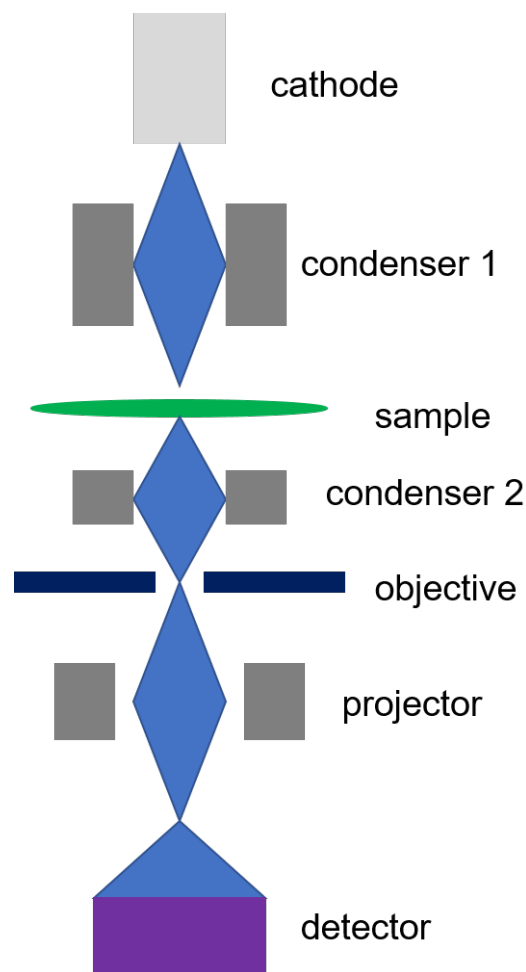


Figure 2.10: Schematic sketch of the construction of a transmission electron microscope

Subsequently, the electron beam impinges on the sample and three different interactions are possible:

1. Some of the electrons pass through the sample unhindered.
2. The electrons are deflected by positively charged atomic nuclei, resulting in a low energy loss. This is called elastic scattering.
3. The electrons of the beam impinge on the electrons in the atomic shell. These are characterized by their energy loss and a slight deviation from its orbit. This interaction is called inelastic scattering.^[75,78,79]

With the help of a transmission electron microscope very thin samples are always examined. There is hardly any absorption, but much more inelastic and elastic scattering.

The objective aperture of the objective lens (see figure 2.10) is adjusted that most of the non-scattered and the most of the inelastic scattered electrons pass through this. In this way an increase in contrast is achieved. The magnification of the image corresponds to the product of all magnifying lenses. The image is projected, for example, on a fluorescent screen.^[78,79]

2.3.3 UV-Vis spectroscopy

UV-Vis spectroscopy is an absorbance spectroscopic method that uses electromagnetic waves of ultraviolet (100 - 400 nm) and visible (400 - 760 nm) light for excitation of the molecules.^[85] The molecules are irradiated with photons whereby valence electrons are excited and raised onto a higher energy level (see figure 2.11).

The necessary energy of a photon to excite a valence electrons from a highest occupied molecular orbital (HOMO) to the lowest unoccupied molecular orbital (LUMO) in the investigated molecules is given by

$$\Delta E = h \cdot \nu = \frac{h \cdot c}{\lambda} \quad (2.44)$$

with ΔE as the energy difference between HOMO and LUMO, h as the Planck constant, c as the speed of light, ν as the frequency and λ as the wavelength of the electromagnetic wave.^[85]

In this spectroscopy atoms produce clearly defined line spectrum, because only individual transitions take place. These can be assigned to each of a defined wavelength. For molecules in liquid state occur broad absorbance bands, because many rotational

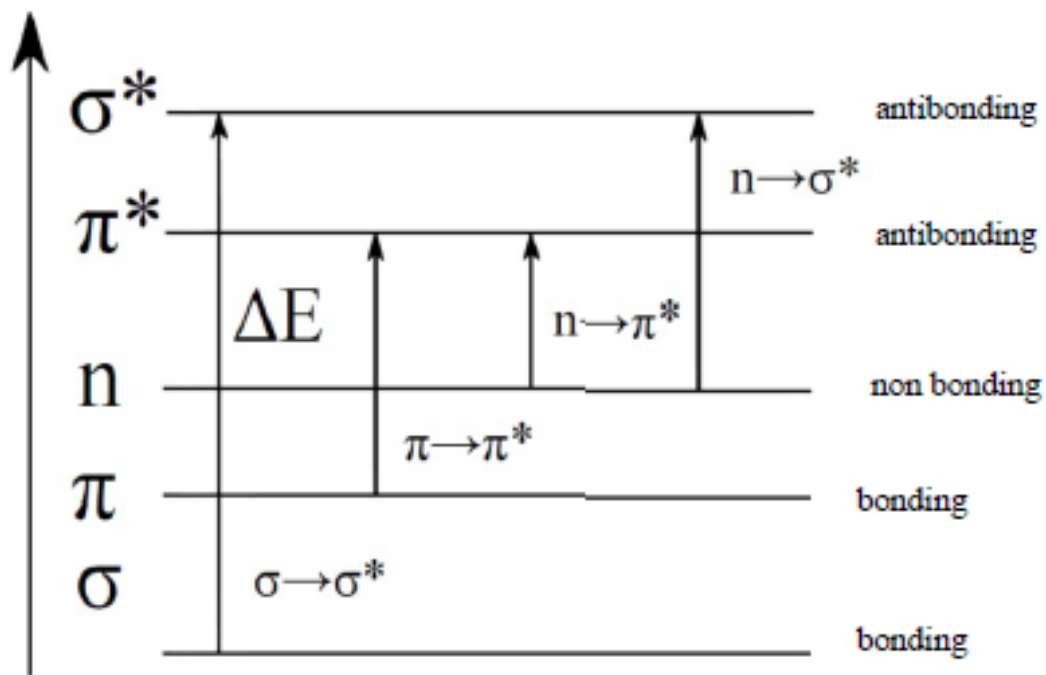


Figure 2.11: Schematic representation of the excitation of electrons by absorbance of photons of the energy ΔE ^[86]

and vibrational levels belong to the electronic states. The intensity of the absorbance bands is a measure of the concentration of the investigated sample and can be calculated by the Lambert-Beer-law:

$$E_{\lambda} = \log \left(\frac{I}{I_0} \right) = \epsilon_{\lambda} \cdot c \cdot d \quad (2.45)$$

Here E_{λ} is the extinction, c the concentration, d the layer thickness of the irradiated specimen and ϵ_{λ} the extinction coefficient.^[37,86,87]

In UV-Vis spectroscopy valence electrons are excited. According to the molecule orbital scheme, orbital cleavage splits into a binding and an antibonding orbital, like it is shown in figure 2.11. As a rule, the electrons are all in the binding orbital. Upon excitation of the valence electrons they change into the antibonding orbital.^[87]

3 Results and Discussion

The result section is divided in three parts. The first part presents the results of the investigation of nucleation and growth kinetics of ZnO nanoparticles by in situ SAXS-, WAXS- and UV/Vis-experiments. In the second part the investigation of the growth kinetics of Pd nanoparticles by in situ SAXS-experiments is discussed. The last part deals with the design development and fabrication of microfluidic chips for studying biological and medical processes.

3.1 Investigation of nucleation and growth kinetics of ZnO nanoparticles by in situ SAXS/WAXS/UV-Vis-experiments

3.1.1 Microfluidic synthesis of ZnO nanoparticles

The synthesis of the ZnO nanoparticles was carried out according to the procedure of Ehlert et al.^[19] using the reaction of zinc oleate with tetrabutylammonium hydroxide. For this purpose, the zinc oleate (3) had to be synthesized in a first step by reacting sodium oleate (1) and zinc chloride (2), like it is shown in figure 3.1. After the preparation

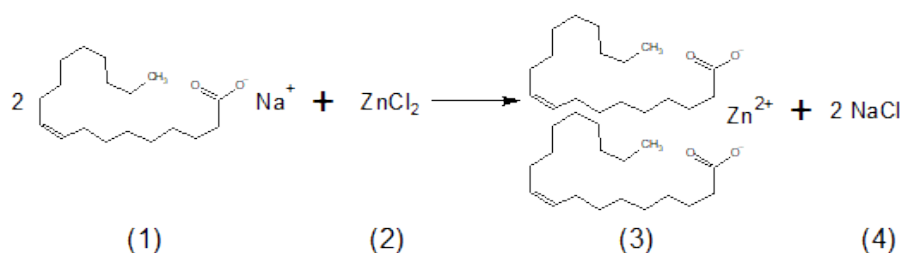


Figure 3.1: Schematic illustration of the synthesis of the zinc oleate precursor: sodium oleate (1) reacts with zinc chloride (2) to zinc oleate (3) and sodium chloride (4).

of the zinc oleate (3) this is dissolved in THF and then treated with the hydrolysis agent tetrabutylammonium hydroxide (5) to form ZnO nanoparticles (6), like it demonstrated in figure 3.2.

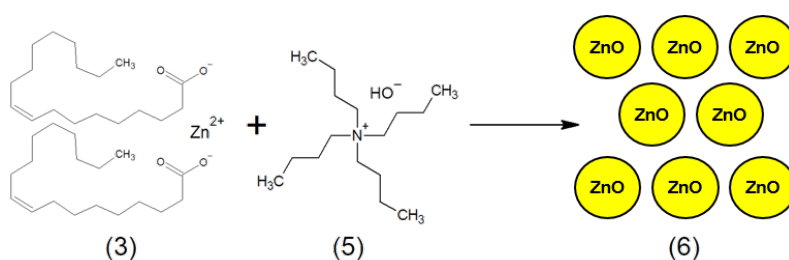


Figure 3.2: Schematic illustration of the synthesis of the ZnO nanoparticles: zinc oleate (3) reacts with tetrabutylammonium hydroxide (5) to ZnO nanoparticles (6).

For the microfluidic synthesis of this ZnO nanoparticles the two reaction solutions (oleate solution and the hydrolysis agent) were pumped with a high precision pump from neMESYS at high flow rates (see table 3.1) through a Y-shaped Teflon mixer via tubing into a quartz capillary, which is heated in a 3D-printed in situ holder integrated with a heating copper tube.

For the experiments performed during this work, there were variations in the concentration of the zinc oleate solution and the temperature at which the synthesis took place. The synthesis parameters are summarized in table 3.1.

Table 3.1: Summary of the synthesis parameters for the microfluidic ZnO-nanoparticle synthesis

Sample name	Temperature [°C]	Zn-Oleate		TBAH	
		c [mM]	flow rate [μ L/h]	c [M]	flow rate [μ L/h]
ZnO_1T_40	40	53	10000	1.0	2000
ZnO_1T_50	50	53	10000	1.0	2000
ZnO_3T_40	40	160	10000	1.0	2000
ZnO_3T_50	50	160	10000	1.0	2000

When the stationary flow conditions were reached, the pumps were stopped and the monitoring of the ZnO nanoparticles by means of SAXS/WAXS/UV-Vis techniques for 4 - 5 h begins with a dead time of approximately 3.6 s.

For longer investigation times the reaction has to be carried out in a closed quartz capillary due to the evaporation of THF at high temperatures. Therefore TBAH was added to the 2 mL zinc oleate solution. After this the capillary was filled with this reaction mixture and closed with hot glue before starting the measurements for 12 - 18 h with a dead time of approximately less than 60 s.

3.1.2 Development of the experimental construction

The initial model was a capillary holder, which was used for simultaneous SAXS/WAXS/UV-Vis measurements and with that kinetic investigations of nanoparticle syntheses have already been carried out in the group of Prof. Förster.^[15] Since the zinc oxide nanoparticles also have fluorescent properties, the design has been changed (another opening at a 90° angle was needed), so that the photoluminescence can be measured.

This design was 3D-printed using acrylonitrile butadiene styrene (ABS) and a copper tube was added to heat the capillary (see figure 3.6 B). Exemplary sketches of the design, drawn with AutoCAD, and marks of possible investigation methods, like X-ray

scattering methods and spectroscopy methods, are shown in figure 3.3.

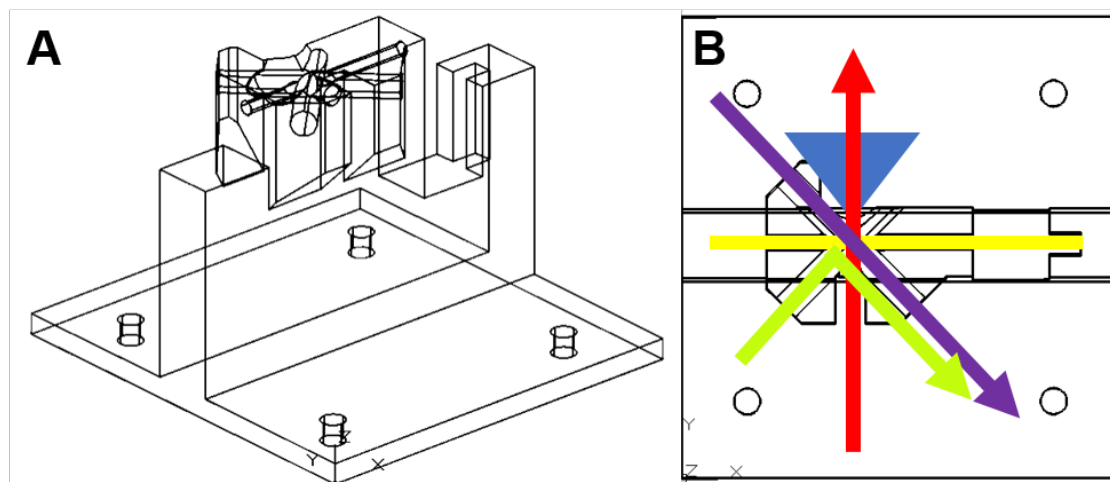


Figure 3.3: exemplary AutoCAD-sketches of the capillary holder: overall view (A) and top view (B) with marks of possible application methods (yellow - sample direction; red - SAXS; blue - WAXS; purple - UV-Vis; green - photoluminescence)

The use of plastic as the material for the capillary holder implicates a limitation on the maximum possible reaction temperature. ABS, for example, softens at a temperature of 95 -110 °C, why the operating limits are between -45 °C and 85 °C permanent temperature.^[88]

Figure 3.4 A shows, that there are differences between the temperature set at the capillary holder and the temperature measured in the capillary. As an example, figure 3.4 B shows an infrared image where it can be seen that achieving the required temperature of 40 °C in the capillary for the ZnO-nanoparticle synthesis, needs to set a temperature of 55 °C on the capillary holder.

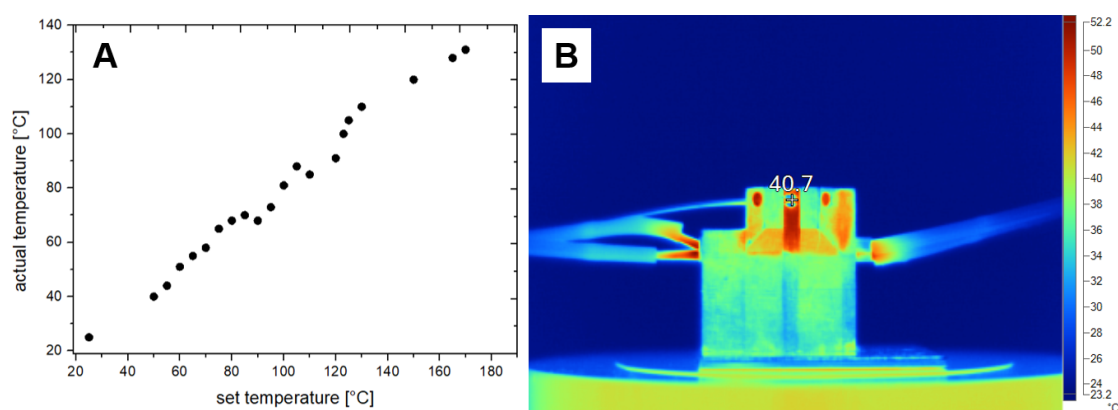


Figure 3.4: graphical illustration of the differences between the temperature set at the capillary holder and the actual temperature measured at the capillary (A) and image of a infrared camera at a set temperature of 55 °C (B)

The data from the graph in figure 3.4 A illustrates that the use of the ABS capillary holder therefore enables a maximum reaction temperature of less than 80 °C.

During this work, the state of the art in 3D printers was not yet ready to process high-temperature plastics such as polyimides. So the use of metal was the alternative way to achieve higher synthesis temperatures.

For this purpose, a capillary holder was made of copper, which can be seen in figure 3.5.

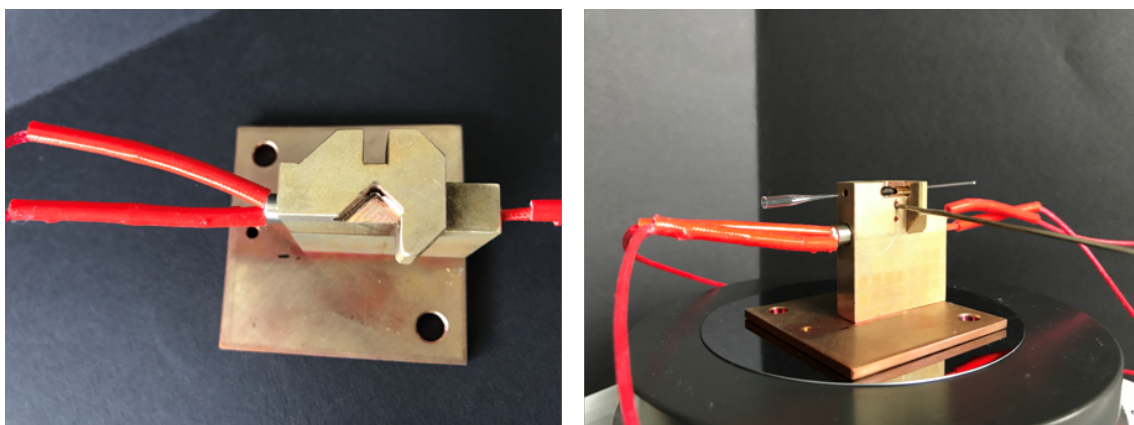


Figure 3.5: exemplary images of the capillary holder made of copper

Unfortunately, the fluorescence data of the experiments performed during this work could not be used. These experiments should have been done in an absolutely dark environment. When X-ray methods are carried out at the same time, there is always the light of a warning lamp of the system, which is also measured and thus falsifies the data.

Because of this, only the in situ SAXS-, WAXS- and UV/Vis-data were used to study the kinetics of ZnO nanoparticles.

3.1.3 Small Angle X-ray Scattering

The in situ SAXS/WAXS experiments were performed with a “Double Ganesha AIR” system. Figure 3.6 shows the experimental setup of this system (A) and the 3D-printed capillary holder (B). The X-ray source of this laboratory-based system is a rotating anode providing a microfocused beam at $\lambda = 0.154$ nm.

The scattering data were recorded by position sensitive detectors, wherein the SAXS-detector is located in an evacuated tube with a sample-distance of ca. 40 cm and the WAXS-detector has an unusual position of ca. 1.8 cm above the microfluidic cell, which is necessary to maximize the signal-noise-ratio.

For the really early stages the SAXS experiments were performed at a synchrotron at Petra III/DESY Hamburg at the beamline P03 ($\lambda = 0.093$ nm) with a sample-detector distance of 1.69 m, which setup is shown in figure 3.6 C.

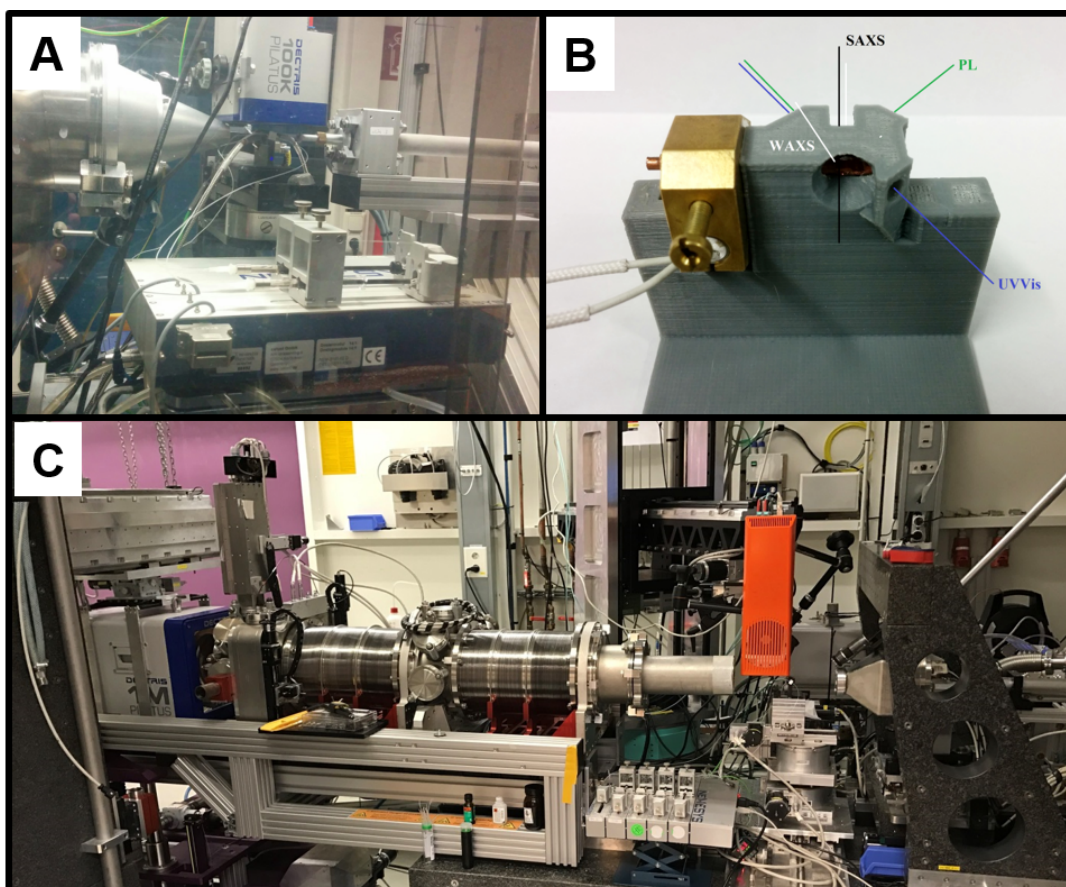


Figure 3.6: Demonstration of the experimental setup of the microfluidic ZnO-nanoparticle synthesis: experimental setup at the laboratory based Ganesha (A), closeup view of the 3D-printed in situ capillary holder integrated with a heating copper tube (B), experimental setup at Petra III/DESY Hamburg at the beamline P03.

The ZnO nanoparticles were prepared by the reaction of zinc oleate with TBAH in THF. After the reaction the oleate counterions of the zinc salt act as ligands which stabilize the growing ZnO nanoparticles.

The kinetics of the nanoparticle nucleation and growth process was investigated by time-resolved in situ SAXS/WAXS/UV-Vis-spectroscopy at two different temperatures (40 °C and 50 °C) and concentrations employing a stopped-flow microfluidic device for fast mixing. The concentrations of the zinc oleate precursor stock solutions before mixing were $[\text{Zn}^{2+}]_{\text{prec}} = 0.053 \text{ M}$ or 0.160 M in THF and $[\text{TBAH}]_{\text{prec}} = 1.0 \text{ M}$ for TBAH in THF. In the microfluidic device the stock solutions were mixed in a volume ratio $V(\text{Zn}^{2+}) : V(\text{TBAH}) = 5 : 1$, resulting in initial concentrations of $[\text{Zn}^{2+}]_0 = 0.044 \text{ M}$ or 0.133 M and $[\text{TBAH}]_0 = 0.167 \text{ M}$ in the reaction mixture

Precursor reactions at 30 °C were too slow and incomplete to obtain well defined nanoparticles and reactions at 60 °C were difficult due to fast evaporation of the THF ($T_v = 66 \text{ °C}$), which was used as the solvent.

Figure 3.7 shows the scattered intensity $I(q)$ as a function of time for two different $[\text{Zn}^{2+}]_{\text{prec}}$ -concentrations and temperatures, providing systematic information on the ZnO-nanoparticle nucleation and growth.

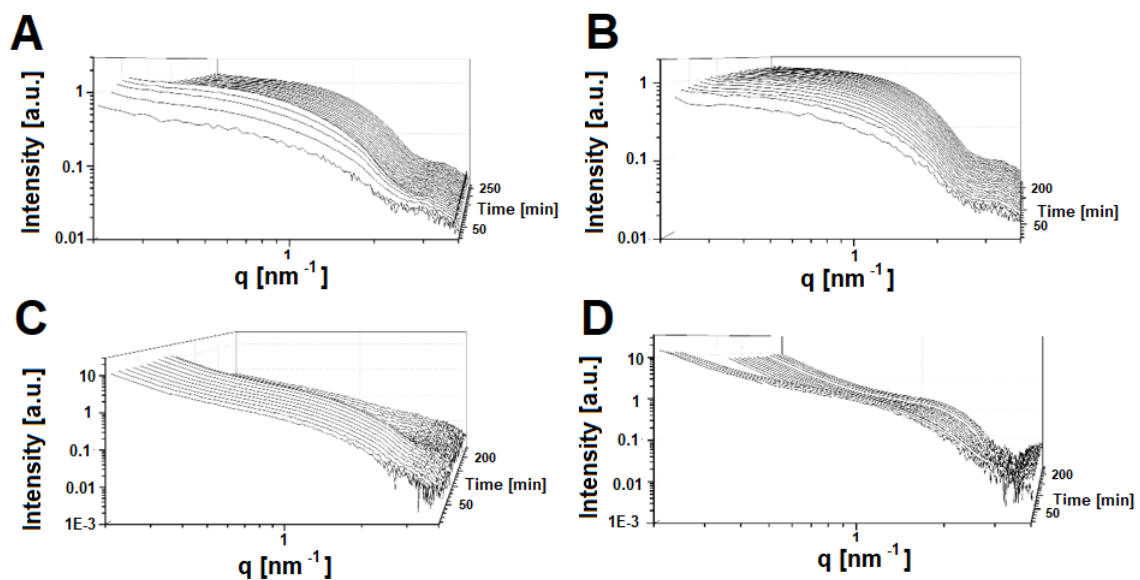


Figure 3.7: Stack-plots of the measured SAXS curves recorded in situ during the formation of the ZnO nanoparticles: A) $[\text{Zn}^{2+}]_{\text{prec}} = 160 \text{ mM}$, $T = 40 \text{ °C}$; B) $[\text{Zn}^{2+}]_{\text{prec}} = 160 \text{ mM}$, $T = 50 \text{ °C}$; C) $[\text{Zn}^{2+}]_{\text{prec}} = 53 \text{ mM}$, $T = 40 \text{ °C}$; D) $[\text{Zn}^{2+}]_{\text{prec}} = 53 \text{ mM}$, $T = 50 \text{ °C}$.

Figure 3.7 A shows the measured SAXS-curves at 40°C for a initial precursor concentration of $[Zn^{2+}]_0 = 0.133$ M and $[TBAH]_0 = 0.167$ M. A Guinier plateau at low scattering vectors q was observed, which develops into a q^{-4} -Porod decay at $q > 1$ nm⁻¹, followed by a shoulder at $q \sim 2$ nm⁻¹ corresponding to the damped formfactor oscillation of the spherical nanoparticles.

The first five measurements show a systematically increasing scattering intensity indicating the early growth phase of the nanoparticles. Subsequently, the formfactor oscillations shift to lower q indicating an increase of the nanoparticle radius during the early and late growth phase. The observation of damped formfactor oscillations indicates that narrow disperse nanoparticles were formed.

In figure 3.7 B the nanoparticle growth at a temperature of 50°C was measured for the same initial precursor concentration of $[Zn^{2+}]_0 = 0.133$ M. The measured scattering curves show the same features as for the 40 °C-measurement (3.7 A), i.e. a Guinier plateau at low q followed by a Porod-regime with a characteristic shoulder due to the formfactor oscillation. The particle growth occurs faster, as the early growth phase with the characteristic increase of the scattering intensity is already finished after 25 minutes.

To obtain information on the concentration dependence, also experiments for more diluted Zn²⁺-precursor solutions with $[Zn^{2+}]_0 = 0.044$ M keeping the TBAH-precursor concentration constant at $[TBAH]_0 = 0.167$ M were performed.

Figure 3.7 C shows the measured SAXS-curves for a temperature of 40 °C. Despite the much reduced signal-to-noise ratio, the temporal evolution of the scattering curves can still be followed, exhibiting similar characteristic features as the scattering curves measured at higher concentration. This also applies to the measurements performed at a temperature of 50 °C in figure 3.7 D.

Despite the low- q upturn due to excess scattering around the beam stop, it was still possible to quantitatively analyze the scattering curves to determine the temporal evolution of the particle radii and the polydispersity.

Performing studies in more dilute solutions required the use of synchrotron X-ray scattering. They were performed at the beamline ID02 at ESRF in Grenoble, and at the beamline P03 at PETRA-III (DESY) in Hamburg. It turned out that the high X-ray primary beam intensity of these third-generation synchrotron sources induced radiochemical side reactions in the Zn-oleate/TBAH-system, possibly involving reactions at the oleic

acid double bond. This lead to a pronounced loq-q upturns during all phases of the nanoparticle nucleation and growth process.

The four sets of SAXS-curves measured at the DESY with two Zn^{2+} -precursor concentrations (53 mM, 160 mM) and two temperatures (40 °C, 50 °C) are shown in the figure 3.8.

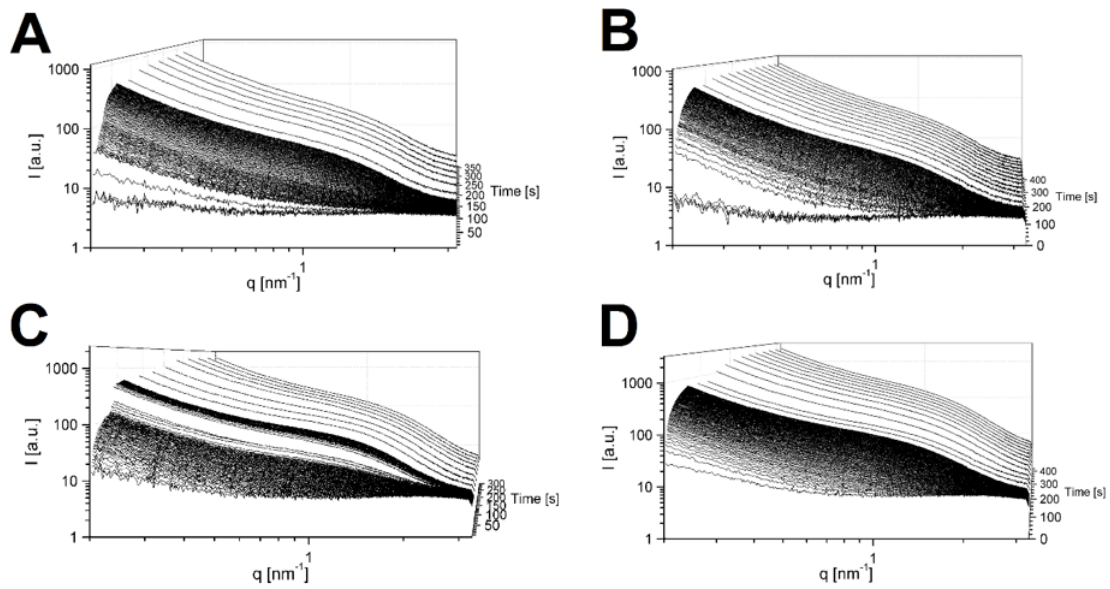


Figure 3.8: Stack-plots of the SAXS curves recorded in situ during the first 300 - 400 s of the formation of the ZnO nanoparticles at the Petra III P03-beamline: A) $[\text{Zn}^{2+}]_{\text{prec}} = 53 \text{ mM}$, $T = 40 \text{ °C}$; B) $[\text{Zn}^{2+}]_{\text{prec}} = 53 \text{ mM}$, $T = 50 \text{ °C}$; C) $[\text{Zn}^{2+}]_{\text{prec}} = 160 \text{ mM}$, $T = 40 \text{ °C}$; D) $[\text{Zn}^{2+}]_{\text{prec}} = 160 \text{ mM}$, $T = 50 \text{ °C}$.

Although it is possible to measure the scattering curves with higher temporal resolution (0.5 seconds) and higher signal-to-noise ratio, the high featureless scattering background prevented a quantitative analysis of the scattering curves to determine the particle radii.

Still the qualitative evolution of the scattering curves with an initial increase of the scattering intensity and a shift of the characteristic formfactor region to lower q can be well recognized and agrees well with the data of the SAXS-experiments measured at the Ganesha, which is presented in figure 3.9 exemplary.

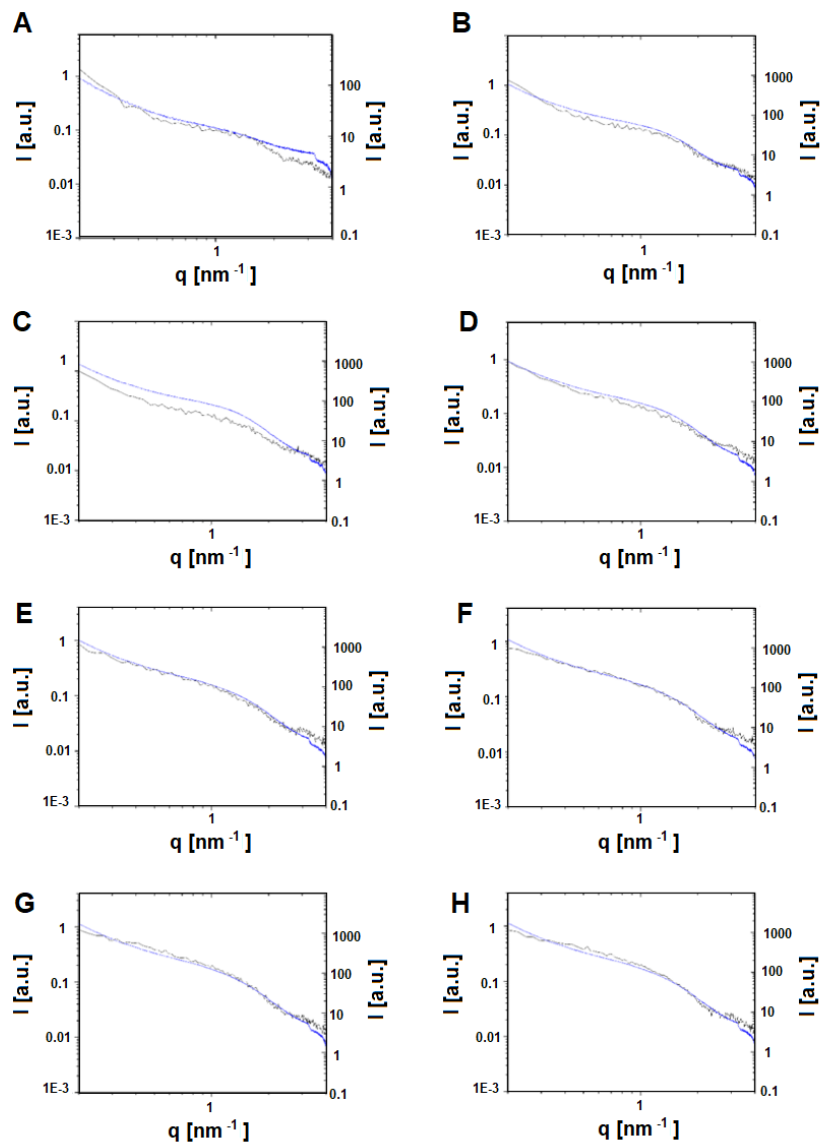


Figure 3.9: Comparison of some measurements by both beamlines of the first five minutes of the ZnO nanoparticle formation. The black graphs are the SAXS-experiments measured at the Ganesha, the blue graphs are the SAXS-experiments measured at the DESY, PETRA III P03:

- A) $[\text{Zn}^{2+}]_{\text{prec}} = 160 \text{ mM}$, $T = 40 \text{ }^\circ\text{C}$, $t = 30\text{s}$,
- B) $[\text{Zn}^{2+}]_{\text{prec}} = 160 \text{ mM}$, $T = 40 \text{ }^\circ\text{C}$, $t = 60\text{s}$,
- C) $[\text{Zn}^{2+}]_{\text{prec}} = 160 \text{ mM}$, $T = 40 \text{ }^\circ\text{C}$, $t = 90\text{s}$,
- D) $[\text{Zn}^{2+}]_{\text{prec}} = 160 \text{ mM}$, $T = 40 \text{ }^\circ\text{C}$, $t = 120\text{s}$,
- E) $[\text{Zn}^{2+}]_{\text{prec}} = 160 \text{ mM}$, $T = 40 \text{ }^\circ\text{C}$, $t = 150\text{s}$,
- F) $[\text{Zn}^{2+}]_{\text{prec}} = 160 \text{ mM}$, $T = 40 \text{ }^\circ\text{C}$, $t = 180\text{s}$,
- G) $[\text{Zn}^{2+}]_{\text{prec}} = 160 \text{ mM}$, $T = 40 \text{ }^\circ\text{C}$, $t = 240\text{s}$,
- H) $[\text{Zn}^{2+}]_{\text{prec}} = 160 \text{ mM}$, $T = 40 \text{ }^\circ\text{C}$, $t = 300\text{s}$

In the following it will thus quantitatively analyze the SAXS-curves measured at our in-house SAXS setup and provide a qualitative comparison with the synchrotron-SAXS measurements.

To further describe the data analysis, selected SAXS-curves representative for the early, middle and late stages of particle nucleation and growth are shown in figure 3.10 for the case of a Zn^{2+} -precursor concentration of $[\text{Zn}^{2+}]_{\text{prec}} = 160 \text{ mM}$ and a TBAH-precursor concentration of $[\text{TBAH}]_{\text{prec}} = 1 \text{ M}$ at $40 \text{ }^\circ\text{C}$, as shown in figure 3.7 A.

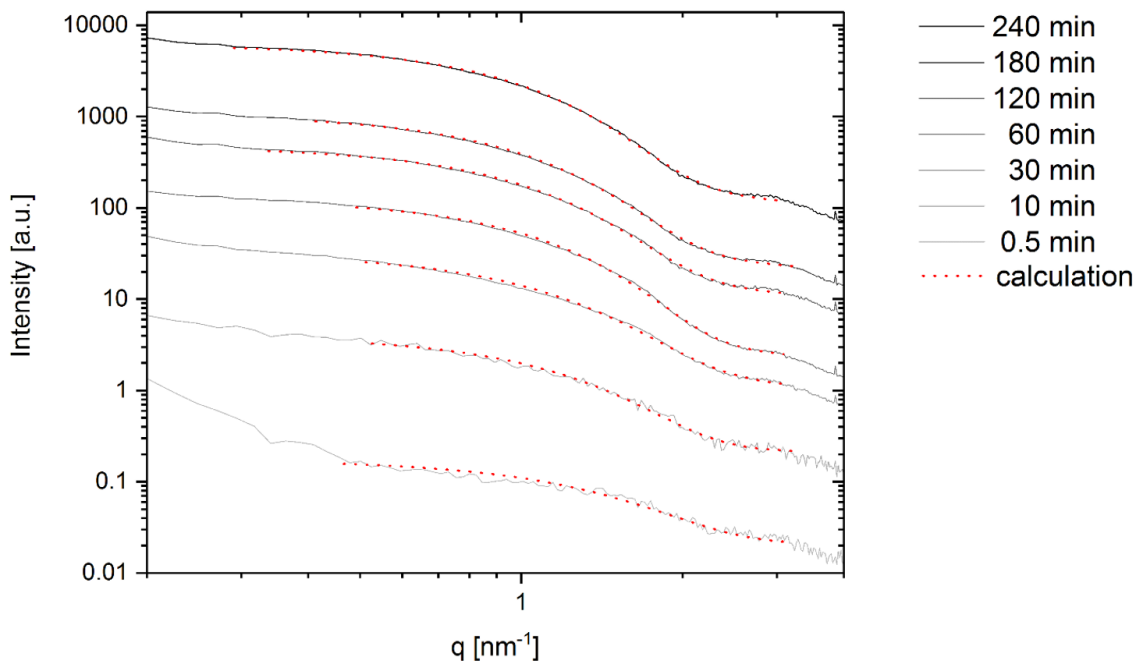


Figure 3.10: Selected SAXS-curves of the ZnO nanoparticle formation at $40 \text{ }^\circ\text{C}$ with a Zn^{2+} -precursor concentration of $[\text{Zn}^{2+}]_{\text{prec}} = 160 \text{ mM}$ at different times measured at the Ganesha-beamline. The dotted red lines indicate the fits to the measured scattering curves.

The scattering curves are fitted to an analytical expression of the formfactor of poly-disperse homogeneous spheres

$$I(q) = (b_1 - b_2)^2 \rho_N \left\langle \frac{9}{(qR)^6} [(\sin(qR) - qR \cos(qR))]^2 \right\rangle, \quad (3.1)$$

where R is the radius of the nanoparticles, $\langle \dots \rangle$ denotes the average over the Schulz-Zimm-distribution with a weighting factor R^6 to account for weight-averaged scattered intensity.

The fitted curves are indicated by the red solid lines showing very good agreement with the experimentally determined scattering curves except for the very first measurement where low- q scattering intensity hides part of the Guinier region, which nevertheless can still be determined with good precision.

From the fits the scattered intensity $I(0)$, the mean radius of the particles \bar{R} and the relative polydispersity σ are obtained. The polydispersity is in the range of 0.13 – 0.16 for all scattering curves.

The temporal evolution of the particle radii as a function of time is shown figure 3.11. An early growth stage where the particle radii increase from 1.5 nm to 2.2 nm with the first 500 seconds for temperatures of 40 °C and within the first 200 seconds for temperatures of 50 °C is observed.

Later the particle radii stay constant over several hours, indicating the good long-term stability of the ZnO nanoparticles synthesized according to the described protocol.

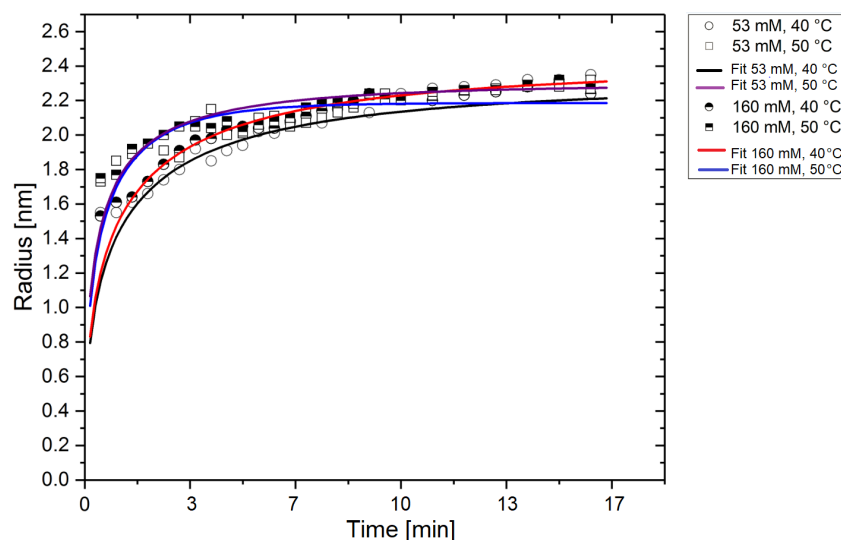


Figure 3.11: Time evolution of the average ZnO nanoparticle radius determined from the fitted SAXS-curves for the different concentrations and temperatures investigated in the present study. (up to 240min, constant)

3.1.4 Nucleation and growth model

The growth curves were quantitatively analyzed by a nucleation and growth model which was recently successfully applied to the growth of Au-nanoparticles. The following chemical reaction is considered



and leads to the formation of the ZnO nanoparticles.

The kinetic model is formulated in terms of the time dependence of the concentrations of the precursors $[\text{Zn}^{2+}]$, $[\text{OH}^-]$, of free solvated ZnO-units $[\text{ZnO}]$, of ZnO-units incorporated into nanoparticles by nucleation $[\text{ZnO}_N]$ or by growth onto earlier formed nanoparticles J $[\text{ZnO}_{PJ}]$, as well as in terms of the particle concentrations $[P]$ during the nucleation and growth period.

It corresponds to a set of coupled first order differential equations with respect to the ionic components

$$\begin{aligned} \frac{d[\text{Zn}^{2+}]}{dt} &= -k_1 [\text{Zn}^{2+}] [\text{OH}^-] \\ \frac{d[\text{OH}^-]}{dt} &= -k_1 [\text{Zn}^{2+}] [\text{OH}^-] \\ \frac{d[\text{ZnO}]}{dt} &= k_1 [\text{Zn}^{2+}][\text{OH}^-] - \beta \frac{V}{\nu_0} \exp\left[-\frac{\Delta G_c}{kT}\right] - \int_0^t 4\pi R_J D N_A [\text{ZnO}] \frac{\left(1 - \frac{[\text{ZnO}]_{\text{sat}} \exp\left[\frac{R_{\text{cap}}}{R_J}\right]}{[\text{ZnO}]}\right)}{\left(1 + \frac{D}{R_J k_{gr}}\right)} h(t_j) dt_J \\ \frac{d[\text{ZnO}_N]}{dt} &= \beta \frac{V}{\nu_0} \exp\left[-\frac{G_c}{kT}\right] \\ \frac{d[\text{ZnO}_{PJ}]}{dt} &= 4R_J D N_A [P_J] [\text{ZnO}] \frac{\left(1 - \frac{[\text{ZnO}]_{\text{sat}} \exp\left[\frac{R_{\text{cap}}}{R_J}\right]}{[\text{ZnO}]}\right)}{\left(1 + \frac{D}{R_J k_{gr}}\right)}, J = 1, \dots, N \\ \frac{d[P_J]}{dt} \Big|_{t=t_j} &= \beta \exp\left[-\frac{\Delta G_c}{kT}\right] \delta [t - t_J] = h(t_j) \end{aligned} \quad (3.3)$$

where $\delta [t - t_j]$ is the delta function used to describe the concentration of a new nu-

cleated species $[P_j]$, which is determined by the amount of $[ZnO_N]$ produced at $t = t_j$.

k_1 is the rate constant of the chemical reaction, k_{gr} the rate constant of the growth reaction, V the volume of the spherical particle related to the particle radius by $V = \frac{4}{3}\pi R^3$ and $\nu_0 = \frac{M}{\rho N_A} \approx 2.41 \cdot 10^{-29} m^3$ is the molar volume of a ZnO-unit, calculated from its molar mass M , the ZnO bulk density ρ , and Avogadro's constant N_A .

$\beta = \frac{4}{9} \frac{k_B T}{\eta \nu_0}$ is the rate constant of the nucleation reaction, calculated from Boltzmann's constant k_B and the solvent viscosity η , $D = \frac{k_B T}{6 \pi \eta R}$ the diffusion constant of the ZnO-units, γ the interfacial tension of the ZnO nanoparticles and $[ZnO]_{sat}$ the saturation concentration of ZnO.

The nucleation free enthalpy is given by

$$\Delta G_c(t) = \frac{16\pi\gamma^3\nu_0^2}{3(k_B T)^2 (\ln S(t))^2} \quad (3.4)$$

where $S = \frac{[ZnO]}{[ZnO]_{sat}}$ is the supersaturation.

A priori known parameters are the molar mass M of ZnO ($M = 81.41$ g/mol), the bulk density ρ of ZnO (5.61 g/mol) and the solvent viscosity η (0.46 mPas).

Unknown values are the rate constant k_1 of the chemical reaction (equ. 4.2), the growth rate constant k_{gr} , the interfacial tension γ of the ZnO nanoparticles, and the saturation concentration $[ZnO]_{sat}$ of ZnO, whose values are fitted to the experimental data in figure 3.11.

Solving this set of coupled differential equations yields the concentrations $[P_j](t)$ and radii $R_j(t)$ of all particles J that have been formed during the nucleation process, from which the size distribution $h(R,t)$, the mean radius $\bar{R}(t)$ and the relative standard deviation $\sigma_R(t)$ can be obtained and compared to the experimental data. Details of the calculations are given by X. L. Chen^[15].

Table 3.2 shows the values of k_1 , k_{gr} , γ and $[ZnO]_{sat}$ for which the best agreement with the measured growth case was obtained.

The surface tension of ZnO/THF was the same for all measurements with a value of $\gamma = 205$ mN/m. This can be compared to a value of $\gamma = 470$ mN/m, which was determined for ZnO/ethanol. Ethanol has a slightly worse solvent quality for ZnO

Table 3.2: Values for k_1 , k_{gr} , γ and $[ZnO]_{sat}$ for which the best fit to the experimental data was obtained

Temperature [°C]	$[Zn^{2+}]_0$ [M]	k_1 [m ³ /Ms]	k_{gr} [m ³ /Ms]	γ [mN/m]	$[ZnO]_{sat}$ [M]
40	0.044	$3 \cdot 10^{-5}$	$6 \cdot 10^{-6}$	205	$1 \cdot 10^{-7}$
40	0.133	$3 \cdot 10^{-5}$	$7.5 \cdot 10^{-6}$	205	$1 \cdot 10^{-7}$
50	0.044	$7 \cdot 10^{-5}$	$2 \cdot 10^{-5}$	205	$1 \cdot 10^{-7}$
50	0.133	$7 \cdot 10^{-5}$	$2.7 \cdot 10^{-5}$	205	$1 \cdot 10^{-7}$

compared to THF, therefore a higher value is expected.

For the value for the saturation concentration the same value of $[ZnO]_{sat} = 1 \cdot 10^{-7}$ M was used for all experiments, which is nearly the same value reported in literature, i.e. $[ZnO]_{sat} = 2.2 \cdot 10^{-1}$ M.^[22]

The precursor reaction rates (equ. 3.2) are concentration independent and in the order of $k_1 \sim 5 \cdot 10^{-5}$ m³/Ms, increasing with increasing temperature. As outlined by X. L. Chen^[15] initiating the nucleation process, the time at which a critical saturation of $S \sim 100$ is reached, can be estimated as

$$\tau_{nuc} = \frac{S[ZnO]_{sat}}{k_1 [Zn^{2+}]_0 ([Zn^{2+}]_0 - S[ZnO]_{sat})} \quad (3.5)$$

which is in the order of $\tau_{nuc} \sim 20$ s, which is in a good agreement with the reaction time where the first nanoparticles could be observed.

Similarly, the radius of the critical nucleus can be calculated as $R = \frac{2 \gamma \nu_0}{k T \ln(S)} = 0.50$ nm.

The measured growth rates increase slightly with increasing concentration and moderately with temperature and are in the order of $k_{gr} \sim 1 \cdot 10^{-5}$ m/s. Thus, they are an order of magnitude faster compared to values measured for the growth of Au-nanoparticles in toluene ($k_{gr} \sim 1 \cdot 10^{-6}$ m/s), likely because the activation process for growth is lower across the oleate/solvent stabilization layer.

From the temperature dependence of the rate constants it is estimated that the activation energy is ca. ~ 100 kJ/mol, which is somewhat larger than determined for Au-nanoparticle formation, thus confirming the higher energy activation process.

After around 17 minutes, the ZnO-nanoparticles increase in size only very slightly, by less than 0.2 nm, over a period of 4.5 hours as shown in figure 3.12.

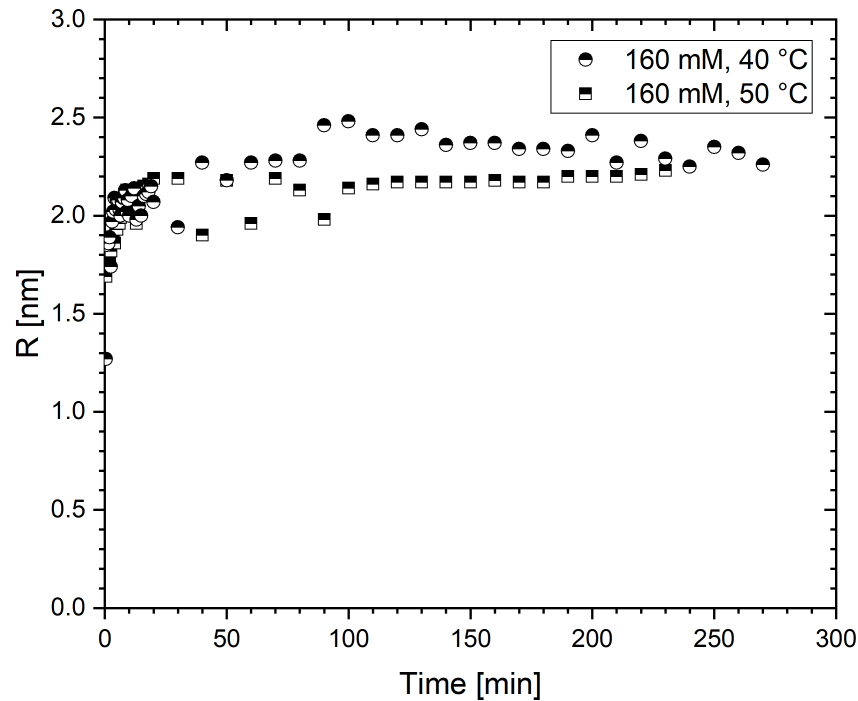


Figure 3.12: Time evolution of the average ZnO-nanoparticle radius over a period of 270 min

This demonstrates the good stability of the ZnO nanoparticles provided by the oleate ligands. From the numerical analysis it follows that the Zn^{2+} -precursor is consumed to about 3 % of its initial concentration after around 33 minutes, thus nearly full conversion has been achieved.

It was observed that at a lower temperature the particle size is larger. This is related to an increasing k_{gr}/k_1 - ratio with increasing temperature (see table 3.2), which corresponds to a faster growth in relation to nucleation, thus leading to larger particles.

The investigation of the nucleation and growth kinetics of zinc oxide nanoparticles using in situ SAXS / WAXS / UV-Vis experiments were performed by a developed experimental setup on a lab-based SAXS/WAXS instrument. The in situ investigations of nucleation and growth were performed over time scales from 30 s up to 18 h and follows the classical model.

3.1.5 Crystallinity

With the WAXS detector positioned close to the sample it was possible to simultaneously detect also the wide-angle X-ray diffraction during the ZnO nanoparticle growth process. A Wurzite structure (space group P63mc) with lattice constants $a = 3.31$ and $c = 5.22$ was observed, which is in very good agreement with literature values $a = 3.250$ and $c = 5.207$ of bulk ZnO.^[20]

Due to the low wide-angle scattering intensity we had to measure in 20 min. frames, thus on considerably longer time scales compared to the SAXS-experiments, up to 12 – 18 hours. Figure 3.13 presents an example of the time-evolution of the WAXS curves measured during the nanoparticle growth.

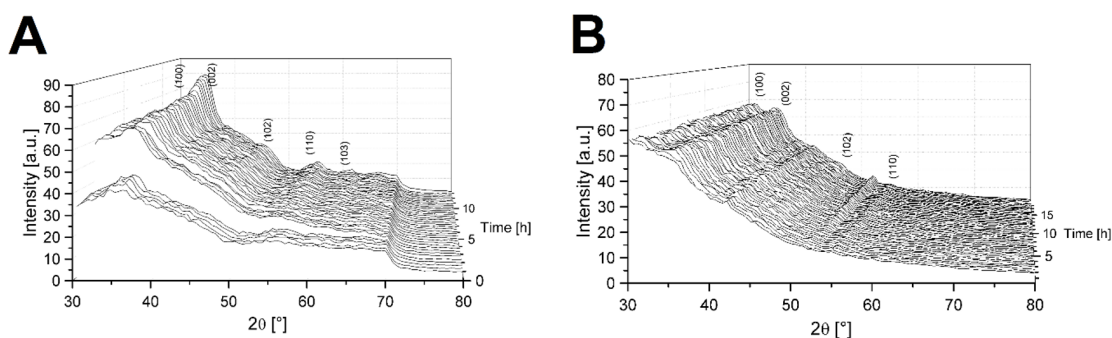


Figure 3.13: Three-dimensional plot of the time-dependent WAXS-curves recorded in situ during the formation of the ZnO nanoparticles with a concentration of 160 mM at 40 °C (A) and 50 °C(B).

During the first hour only weak, broad first-order peaks were observed. The single broad peak measured during the first frame was analyzed by fitting to a Gaussian peak function (see figure 3.14) to derive a crystalline peak domain size of 0.65 nm, which is of the order of the size of the unit cell.

The nanoparticles are therefore considered initially in an amorphous state. During the subsequent reaction time in the second growth phase, the intensity of the WAXS signals increased and well-defined first and higher-order signals indicating a Wurzite structure can be observed.

This can also be seen in figure 3.15, where some exemplary two-dimensional WAXS images of the formation of the ZnO nanoparticles with a concentration of $[Zn^{2+}]_{prec} = 160$ mM at 40 °C are summarized.

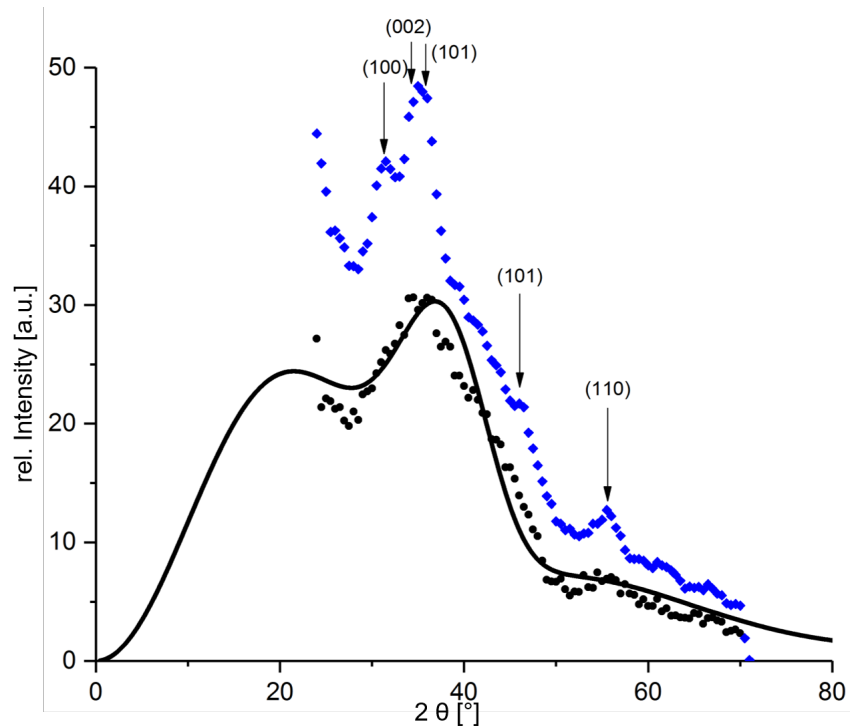


Figure 3.14: Wide-angle diffraction data for the first 20 min frame (black symbols) and after ten hours (blue symbols). The solid line is the fit to determine the mean crystalline domain size $D = 0.65$ nm using a Gaussian peak shape.

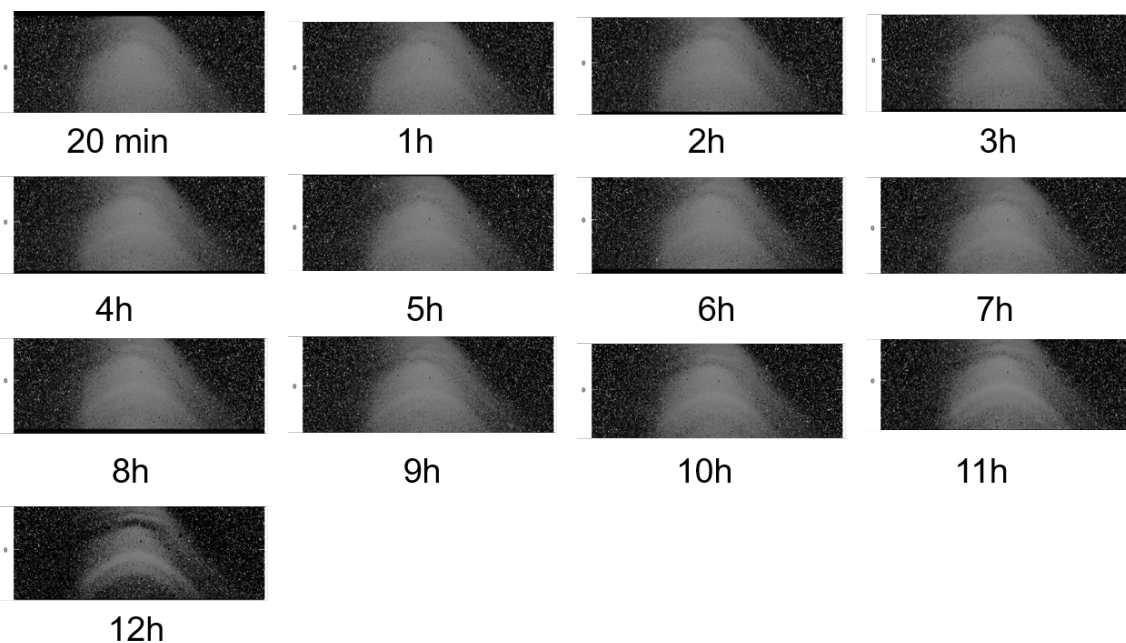


Figure 3.15: Exemplary selection of two-dimensional time-dependent WAXS images of the in situ measurements of the formation of the ZnO nanoparticles with a concentration of $[\text{Zn}^{2+}]_{\text{prec}} = 160$ mM at 40°C .

From the peak widths at the end of the reaction time it was possible to calculate the mean particle diameter using the Scherrer-equation^[89]:

$$B = \frac{K \cdot \lambda}{d \cdot \cos(2\theta)}, \quad (3.6)$$

where B is the half-width of the diffraction peak, λ is the wavelength of the x-rays, d is the particle diameter, 2θ is the scattering angle (in radian measure) and K is a numerical constant for which Scherrer obtained the value $2 \left(\frac{\ln 2}{\pi}\right)^{0.5} = 0.93$.

Using the example with a concentration of 160 mM at 40 °C of the (002)-peak at 35.5 ° after 4 hours, a particle diameter of 4.7 nm is obtained. This is nearly consistent by comparison with the SAXS-data (4.5 nm).

3.1.6 UV-Vis spectroscopy

The UV-Vis-spectra was also measured using the capillary and fiber optics during particle synthesis and parallel to the X-ray-scattering measurements. UV-Vis-measurements with a good signal-to-noise ratio could only be obtained for the highest used concentration $[Zn^{2+}]_{prec} = 160$ mM. The absorbance spectra are shown in figure 3.16.

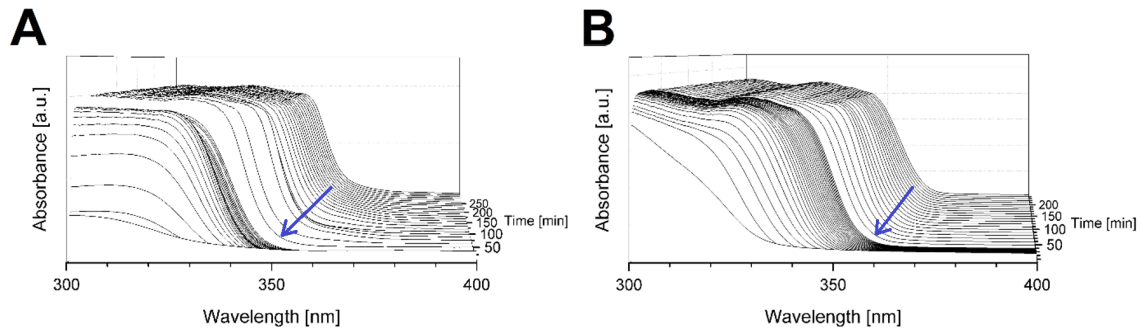


Figure 3.16: Three-dimensional plot of the UV-Vis spectra as a function of time recorded in situ during the formation of the ZnO nanoparticles with a $[Zn^{2+}]_{prec}$ -concentration of 160 mM at 40 °C (A) and 50 °C (B). The blue arrows indicate exemplary turning points, which determination was used to calculate the bandgap.

The WAXS-data indicate a crystallization process during the second growth phase, that sets in after one hour, which is the time after which the initial nucleation and growth process has been finished and the precursor nearly fully consumed. It was also observed that the UV/Vis-spectra measured in-situ during particle synthesis indicate a crystallization process that sets in after one hour.

For both temperatures a two-stage process was clearly observed, where first the UV-absorbance increases with the formation of an absorbance edge at $\lambda = 340$ nm, which after ca. 60 min shifts to larger values towards a plateau value of $\lambda = 360$ nm.

From the positions of the absorbance edges one can calculate the band gap

$\Delta E_g(d) = E_g(d) - E_g^0$ using the following equation^[20]

$$\Delta E_g = 100 \cdot (18.1 \cdot d^2 + 41.4 \cdot d)^{-1} \quad (3.7)$$

where $E_g(d)$ is the bandgap of the nanoparticle of a diameter d and E_g^0 is the bulk band gap with a value of 3.37 eV. The positions of the absorption edges represent the turning points of the respective graphs. The respective turning point was determined by linear extrapolation. The equation 3.7 can be inverted to obtain the diameter, which is plotted in figure 3.17.

As it can be seen in figure 3.17 A, the band gap decreases from 3.8 eV to 3.5 eV,

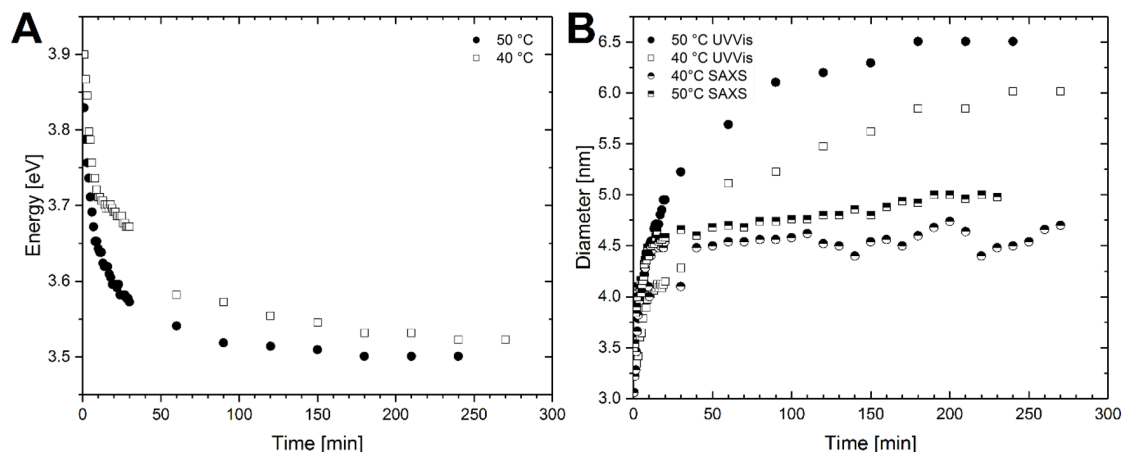


Figure 3.17: Time evolution of the band gap energy (A) and the diameter (B) determined from the UV-vis spectra (including a comparison with the SAXS data in B) of the ZnO nanoparticles with a concentration of 160 mM at different temperatures.

which still is significantly larger compared to the bulk band gap of 3.37 eV^[90] due to the quantum confinement effect.

Figure 3.17 B shows the time dependence of the calculated particle diameter of the UV-vis-data. In agreement with the SAXS- and WAXS-data a larger radii with increasing temperature due to the increasing growth rate was observed as expected.

The conclusion of these results is that albeit the relative increase of the particle radii in the second growth process is very small, it profoundly affects the UV-Vis spectra and the crystallinity as observed in the WAXS-curves. This indicates that the particles formed after the initial nucleation and growth phase develop full crystallinity in the second growth process.

Caetano et al. suggested a healing/internal crystal rearrangement process that would very well explain this observation, as well as the irregular nanoparticle shapes observed with electron microscopy.^[40]

3.1.7 Transmission electron microscopy

For a characterization of the nanoparticles after the synthesis transmission electron microscopy (TEM) was used. For this, the final nanoparticle solutions of the nucleation and growth studies were transferred onto carbon-coated copper grids, blotted and dried for investigation by TEM.

Figure 3.18 shows TEM-images of the undiluted samples of the obtained nanoparticles for the two concentrations and two temperatures. The individual nanoparticles were measured and evaluated using the "Image J" software.

For all samples nearly spherical nanoparticle shapes with a narrow size distribution were observed, confirming the results from the SAXS-, WAXS- and UV-Vis-experiments.

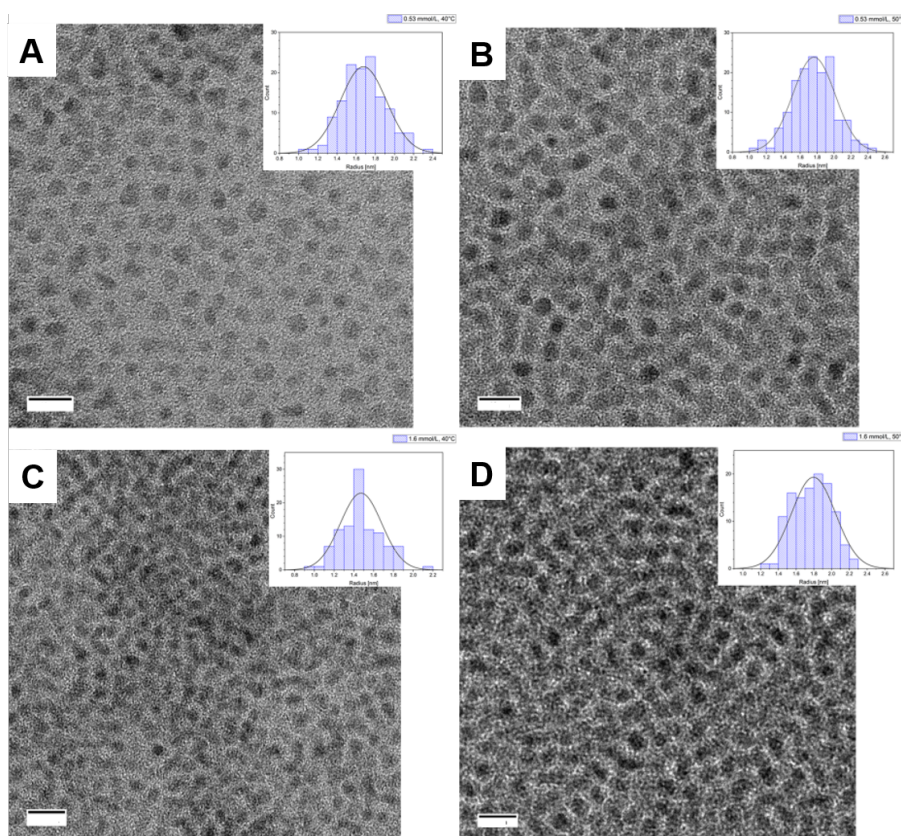


Figure 3.18: TEM-images of ZnO nanoparticles with an average particle diameter between 3 nm and 4 nm: A) $[\text{Zn}^{2+}]_{\text{prec}} = 53 \text{ mM}$, $T = 40 \text{ }^\circ\text{C}$, B) $[\text{Zn}^{2+}]_{\text{prec}} = 160 \text{ mM}$, $T = 40 \text{ }^\circ\text{C}$, C) $[\text{Zn}^{2+}]_{\text{prec}} = 53 \text{ mM}$, $T = 50 \text{ }^\circ\text{C}$, D) $[\text{Zn}^{2+}]_{\text{prec}} = 160 \text{ mM}$, $T = 50 \text{ }^\circ\text{C}$. [scale bar: 10 nm]

For the average particle size after a finished synthesis it is obtained that it increases slightly with higher precursor concentration $[\text{Zn}^{2+}]_{\text{prec}}$ and reaction temperature.

For $[\text{Zn}^{2+}]_{\text{prec}} = 53 \text{ mM}$ the average particle size decreases slightly from 1.6 nm to 1.5 nm

(figure 3.18 A and C) and for $[\text{Zn}^{2+}]_{\text{prec}} = 160 \text{ mM}$ there is an increase from 1.7 nm to 1.8 nm (figure 3.18 B and D).

The results of the evaluation of the TEM-images are summarized in table 3.3.

Table 3.3: Summary of the results of the evaluation of the TEM-images

TEM-image	$[\text{Zn}^{2+}]_{\text{prec}}$	temperature	particle size
figure 3.18 A	53 mM	40 °C	1.6 nm
figure 3.18 B	160 mM	40 °C	1.7 nm
figure 3.18 C	53 mM	50 °C	1.5 nm
figure 3.18 D	160 mM	50 °C	1.8 nm

This results are in line with the increase of the growth rate with increasing temperature. It was noted that the diameter of the nanoparticles as determined by TEM after synthesis is significantly lower compared to the values measured during the nucleation and growth period (figure 3.10) up to 4.2 nm, which is attributed to a low electron transmission contrast of the outer edge of the nanoparticles.

3.2 Investigation of the growth kinetics of Pd nanoparticles by in situ SAXS-experiments

3.2.1 Synthesis of Pd nanoparticles

The synthesis of the Pd nanoparticles was carried out according to the procedure of Mazumder and Sun.^[27] For this purpose, the reduction of palladium(II) acetylacetonate (1) in oleylamine (2) and borane tert-butylamine complex (4) was used to form spherical Pd nanoparticles (6), like it is schematic illustrated in figure 3.19.

Oleylamine served not only as a solvent but also as a surfactant and as well as a reducing agent. The BTB-complex was used as a coreductant.^[27]

According to Nui et al.^[91], it is assumed that the formation of Pd nanoparticles proceeds through a three-step mechanism: intermediate formation (3), nucleation (5) and growth (6).

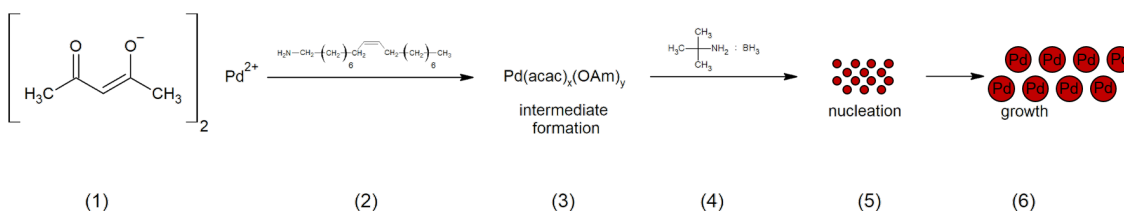


Figure 3.19: Schematic illustration of the synthesis of the palladium nanoparticles: Pd(acac)₂ (1) reacts with OAm (2) and BTB (4) to Pd nanoparticles (6).

For the experiments performed during this work, there were variations in the concentration of the BTB-complex, the synthesis temperature and the heating rate. The synthesis parameters are summarized in table 3.4.

Table 3.4: Summary of the synthesis parameters for the Pd-nanoparticle synthesis

Sample name	Pd(acac) ₂ c [mM]	BTB c [M]	start temperature [°C]	end temperature [°C]	heating rate [°C\min]
Pd-MM_01	16.41	1.14	60	90	3
Pd-MM_02	16.41	1.14	60	90	6
Pd-MM_03	16.41	0.57	60	90	3
Pd-MM_04	16.41	0.57	60	90	6
Pd-MM_06	16.41	1.14	60	70	3
Pd-MM_07	16.41	1.14	60	70	6
Pd-MM_08	16.41	0.57	60	70	3
Pd-MM_09	16.41	0.57	60	70	6

For the syntheses of this Pd nanoparticles, the Pd(acac)₂-solution was added to the BTB-solution in a volume ratio of 5 to 1. After this a quartz capillary was filled with ca. 1 mL of this reaction solution and closed with hot glue before starting the heating in a heating cell from Linkam.

When the heating was started, the monitoring of the Pd nanoparticles by SAXS at a synchrotron at Petra III/DESY Hamburg at the beamline P03 for ca. 45 min begins with a dead time of approximately less than 4 min.

3.2.2 Development of the experimental construction

The initial idea was to perform this Pd-nanoparticle synthesis in a microfluidic chip due to the solvent stability of the PDMS towards the OAm. The photos in figure 3.20 A and 3.20 C show the experimental setup for this way to synthesize Pd nanoparticles microfluidically.

In preliminary experiments Pd nanoparticles could be successfully synthesized, like it is seen in both images. Two different heating methods were tested. Figure 3.20 A shows the setup with self-made Kapton heating foils.

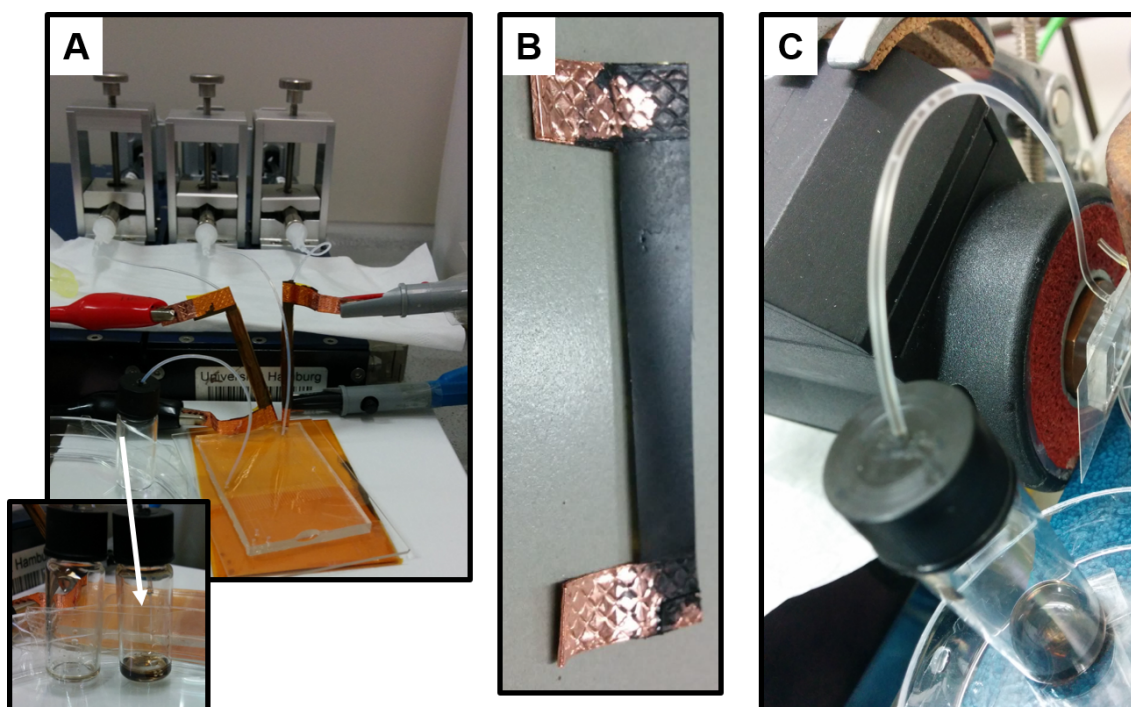


Figure 3.20: Photos of the experimental setup for Pd nanoparticle synthesis in a two-dimensional PDMS glass microfluidic chip with different heating methods for the tubes: A) self-made Kapton heating foils [with a close-up view of this (B)], C) copper heating block.

For producing the heating foils, an example is shown in figure 3.20 B, a heating varnish was applied between two copper contacts on a Kapton foil and dried.

As soon as a voltage is applied to the copper contacts, current flows through the heating varnish and the surface that is coated with it heats up. A heating varnish from *Future Carbon* was applied - a one-component varnish *ACR-100* with a heating capacity up to 100 °C. The advantage of this method was that the tubes, which direct the educts into the microfluidic chip, could be heated individually.

However, the disadvantage of the large heat loss prevailed. Therefore, the tubes were heated in a copper block. This method heats all tubes simultaneously, as shown in figure 3.20 C. But there was still the problem of accurately controlling the reaction temperature in the mixing cross of the microfluidic chip.

As a result, the experimental construction was changed to this capillary-holder-model in which the ZnO nanoparticles were already microfluidically synthesized during this work and investigated in situ for example with X-ray scattering methods. For this synthesis the two reaction solutions ($\text{Pd}(\text{acac})_2$ and BTB) were pumped with a high precision pump from neMESYS at high flow rates in a ratio of 5 to 1 ($\text{Pd}(\text{acac})_2$ -solution to BTB-solution) through a Y-shaped Teflon mixer via tubing into a quartz capillary, which is heated in a 3D-printed in situ holder integrated with a heating copper tube.

Figure 3.21 shows an image of a infrared camera. As already described in chapter 3.1.2, a much higher temperature has to be applied to the heating block in order to reach the desired reaction temperature.

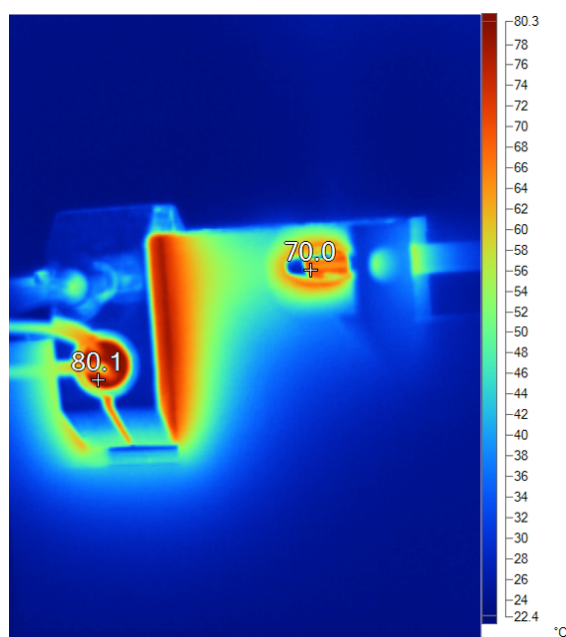


Figure 3.21: Image of a infrared camera at set temperature of 80 °C for reaching 70 °C as a reaction temperature for the Pd nanoparticle synthesis

In order to reach 70 °C (90 °C) as the reaction temperature, a temperature of 80 °C (110 °C) had to be applied to the heating block. Gas evolution occurred during this synthesis and caused problems in the SAXS measurements. It made no difference whether the synthesis was carried out with continuous flow or stop flow. Therefore, the syntheses were finally carried out in a closed capillary.

The SAXS measurements of Pd-nanoparticle syntheses in a closed quartz capillary were performed in a heating cell from Linkam at the synchrotron at Petra III/DESY in Hamburg at the beamline P03 by Dr. Sascha Ehlert and Vanessa Leffler during my parental leave.

The planning of the experiments and the evaluation as well as the analysis of the experimental data were done by me.

The experimental setup is shown in figure 3.22. The red frame marks the heating cell.

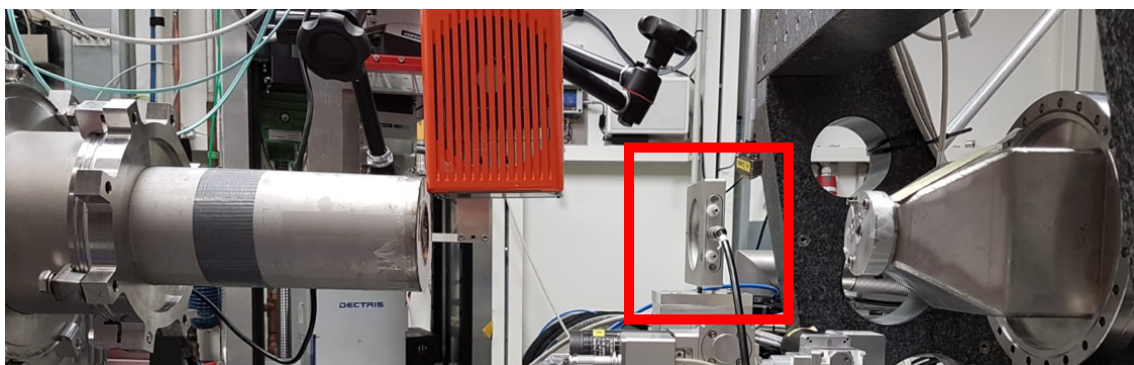


Figure 3.22: Demonstration of the experimental setup for the Pd nanoparticle synthesis in a closed quartz capillary in a heating cell (marked with a red frame) at the synchrotron. This photo was made and provided by Vanessa Leffler.

3.2.3 Small Angle X-ray Scattering

The in situ SAXS experiments were performed at a synchrotron at Petra III/DESY in Hamburg at the beamline P03 ($\lambda = 0.095$ nm) with a sample-detector distance of 1.66 m. The Pd nanoparticles were prepared by the reaction of $\text{Pd}(\text{acac})_2$ with BTB in OAm. After the reaction the oleylamine acts as ligands which stabilize the growing Pd nanoparticles. The kinetic of the growth process was investigated by time-solved in situ SAXS at different temperatures, concentrations and heating rates.

Figure 3.23 shows the time resolved SAXS intensity as a function of the scattering vector q for two different BTB-concentrations and heating rates at a synthesis temperature of 90 °C and figure 3.24 the measured SAXS-curves for the same conditions at a temperature of 70 °C.

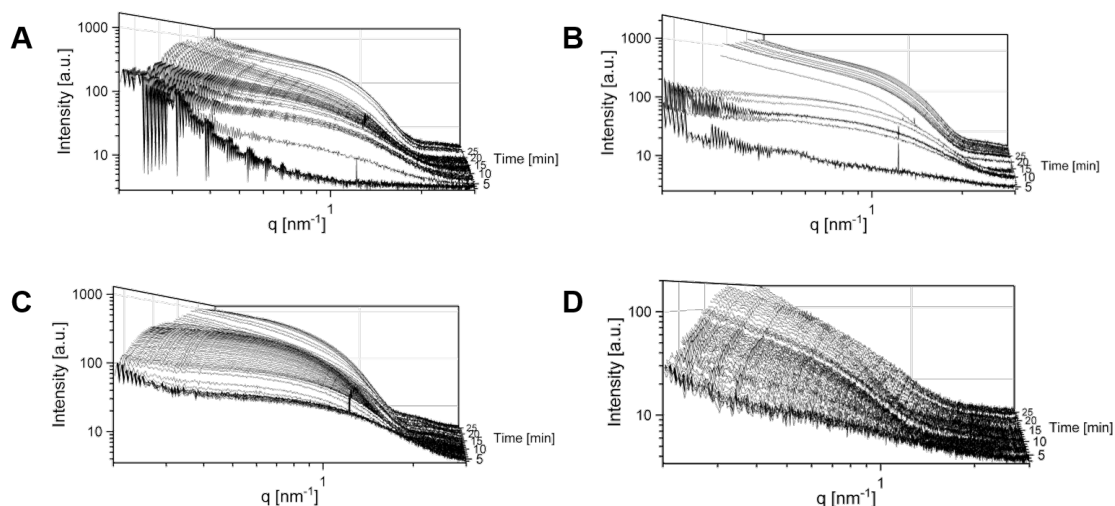


Figure 3.23: Stack-plots of selected measurement data of the SAXS-curves recorded in situ during the formation of the Pd nanoparticles at a temperature of 90 °C: A) $[\text{Pd}^{2+}]_{\text{prec}} = 16.41$ mM, $[\text{BTB}]_{\text{prec}} = 1.14$ M, $\Delta T = 3$ °C/min; B) $[\text{Pd}^{2+}]_{\text{prec}} = 16.41$ mM, $[\text{BTB}]_{\text{prec}} = 1.14$ M, $\Delta T = 6$ °C/min; C) $[\text{Pd}^{2+}]_{\text{prec}} = 16.41$ mM, $[\text{BTB}]_{\text{prec}} = 0.57$ M, $\Delta T = 3$ °C/min; D) $[\text{Pd}^{2+}]_{\text{prec}} = 16.41$ mM, $[\text{BTB}]_{\text{prec}} = 0.57$ M, $\Delta T = 6$ °C/min.

Figure 3.23 A shows the measured SAXS-curves at 90 °C with a heating rate $\Delta T = 3$ °C/min for a Pd^{2+} -precursor concentration $[\text{Pd}^{2+}]_{\text{prec}} = 16.41$ mM and a BTB-precursor concentration of $[\text{BTB}]_{\text{prec}} = 1.14$ M, which after mixing results in concentrations of $[\text{Pd}^{2+}]_0 = 13.67$ mM and $[\text{BTB}]_0 = 190$ mM during the initiation of the reaction.

Over the reaction time, the measured scattering curves show a Guinier plateau at low scattering vector q , which develops into a q^{-4} -Porod decay at $q > 1$ nm⁻¹, followed by a shoulder at $q \sim 2$ nm⁻¹ corresponding to the damped formfactor oscillation of the nanoparticles.

The scattering intensity increases significantly with reaction time indicating the growth phase of the nanoparticles. Also the formfactor oscillations shift to lower q by time, which is a sign of an increase in the nanoparticle radius during the growth phase.

The Pd-nanoparticle growth with a higher heating rate ($\Delta T = 6 \text{ }^\circ\text{C}/\text{min}$) was measured for the same precursor concentrations in figure 3.23 B. The measured scattering curves show the same features as for the measurement with a heating rate $\Delta T = 3 \text{ }^\circ\text{C}/\text{min}$ (3.23 A), but the particle growth occurs a bit faster, as the early growth phase with the characteristic increase of the scattering intensity is already finished ca. 5 min earlier (after 15 min).

To acquire information on the concentration dependence, some experiments for more diluted BTB-precursor solutions with $[\text{BTB}]_{\text{prec}} = 0.57 \text{ M}$ and a constant $\text{Pd}(\text{acac})_2$ -precursor concentration at $[\text{Pd}^{2+}]_{\text{prec}} = 16.41 \text{ mM}$ were performed. Figure 3.23 C and figure 3.23 D represent these measurements.

Figure 3.23 C shows the SAXS-curves for a reaction with a heating rate $\Delta T = 3 \text{ }^\circ\text{C}/\text{min}$, a Pd^{2+} -precursor concentration $[\text{Pd}^{2+}]_{\text{prec}} = 16.41 \text{ mM}$ and a BTB-precursor concentration $[\text{BTB}]_{\text{prec}} = 0.57 \text{ M}$, which after mixing results in concentrations of $[\text{Pd}^{2+}]_0 = 13.67 \text{ mM}$ and $[\text{BTB}]_0 = 95 \text{ mM}$ during the initiation of the synthesis.

These scattering curves exhibit the same properties, but in direct comparison with the higher concentration (3.23 A) it is noticeable that the particle growth is faster in case of the nanoparticle reaction with lower BTB-precursor concentration.

The same observation is made comparing the two measurements with the higher heating rate (figure 3.23 B and figure 3.23 D). It seems that a higher BTB-concentration lead to a kind of blockage of the reactive side of the molecules, that is why less BTB-concentration implicates a faster particle growth.

To obtain information on the temperature dependence, the same experiments were performed at a reaction temperature of $70 \text{ }^\circ\text{C}$. The measured SAXS-curves of these experiments are summarized in figure 3.24. Also in these experiments, the $\text{Pd}(\text{acac})_2$ -precursor concentration was kept constant and only the BTB-precursor concentration as well as the heating rate were varied.

The features of the scattering curves are similar to those in figure 3.23.

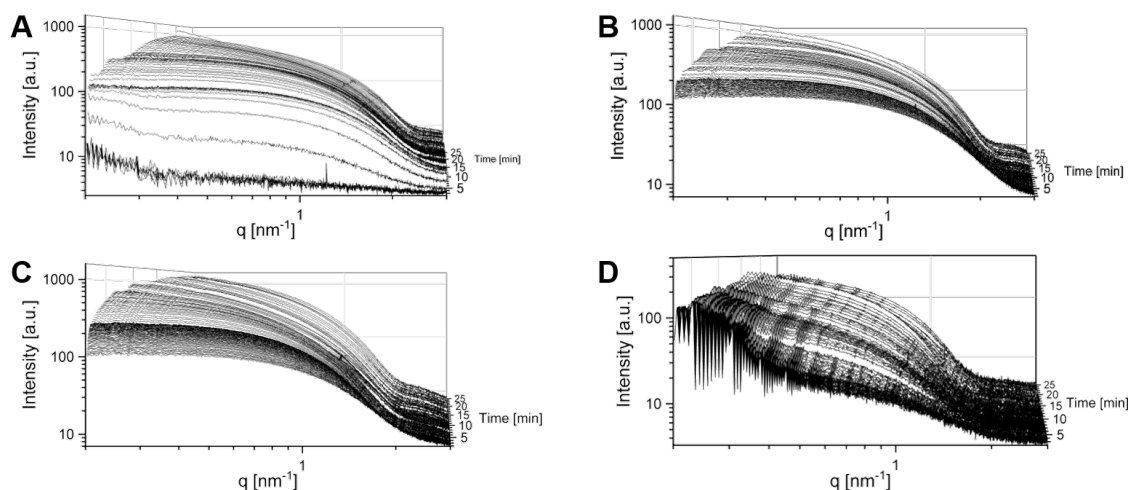


Figure 3.24: Stack-plots of selected measurement data of the SAXS-curves recorded in situ during the formation of the Pd nanoparticles at a temperature of 70 °C: A) $[\text{Pd}^{2+}]_{\text{prec}} = 16.41 \text{ mM}$, $[\text{BTB}]_{\text{prec}} = 1.14 \text{ M}$, $\Delta T = 3 \text{ }^\circ\text{C/min}$; B) $[\text{Pd}^{2+}]_{\text{prec}} = 16.41 \text{ mM}$, $[\text{BTB}]_{\text{prec}} = 1.14 \text{ M}$, $\Delta T = 6 \text{ }^\circ\text{C/min}$; C) $[\text{Pd}^{2+}]_{\text{prec}} = 16.41 \text{ mM}$, $[\text{BTB}]_{\text{prec}} = 0.57 \text{ M}$, $\Delta T = 3 \text{ }^\circ\text{C/min}$; D) $[\text{Pd}^{2+}]_{\text{prec}} = 16.41 \text{ mM}$, $[\text{BTB}]_{\text{prec}} = 0.57 \text{ M}$, $\Delta T = 6 \text{ }^\circ\text{C/min}$.

Figure 3.24 A shows the measured SAXS-curves at 70 °C with a heating rate $\Delta T = 3 \text{ }^\circ\text{C/min}$ for a Pd^{2+} -precursor concentration $[\text{Pd}^{2+}]_{\text{prec}} = 16.41 \text{ mM}$ and a BTB-precursor concentration $[\text{BTB}]_{\text{prec}} = 1.14 \text{ M}$. A Guinier plateau at low scattering vector q is shown by the measured scattering curves, which develops into a q^{-4} -Parod decay at $q > 1 \text{ nm}^{-1}$, followed by a shoulder at $q \sim 2 \text{ nm}^{-1}$ corresponding to the dulled formfactor oscillation of the Pd nanoparticles. The scattering intensity increases with reaction time, which indicates the growth phase of these nanoparticles. The formfactor oscillation shifts to lower q values by time. This is a sign of an increase in the nanoparticle size during the growth phase.

The nanoparticle growth with a higher heating rate $\Delta T = 6 \text{ }^\circ\text{C/min}$ was measured for the same precursor concentrations and is shown in figure 3.24 B. The measured SAXS-curves show the same features as for the measurement with a lower heating rate (3.24 A), but the particle growth happened faster, as the early growth phase clarifies.

To get also information on the concentration dependence, some experiments for a more diluted BTB-precursor concentration with $[\text{BTB}]_{\text{prec}} = 0.57 \text{ M}$ have been executed. The Pd^{2+} -precursor concentration for these experiments was kept constant at $[\text{Pd}^{2+}]_{\text{prec}} = 16.41 \text{ mM}$. Figure 3.24 C and figure 3.24 D represent these measured scattering curves.

Figure 3.24 C display the SAXS-curves for the reaction with a heating rate $\Delta T = 3 \text{ }^\circ\text{C/min}$.

The scattering curves exhibit the same properties, but in the direct comparison with the higher BTB-concentration (3.24 A) it is noticeable that the particle growth occurs in this case faster. The same observation is made comparing the results of the two measurements with the higher heating rate $\Delta T = 6 \text{ }^\circ\text{C}/\text{min}$ (figure 3.24 B and figure 3.24 D).

It seems also at a reaction temperature of $70 \text{ }^\circ\text{C}$ that a higher BTB-concentration lead to a kind of barrier to the reactive side of the molecules. That is the reason why less BTB concentration implicates a faster growth of the nanoparticles.

In summary, it can be said that in this series of measurements is also has been observed that the BTB-precursor concentration has an influence on the rate of particle growth. Likewise, the heating rate has almost no influence on particle growth. With lower BTB-concentration, the formfactor oscillation shifting to lower q values is faster and it follows that the Pd nanoparticles grow faster.

The fact that the reaction temperature has a large influence on particle growth becomes clear by comparing the measurements at different temperatures and the same reaction conditions, for example comparing figure 3.23 A with figure 3.24 A or figure 3.23 B with figure 3.24 B.

In the following, the SAXS-curves will be analyzed quantitatively. To further describe the data analysis, selected SAXS-curves representative for the early, middle and late stages of Pd nanoparticle growth are shown in figure 3.25 for the case of a Pd^{2+} -precursor concentration $[\text{Pd}^{2+}]_{\text{prec}} = 16.41 \text{ mM}$, a BTB-precursor concentration $[\text{BTB}]_{\text{prec}} = 0.57 \text{ M}$, a heating rate $\Delta T = 3 \text{ }^\circ\text{C}/\text{min}$ and a synthesis temperature of $90 \text{ }^\circ\text{C}$, as shown in figure 3.23 C.

The scattering curves are fitted to an analytically expression of the formfactor of poly-disperse homogeneous spheres, like it was described in chapter 3.1.3. The fitted curves, indicated by the red dotted lines, show a very good agreement with the experimentally determined SAXS-curves.

From the fits the scattered intensity $I(0)$, the mean radius of the particles \bar{R} and the relative polydispersity σ were obtained. The polydispersity for all scattering curves is in the range of 0.16 - 0.23.

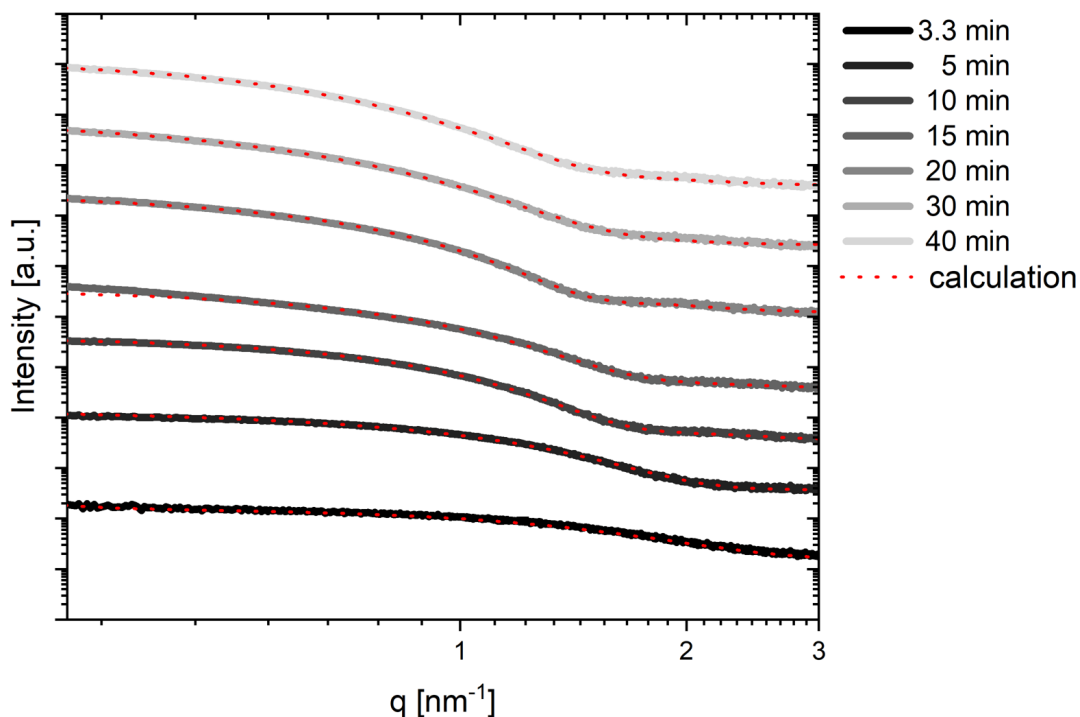


Figure 3.25: Selected SAXS-curves of the Pd-nanoparticle formation at 90 °C with $[\text{Pd}^{2+}]_{\text{prec}} = 16.41 \text{ mM}$, $[\text{BTB}]_{\text{prec}} = 0.57 \text{ M}$ and $\Delta T = 3 \text{ }^\circ\text{C}/\text{min}$ at different times. The red dotted lines indicate the fits to the measured scattering curves.

Figure 3.26 shows two comparisons of the particle radii as a function of time. The black and red dotted data indicate the syntheses at 90 °C, the green and blue dotted data the syntheses at 70 °C.

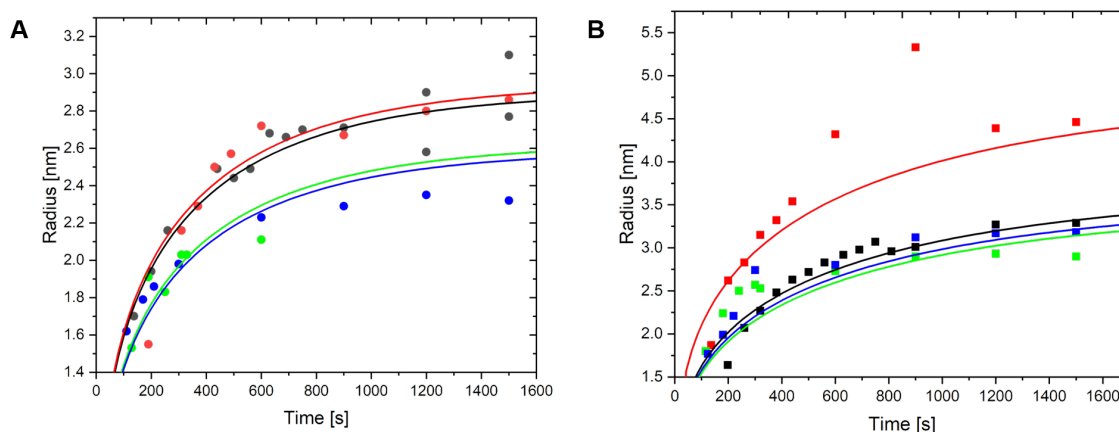


Figure 3.26: Time evolution of the average Pd-nanoparticle radius determined from the fitted SAXS-curves for different temperatures and heating rates with a $[\text{BTB}]_{\text{prec}} = 1.14 \text{ M}$ (A) and with a $[\text{BTB}]_{\text{prec}} = 0.57 \text{ M}$ (B). The black and green data indicate the syntheses with a heating rate $\Delta T = 3 \text{ }^\circ\text{C}/\text{min}$, the red and blue data the syntheses with a heating rate $\Delta T = 6 \text{ }^\circ\text{C}/\text{min}$. The black and red dotted data indicate the syntheses at 90 °C, the green and blue dotted data the syntheses at 70 °C. The solid lines indicate the calculation to the determined data.

Figure 3.26 A shows the temperature comparison of the Pd-nanoparticle syntheses with a BTB-precursor concentration of $[BTB]_{prec} = 1.14M$. It is noticeable that the influence of the heating rate ΔT (black and green data: $\Delta T = 3\text{ }^{\circ}C/min$; red and blue data: $\Delta T = 6\text{ }^{\circ}C/min$) does not have a big influence on the growth rate of the Pd nanoparticles as comparatively the synthesis temperature.

The same finding can be obtained by comparing the nanoparticle syntheses with the lower BTB-precursor concentration $[BTB]_{prec} = 0.57\text{ M}$ in figure 3.26 B. By increasing the reaction temperature, the molecules moves faster, so that the number of effective collisions between the molecules increases and results in a faster reaction. The change in the end temperature has therefore a greater influence in particle growth than the speed to achieve this temperature.

A comparison within the respective synthesis temperature with respect to the BTB-precursor concentration is shown in figure 3.27.

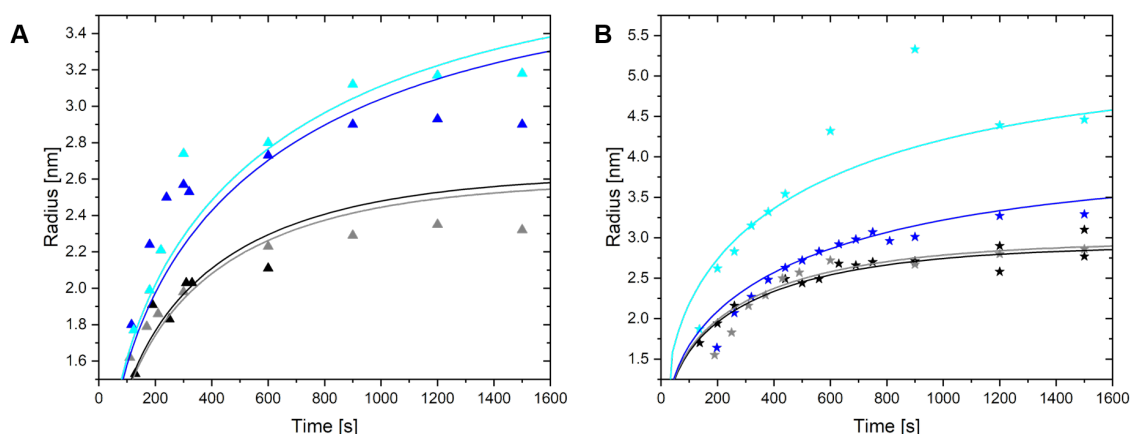


Figure 3.27: Time evolution of the average Pd-nanoparticle radius determined from the fitted SAXS-curves for different BTB-concentrations and heating rates at a synthesis temperature of 70 °C (A) and 90 °C (B). The black and dark blue data indicate the syntheses with a heating rate $\Delta T = 3\text{ }^{\circ}C/min$, the grey and light blue data the syntheses with a heating rate $\Delta T = 6\text{ }^{\circ}C/min$. The black and grey dotted data indicate the syntheses with a high BTB-concentration $[BTB]_{prec} = 1.14\text{ M}$, the dark and light blue dotted data the syntheses with a low BTB-concentration $[BTB]_{prec} = 0.57\text{ M}$. The solid lines indicate the calculation to the determined data.

The black and grey dotted data indicate the syntheses with the higher BTB-precursor concentration $[BTB]_{prec} = 1.14\text{ M}$, the dark and light blue dotted data the syntheses with the lower BTB-precursor concentration $[BTB]_{prec} = 0.57\text{ M}$.

Similarly, on the one hand the black and dark blue data describe the nanoparticle formation with a heating rate $\Delta T = 3\text{ }^{\circ}C/min$ and on the other hand the grey and light blue data represent the syntheses with a heating rate $\Delta T = 6\text{ }^{\circ}C/min$.

Figure 3.27 A shows the time evolution of the average Pd-nanoparticle radius of all synthesis at a temperature of 70 °C and figure 3.27 B for all synthesis at a temperature of 90 °C. In both cases it can be seen that the heating rate ΔT has almost no influence on particle growth, but the BTB-precursor concentration. For both temperatures, the nanoparticles grow faster at the lower BTB-precursor concentration.

This contradicts any expectation that a reaction will be faster by increasing the concentration, because an increased concentration contains more reactant molecules that can react with each other. In this nanoparticle synthesis the reactive side of the molecules initially appears to be blocked at a high BTB-concentration, so that the molecules can collide with each other but can not react with each other.

By the decreasing of the BTB-concentration more efficient collisions between the molecules occur. That is the reason why the reaction is faster in this case. The BTB-molecules can react with the carboxylic functional group^[92] of the Pd(acac)₂-molecules more unhindered.

3.2.4 Nucleation and growth model

The growth curves were quantitatively analyzed by a nucleation and growth model which was recently successfully applied to the growth of Au-nanoparticles.^[15] For this Pd nanoparticles the following greatly simplified chemical reaction was considered:



The kinetic model is formulated in terms of the time dependence of the concentrations of the precursors $[\text{Pd}^{2+}]$ and $[\text{BTB}]$, of free solvated Pd-units $[\text{Pd}]$, of Pd-units incorporated into nanoparticles by nucleation $[\text{Pd}_N]$ or by growth onto earlier formed nanoparticles J $[\text{Pd}_J]$ as well as in terms of the particle concentrations $[P_J]$ during the nucleation and growth period.

It corresponds to a set of coupled first order differential equations with respect to the ionic components

$$\begin{aligned} \frac{d[\text{Pd}^{2+}]}{dt} &= -k_1 [\text{Pd}^{2+}] [\text{BTB}] \\ \frac{d[\text{BTB}]}{dt} &= -k_1 [\text{Pd}^{2+}] [\text{BTB}] \\ \frac{d[\text{Pd}]}{dt} &= k_1 [\text{Pd}^{2+}] [\text{BTB}] - \beta \frac{V}{\nu_0} \exp\left[-\frac{\Delta G_c}{k T}\right] - \int_0^t 4\pi R_J D N_A [\text{Pd}] \frac{\left(1 - \frac{[\text{Pd}]_{\text{sat}}}{[\text{Pd}]} \exp\left[\frac{R_{\text{cap}}}{R_J}\right]\right)}{\left(1 + \frac{D}{R_J k_{gr}}\right)} h(t_j) dt_j \\ \frac{d[\text{Pd}_N]}{dt} &= \beta \frac{V}{\nu_0} \exp\left[-\frac{G_c}{k T}\right] \\ \frac{d[\text{Pd}_{PJ}]}{dt} &= 4 R_J D N_A [P_J] [\text{Pd}] \frac{\left(1 - \frac{[\text{Pd}]_{\text{sat}}}{[\text{Pd}]} \exp\left[\frac{R_{\text{cap}}}{R_J}\right]\right)}{\left(1 + \frac{D}{R_J k_{gr}}\right)}, J = 1, \dots, N \\ \left. \frac{d[P_J]}{dt} \right|_{t=t_j} &= \beta \exp\left[-\frac{\Delta G_c}{k T}\right] \delta [t - t_j] = h(t_j) \end{aligned} \quad (3.9)$$

where $\delta [t - t_j]$ is the delta function used to describe the concentration of a new nucleated species $[P_J]$, which is determined by the amount of $[\text{Pd}_N]$ produced at $t = t_j$.

k_1 is the rate constant of the chemical reaction, k_{gr} the rate constant of the growth reaction and V the volume of the spherical particle related to the particle radius by $V = \frac{4\pi R^3}{3}$. $\nu_0 = \frac{M}{\rho N_A} \approx 1.47 \cdot 10^{-29} m^3$ is the molar volume of a Pd-unit, calculated from its molar mass M , the Pd bulk density ρ and Avogadro's constant N_A .

$\beta = \frac{4 k_B T}{9 \eta \nu_0}$ is the rate constant of the nucleation reaction, calculated from Boltzmann's constant k_B and the solvent viscosity η . $D = \frac{k_B T}{6 \pi \eta R}$ is the diffusion constant of the Pd-units, γ the interfacial tension of the ZnO nanoparticles and $[Pd]_{sat}$ the saturation concentration of Pd.

The nucleation free enthalpy is given by

$$\Delta G_c(t) = \frac{16\pi\gamma^3\nu_0^2}{3(k_B T)^2 (\ln S(t))^2} \quad (3.10)$$

where $S = \frac{[Pd]}{[Pd]_{sat}}$ is the supersaturation.

A priori known parameters are the molar mass M of Pd ($M = 106.42$ g/mol), the bulk density ρ of Pd (12 g/mol) and the solvent viscosity η (30 mPas).

Unknown values are the rate constant k_1 of the chemical reaction, the growth rate constant k_{gr} , the interfacial tension γ of the Pd nanoparticles, and the saturation concentration $[Pd]_{sat}$ of Pd, whose values are fitted to the experimental data in figure 3.28.

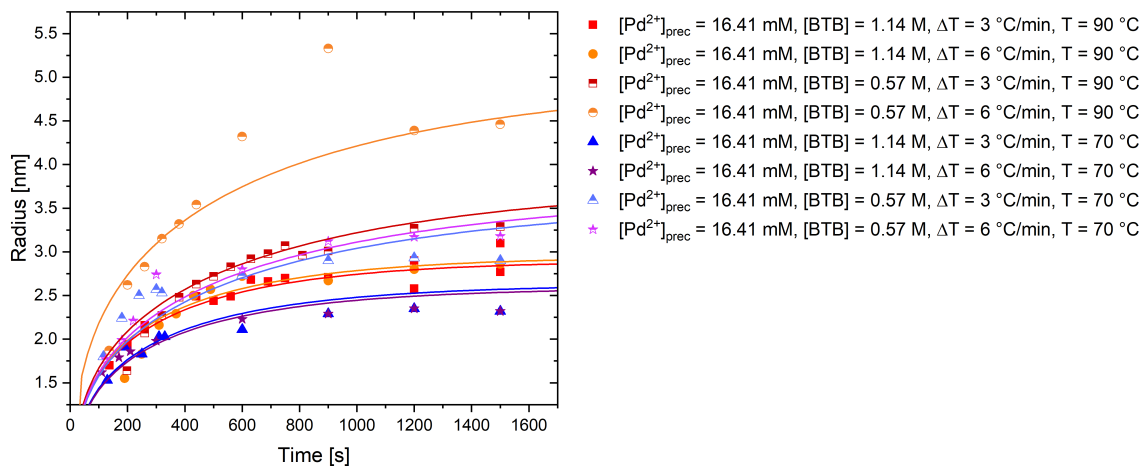


Figure 3.28: Time evolution of the average Pd-nanoparticle radius determined from the fitted SAXS-curves for different concentrations, heating rates and syntheses temperatures

Solving this set of coupled differential equations yields the concentrations $[P_j](t)$ and radii $R_j(t)$ of all particles J that have been formed during the nucleation process, from which the size distribution $h(R,t)$, the mean radius \bar{R} and the relative standard deviation $\sigma_R(t)$ can be obtained and compared to the experimental data. Details of the calculations are given by X. L. Chen.^[15]

Table 3.5 shows the values of k_1 , k_{gr} , γ and $[Pd]_{sat}$ for which the best agreement with the measured growth case was obtained.

Table 3.5: Values for k_1 , k_{gr} , γ and $[Pd]_{sat}$ for which the best fit to the experimental data was obtained

Temperature [°C]	$[Pd]_0$ [mM]	$[BTB]_0$ [mM]	ΔT [°C/min]	k_1 [m ³ /Ms]	k_{gr} [m/s]	γ [mN/m]	$[Pd]_{sat}$ [mM]
90	13.70	190	3	$1.0 \cdot 10^{-5}$	$5.8 \cdot 10^{-5}$	205	$2.0 \cdot 10^{-6}$
90	13.70	190	6	$1.0 \cdot 10^{-5}$	$6.0 \cdot 10^{-5}$	205	$2.0 \cdot 10^{-6}$
90	13.70	95	3	$1.0 \cdot 10^{-5}$	$5.1 \cdot 10^{-5}$	205	$2.0 \cdot 10^{-6}$
90	13.70	95	6	$1.0 \cdot 10^{-5}$	$8.5 \cdot 10^{-5}$	205	$2.0 \cdot 10^{-6}$
70	13.70	190	3	$1.0 \cdot 10^{-5}$	$6.0 \cdot 10^{-5}$	205	$1.0 \cdot 10^{-6}$
70	13.70	190	6	$1.0 \cdot 10^{-5}$	$6.0 \cdot 10^{-5}$	205	$1.0 \cdot 10^{-6}$
70	13.70	95	3	$3.0 \cdot 10^{-5}$	$1.3 \cdot 10^{-4}$	205	$1.0 \cdot 10^{-6}$
70	13.70	95	6	$1.0 \cdot 10^{-5}$	$7.5 \cdot 10^{-5}$	205	$1.0 \cdot 10^{-6}$

The surface tension Pd/OAm was the same for all measurements with a value of 205 mN/m. The value for the saturation concentration is temperature depending. The value of $[Pd]_{sat} = 2 \cdot 10^{-6}$ mol/L is the same for all measurements at 90 °C, the value of $[Pd]_{sat} = 1 \cdot 10^{-6}$ mol/L is the same for all synthesis at 70 °C. The precursor reaction rates k_1 are concentration independent and in the order of $k_1 \sim 1.0 \cdot 10^{-5}$ m³/mols.

As outlined by X. L. Chen^[15] initiating the nucleation process, the time at which a critical saturation of $S \sim 100$ is reached, can be estimated as

$$\tau_{nuc} = \frac{S[Pd]_{sat}}{k_1 [Pd^{2+}]_0 ([Pd^{2+}]_0 - S [Pd]_{sat})} \quad (3.11)$$

which is in the order of $\tau_{nuc} \sim 1$ s for the measurements at 90 °C and $\tau_{nuc} \sim 0.5$ s for the measurements at 70 °C. Similarly, the radius of the critical nucleus can be calculated as

$$R = \frac{2 \gamma \nu_0}{k_B T \ln S} \quad (3.12)$$

which is $1.36 \cdot 10^{-7}$ m for the syntheses at 90 °C and $1.33 \cdot 10^{-7}$ m for the syntheses at 70 °C.

The measured growth rates k_{gr} decrease slightly with increasing concentration as well as with increasing temperature and are in the order of $\sim 7.24 \cdot 10^{-5}$ m/s. These are an order of magnitude faster compared to values measured for Au-nanoparticles in toluene, which as $k_{gr} \sim 1 \cdot 10^{-6}$ m/s, likely because the activation process for growth is lower across the Pd(acac)₂/solvent stabilization layer.

From the temperature dependence of the rate constants the activation energy for both reactions were estimated to be ~ 21 kJ/mol, which is a reasonable value, somewhat larger than determined for Au-nanoparticle formation.

The investigation of the nucleation and growth kinetics of palladium nanoparticles in situ experiments were performed at a synchrotron, which made an observation of the growth in millisecond time steps possible. It can be said that nucleation and growth for these palladium nanoparticles follow the classical model.

3.2.5 Transmission electron microscopy

To characterize the Pd nanoparticles after the synthesis, the original solutions were analyzed by TEM. Figure 3.29 shows TEM-images of selected Pd nanoparticles syntheses of this work.

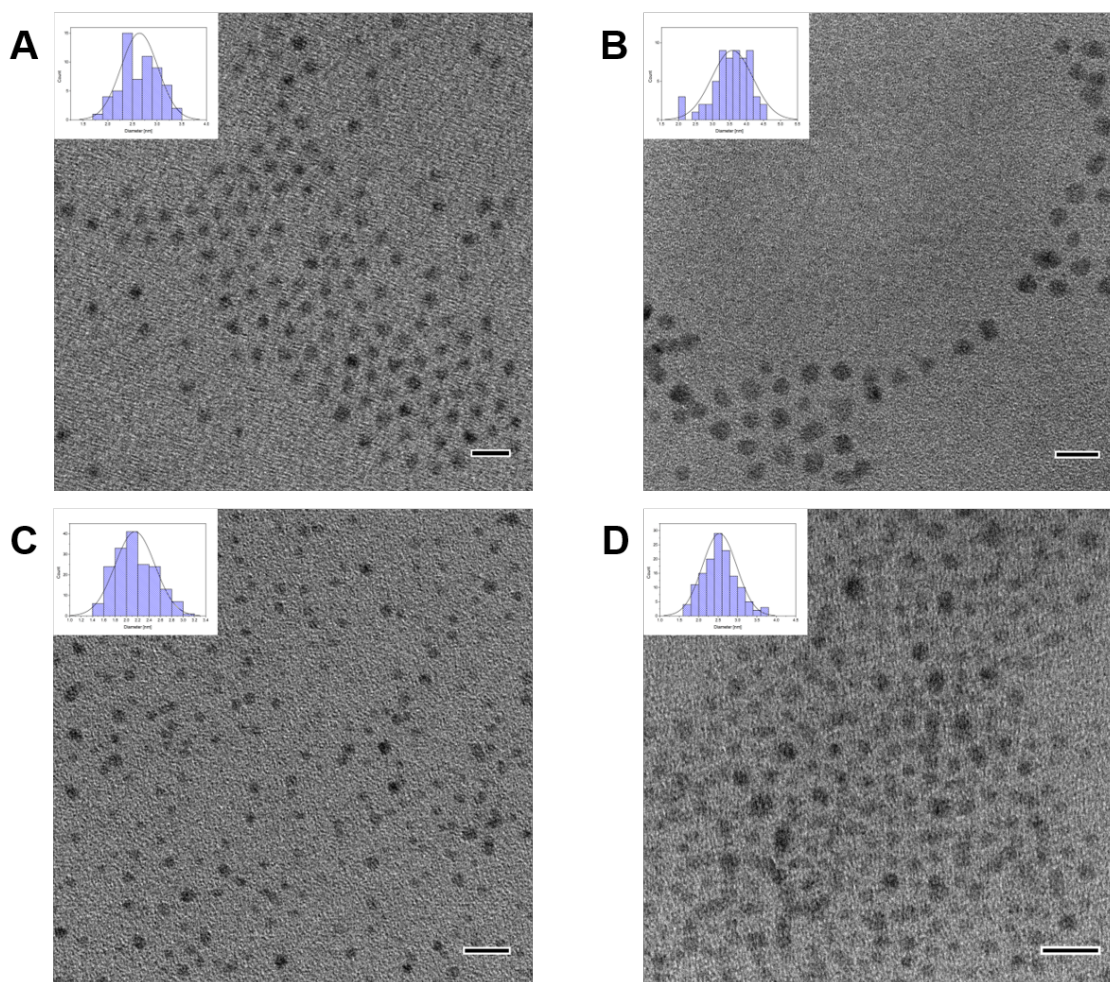


Figure 3.29: TEM-images of Pd nanoparticles with an average particle diameter between 2.0 nm and 3.5 nm:

A) $[\text{Pd}^{2+}]_{\text{prec}} = 16.41 \text{ mM}$, $[\text{BTB}]_{\text{prec}} = 1.14 \text{ M}$, $T = 90 \text{ }^\circ\text{C}$; $\Delta T = 3 \text{ }^\circ\text{C}/\text{min}$;

B) $[\text{Pd}^{2+}]_{\text{prec}} = 16.41 \text{ mM}$, $[\text{BTB}]_{\text{prec}} = 0.57 \text{ M}$, $T = 90 \text{ }^\circ\text{C}$; $\Delta T = 3 \text{ }^\circ\text{C}/\text{min}$;

C) $[\text{Pd}^{2+}]_{\text{prec}} = 16.41 \text{ mM}$, $[\text{BTB}]_{\text{prec}} = 1.14 \text{ M}$, $T = 70 \text{ }^\circ\text{C}$; $\Delta T = 3 \text{ }^\circ\text{C}/\text{min}$;

D) $[\text{Pd}^{2+}]_{\text{prec}} = 16.41 \text{ mM}$, $[\text{BTB}]_{\text{prec}} = 1.14 \text{ M}$, $T = 90 \text{ }^\circ\text{C}$; $\Delta T = 6 \text{ }^\circ\text{C}/\text{min}$;

The particles with a average diameter of $2.6 \pm 0.4 \text{ nm}$, synthesized with a $[\text{BTB}]_{\text{prec}}$ -concentration of 1.14 M, a reaction temperature $T = 90 \text{ }^\circ\text{C}$ and a heating rate $\Delta T = 3 \text{ }^\circ\text{C}/\text{min}$ are shown in figure 3.29 A.

For a comparison with the lower $[\text{BTB}]_{\text{prec}}$ -concentration = 0.57 M, figure 3.29 B shows particles with an average size of $3.6 \pm 0.6 \text{ nm}$. The reaction temperature and heating

rate, in this case, are the same as for the synthesis of the Pd nanoparticles of figure 3.29 A.

To illustrate the influence of the reaction temperature, figure 3.29 C shows the particles that have been synthesized at a reaction temperature of 70 °C. The $[BTB]_{prec}$ -concentration and heating rate ΔT are the same as for the particle synthesis in figure 3.29 A. The average diameter of the Pd nanoparticles for this case is 2.2 ± 0.4 nm.

The heating rate ΔT is also a parameter that has been varied in some Pd nanoparticle syntheses during this work. Figure 3.29 D shows particles with an average size of 2.5 ± 0.4 nm. The $[BTB]_{prec}$ -concentration in this synthesis was 1.14 M, the reaction temperature 90 °C and the heating rate 6 °C/min.

In summary, for the Pd nanoparticle syntheses, it also can be shown from the TEM images that the average particle size after a finished synthesis increases slightly with higher reaction temperature. It was noted that the diameter of the nanoparticles as determined by TEM after synthesis deviates a little from the values measured during the growth process by SAXS.

3.3 Development of microfluidic chips for studying biological and medical processes

In the period from October 2014 to July 2017 there was a collaborative work between the group of Prof. Dr. S. Förster (Physical Chemistry, University of Bayreuth) and the group of Dr. M. Bender (Experimental Biomedicine at the University Hospital Würzburg) on microfluidic bioreactors and stenosis experiments. For the microfluidic investigation of the thrombus formation the cooperation was expanded with Prof. Dr. S. Gekle (Theoretical Physics, University of Bayreuth).

The focus of my work was the design development and fabrication of the microfluidic chips for the stenosis experiments and the microfluidic bioreactors. The experiments, which were partly done together, were mainly evaluated concerning biological and medical aspects by Ruth Kranz (Experimental Biomedicine at the University Hospital Würzburg). She will also include a chapter about this stenosis experiments in her dissertation. Prof. Gekle created corresponding simulations to the data of our experiments.

The following pages give an overview about the steps of the design development of the respective microfluidic chips and show some results of the experiments carried out for this purpose.

3.3.1 Design development and producing of microfluidic chips for performing and monitoring thrombus formation

3.3.1.1 Description of the experiments

The aim of this cooperative work was to investigate the thrombus formation, the thrombus fanning out and cutting off as well as the rolling of platelets. For this at first, as described in chapter 3.3, microfluidic chips with a channel tapering, to model stenosis, were produced. In a standard stenosis-experiment, the microfluidic channels were infused at the beginning with a solution of antibodies (figure 3.30 A).

This step is important to slow down the platelets later during the actual experiment. Subsequent, the channels were rinsed with bovine serum albumin (BSA) to saturate unspecific bonds.

In the second step, the channels were rinsed with mouse plasma solution (figure 3.30 B). This plasma contains von Willebrand Factor (VWF), which is an important protein for platelet adhesion in hemostasis.

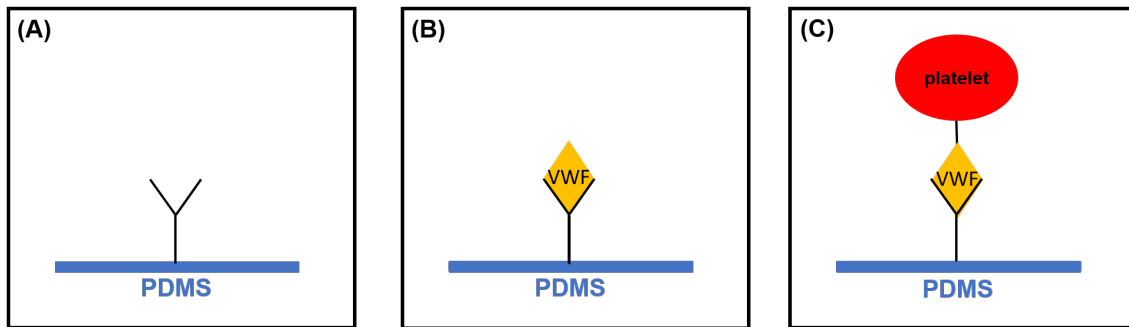


Figure 3.30: Schematic illustration of the experimental procedure to investigate thrombus formation

In the last step (figure 3.30 C), the actual experiment can be done. For this, whole blood from mice or mice ubiquitously expressing GFP was infused through the respective channels at different flow rates and investigated using a light microscope or fluorescence light microscope. Some experiments were recorded with a high-speed camera.

To achieve the best possible results, the channel designs were changed and optimized several times. The design development will be discussed in more detail below. In order to illustrate the individual steps better, several results are shown in this thesis too, but their medical and biological analysis is not part of this work.

3.3.1.2 Discussion of the results

Figure 3.31 shows an example of one of the first channel designs for these experiments. The channel width and height were each $30\ \mu\text{m}$. There were two channel inputs and one output. The tapers of the particular channels varied between 70 % and 80 %.

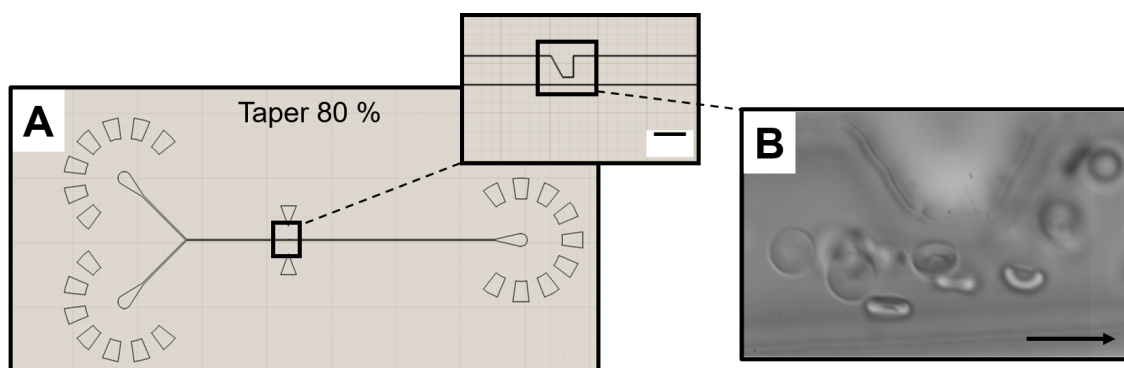


Figure 3.31: Exemplary sketch of one of the first channel designs (scale bar: $30\ \mu\text{m}$) for the stenosis experiments (A) and a corresponding screenshot of a video of an experiment, where mice blood was infused through the channel with a flow rate of $50\ \mu\text{L/h}$ (B). The arrow indicates the direction of the flow.

It could be determined that the tapers of the channels were too minor, which means that it will probably be impossible to induce a thrombus formation with a size of $2\ \mu\text{m}$ in a channel with a gap size of at least $6\ \mu\text{m}$. This can be clearly seen in figure 3.31 B. The platelets flow unhindered through the constriction in the microfluidic channel.

In order to improve the results in this channel design, the microfluidic chips were coated by the method described above.

In figure 3.32 some screenshots of a video of an experiment, where GFP positive blood cells were infused with a flow rate of $15\ \mu\text{L/h}$ through the channel, are summarized. It is shown that the coating process had a positive effect on thrombus formation. In the same way it exemplifies the rolling motion of the platelets within the thrombus and the final constriction process.

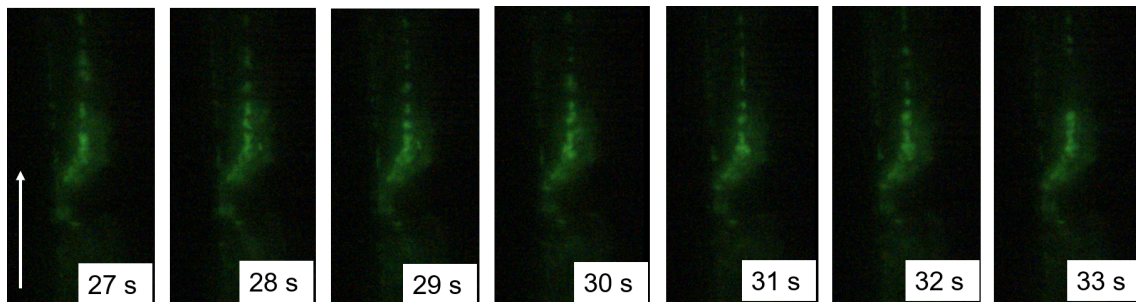


Figure 3.32: Screenshots of a video of an experiment where GFP positive blood cells were infused with a flow rate of $15\ \mu\text{L/h}$ through the microfluidic chip. The arrow indicates the direction of the flow.

Based on the previous experimental results and the resulting findings, the tapers of the microfluidic channels were increased in the next step of design development. The smaller gap size should simplify and support thrombus formation.

Figure 3.33 shows a design example of a microfluidic channel with a larger taper. There were still two channel inputs and one output, as well as the channel width and height was each $30\ \mu\text{m}$. The tapers of the particular channels varied between 80 % and 90 %.

Due to the smaller gap width and the channel coating it was always possible to investigate thrombus formation from now on.

But there was an increasing problem that the channels were plugged and thereby pressurized, causing the destroying of the bonding between the glass slide and the PDMS as well as the leaking of microfluidic chips.

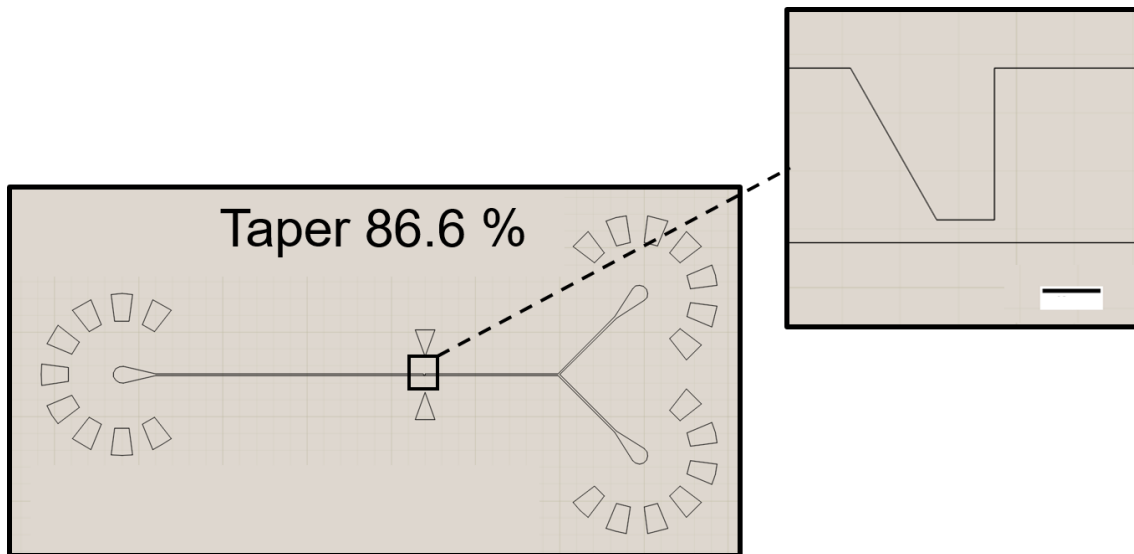


Figure 3.33: Exemplary sketch of channel designs (Design V3) with larger tapers (scale bar: 10 μm)

This is demonstrated in figure 3.34.

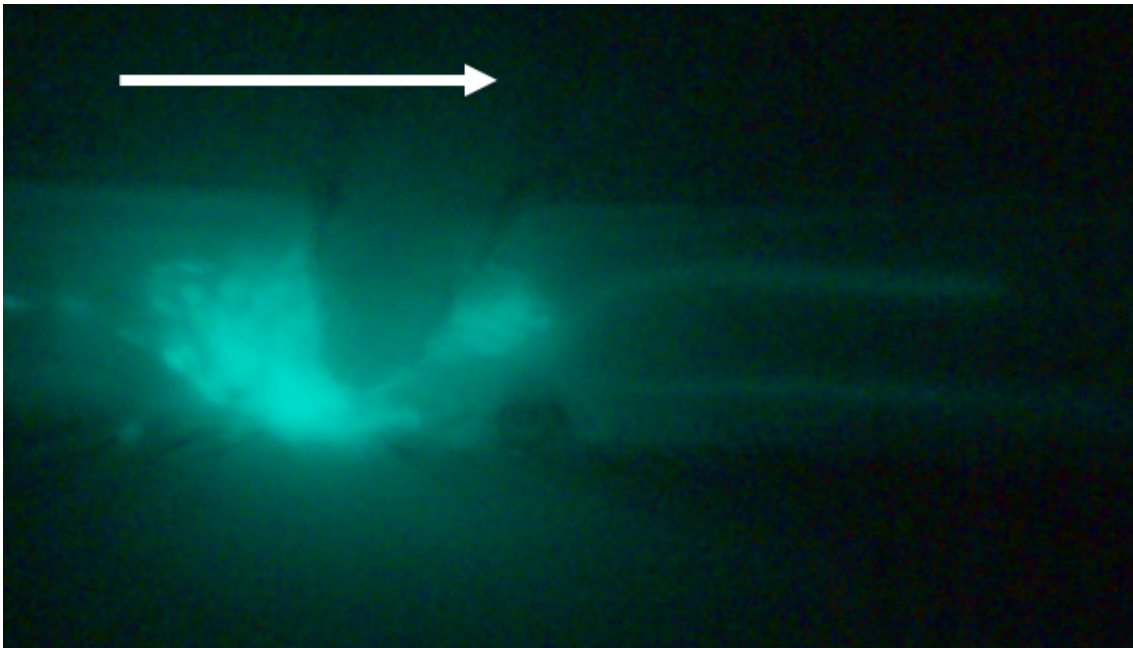


Figure 3.34: A screenshot of a video of an experiment where fluorescent mouse blood was infused with a flow rate of 15 $\mu\text{L/h}$ through the microfluidic chip shows a blockage in the channel and, as a result of this, the PDMS under pressure. The arrow indicates the direction of the flow.

It shows a blockage in the microfluidic channel, which increased the pressure in the channel so much that the bonding between PDMS and the glass slide was destroyed. To handle this, new channel structures with expanded channel width were designed.

In addition, the number of channel inputs was reduced to one, as this simplified the performance of the experiment.

Before that, a channel input had to be closed after the channel coating, as it was no longer needed. At this point in the microfluidic chip, disturbing air bubbles accumulated during the experiment. This led in part to an increased pressure in the microfluidic channel and was the reason for its leakage. Due to this these microfluidic chips could not be used anymore.

A summary of all new designs of the microfluidic channels in this step of design development is given in figure 3.35. The channel heights varied between 30 μm and 60 μm per channel, the channel tapers, depending on the channel width, between 75 % and 90 %. The wider channels have the advantage that from now on higher flow rates could

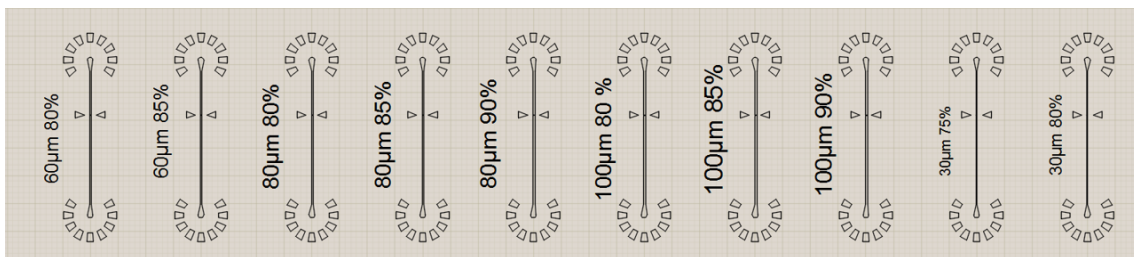


Figure 3.35: Sketch of channel designs with larger geometry and channel tapers (Design V4).

be used. Figure 3.36 shows screenshots of a video sequence of an experiment where mouse blood was infused with a flow rate of 200 $\mu\text{L}/\text{h}$ through a microfluidic chip with a channel taper of 80 %. A thrombus has formed here before the beginning of the video recording. These images display clearly the thrombus fanning out, the rolling of platelets and also the thrombus cutting off.

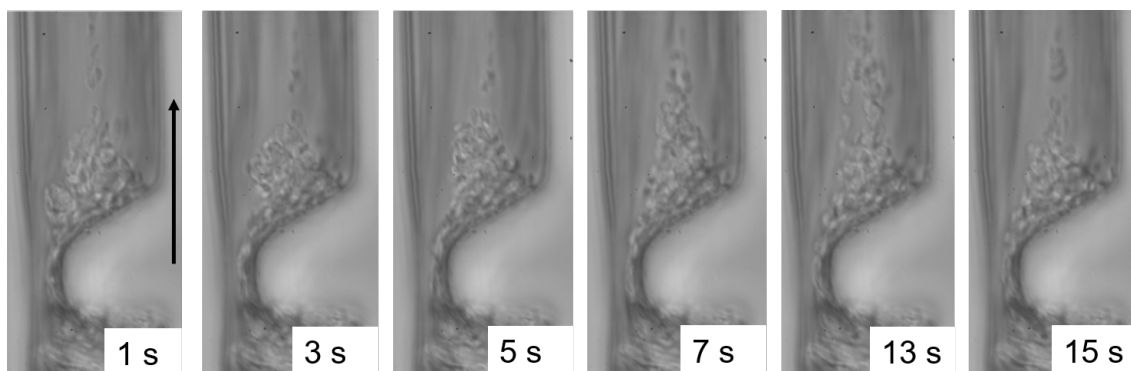


Figure 3.36: Screenshots of a high-speed camera video of an experiment where mouse blood was infused with a flow rate of 200 $\mu\text{L}/\text{h}$ through a microfluidic chip with a channel taper of 80 %. The arrow indicates the direction of the flow.

In a next step of design development, the angle of the tapering was changed from 34° to 17° and 55°. These new channel structures are displayed in figure 3.37.

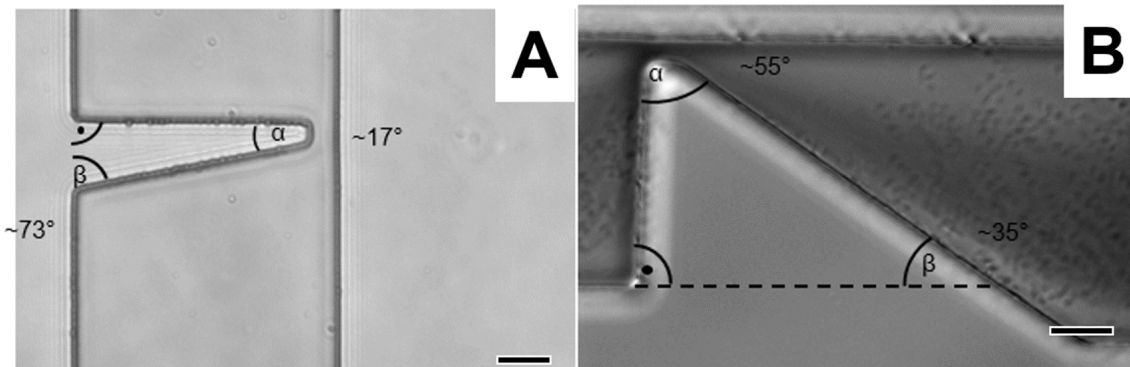


Figure 3.37: Comparison of two new channel designs with an angle at the channel tapering of 17° (A) and 55° (B), scale bars: 20 μm . This graphic was provided by Ruth Kranz.

Based on achieving the best results with microfluidic channels with a width of 100 μm and 80 μm as well as a channel tapering of 90 % each, these two designs are used for a closer comparison in this work and summarized in figure 3.38. An evaluation of the covered areas in the channels was done by Ruth Kranz.

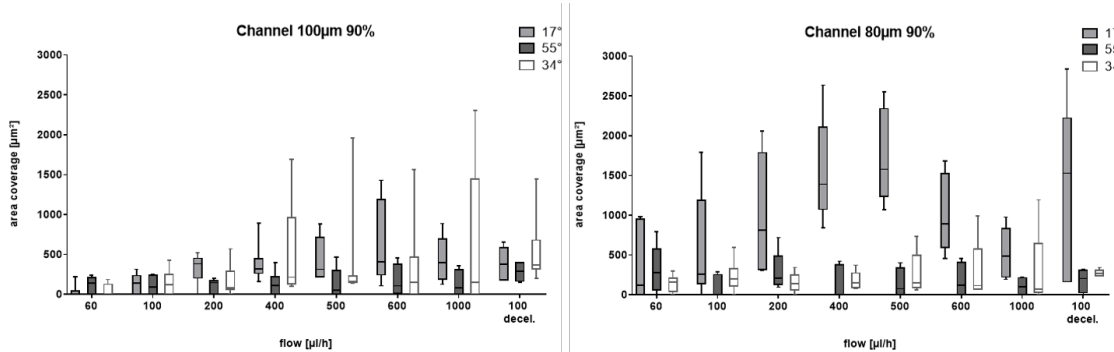


Figure 3.38: Comparison of the area coverage of the two channel structures that led to the best experimental results, channel width of 100 μm (left) and 80 μm (right) with a channel tapering of 90 % each. These graphics were made and provided by Ruth Kranz.

We demonstrate apparent that at both channel widths the largest area covered by the thrombus is achieved at an angle of 17° of the channel tapering. This result is independent of the flow rate used in each experiment. Likewise, it becomes clear in figure 3.38 that the largest thrombi are formed in microfluidic channels with a channel width of 80 μm and a channel tapering of 90%.

Therefore, further experiments were performed only in this channel structure. An example of this is shown in figure 3.39. With this channel structure conditions could

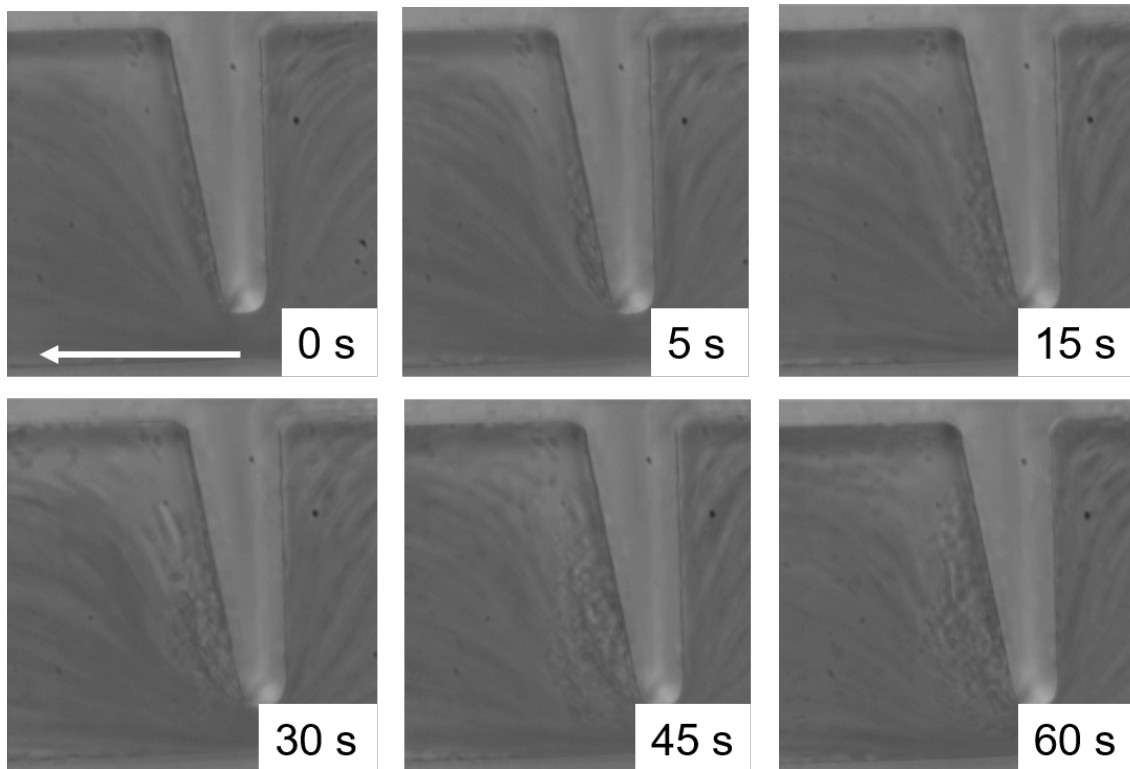


Figure 3.39: Screenshots of a high-speed camera video of an experiment where mice blood was infused with a flow rate of $200 \mu\text{L/h}$ through the microfluidic chip. The channel width was $80 \mu\text{m}$, the channel height $30 \mu\text{m}$. The arrow indicates the direction of the flow.

be created that enable investigating the formation of the thrombus. Moreover studying the thrombus fanning out, cutting off and the rolling of platelets over a longer period of time was also possible. Another observation was made during the entire time: the thrombi were always formed behind the channel tapering and not in the channel gap, which is theoretically expected, as the simulation of Prof. Dr. S. Gekle in figure 3.40 shows.

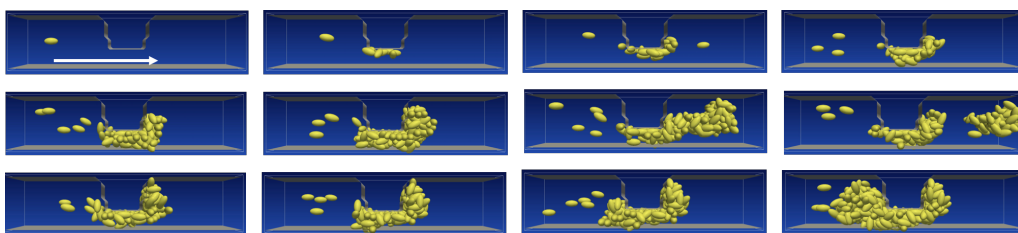


Figure 3.40: Simulation of a thrombus formation made and provided by Prof. Dr. S. Gekle. Order of images: from left to right and from top to bottom. The arrow indicates the direction of the flow.

Based on these experimental results and the simulations, the following considerations have emerged: Two mechanisms are conceivable, why the thrombus arises behind the channel tapering and not exactly in this channel gap, which is theoretically expected:

1. The platelets do not have enough time to bind to the top of the tapering and therefore bind only in the slower area behind.
2. The platelets bind on the tapering, but are immediately torn off again and only stick behind, where the shear forces are significantly lower.

In the first case, the thrombus should be able to form on this plateau if this would be much longer, but not in the second case. For this purpose, channel structures were designed, in which the channel width is still $80\ \mu\text{m}$ and the channel tapering 90% . Only the plateau lengths were increased by the factors 3 to 5, which is displayed in figure 3.41.

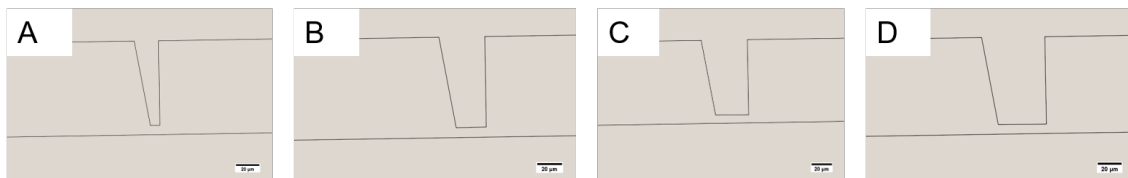


Figure 3.41: Sketches of the excerpts of the designs of the microfluidic channels with a channel width of $80\ \mu\text{m}$ and a longer plateau at the channel tapering (scale bar: $20\ \mu\text{m}$). From left (A) to right (D): plateau length = $8\ \mu\text{m}$ (original), plateau length = $24\ \mu\text{m}$ (factor 3), plateau length = $32\ \mu\text{m}$ (factor 4) and plateau length = $40\ \mu\text{m}$ (factor 5).

Since the experiments for this have yet to be carried out, no further results and findings are available.

Another aspect for future experiments could be the change in flow rate during the experiment. This could model the pulsation of the heart. In flow regions with time-varying shear stresses, a low shear stress follows a high shear stress due to the blood pulse. This can also lead to platelet aggregation.^[69] Or the blood from different knockout mouse lines can be used to investigate how important individual proteins are.

3.3.2 Design development and production of microfluidic bioreactors

3.3.2.1 Description of the experiments

The aim of this cooperation was to investigate in vitro the formation of proplatelets to platelets and the constriction process of platelets. Doing this under dynamic conditions, at first microfluidic bioreactors were produced, as described in chapter 3.3.

As a very large purpose of such work, it can be considered that more blood transfusions, which are donor-independent, can be provided in future thereby. The microfluidic chips, made of PDMS, serve to model the human bone marrow. PDMS is a cell-inert, transparent silicone that provide some strength and is still flexible, which is necessary for this experiments.

In a standard experiment, which setup is shown in figure 3.42 A, at the beginning the microfluidic bioreactors were infused with a BSA-solution to saturate unspecific bonds.

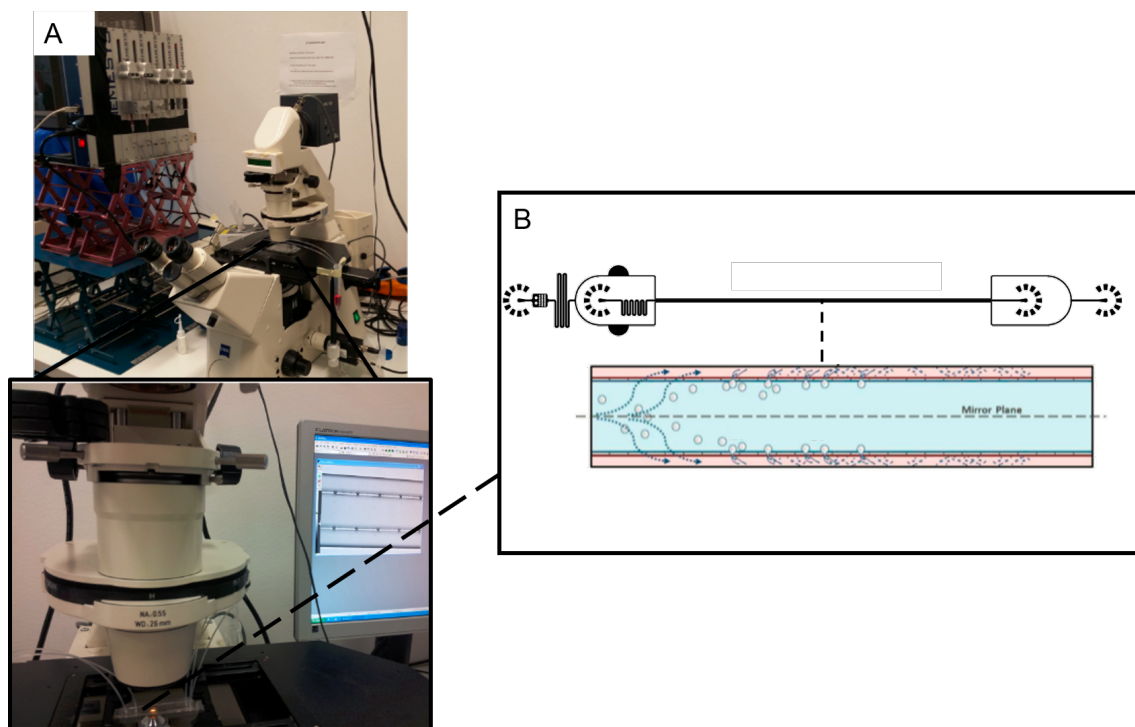


Figure 3.42: Demonstration of the experimental setup (A) and illustration of the bioreactor experiments (B). The lower photo of (A) and the lower sketch of (B) were made and provided by Dr. Markus Bender.

In a second step the channels were rinsed with a medium-solution. This CO_2 independent, phenol-red free medium is a mixture of several salts, glucose, amino acids, L-glutamine, penicillin-streptomycin, HEPES buffer and serum.

In the last step, the actual experiment is performed. For this, megakaryocytes in the medium are infused through the bioreactor (figure 3.42 B). The design by Thon et al.^[16] served as a guideline for our first design development.

To achieve the best possible results, the channel designs were changed and optimized several times. The design development will be discussed in more detail below. In order to illustrate the individual steps better, several results are shown in this thesis too, but their biological analysis is not part of this work.

3.3.2.2 Discussion of the results

Figure 3.43 shows an example of one of the first channel designs for these experiments. There are two inlets, one with a filter, and two outlets. The channel length is 2.5 cm, the channel width 260 μm and the channel height 35 μm . Here, the channel width is divided into 3 areas: the outer channels are each 60 μm wide and the inner region 120 μm . The gap dimension is 2 μm and the partitions have a size of 10 μm · 90 μm .

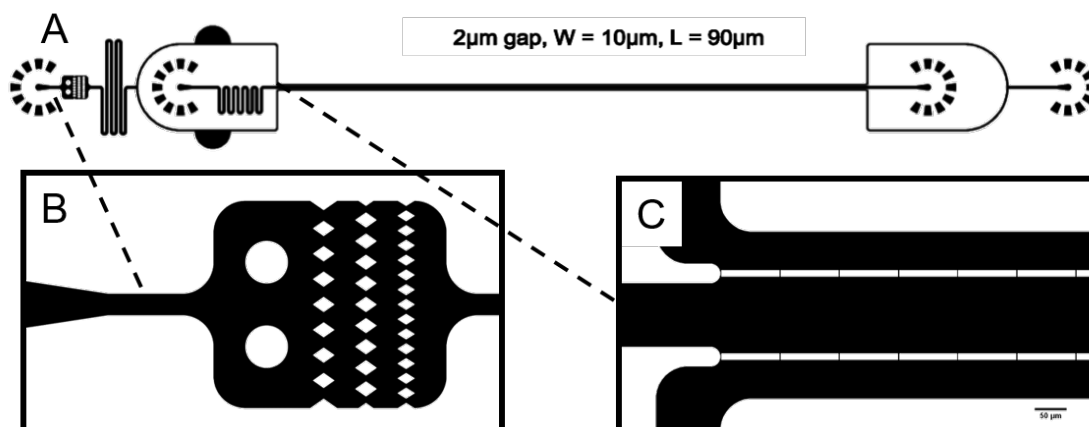


Figure 3.43: Exemplary sketch of one of the first bioreactor-designs (A) with two inlets, one with a filter (B), and two outlets. The total length of the channel is 2.5 cm, the total width 260 μm . Here, the channel width is divided into 3 areas (C) (scale bar: 50 μm).

The special about this structure was the 2-layer design in producing the microfluidic chip. This means that the gaps did not go over the entire channel height, they had only a height of 5 μm .

An exemplary early experiment is shown in figure 3.44. Proplatelets formed from megakaryocytes and platelet release at the tip of the proplatelet was observed. The rolling and the cutting off of the platelet (marked by a black circle) were investigated.

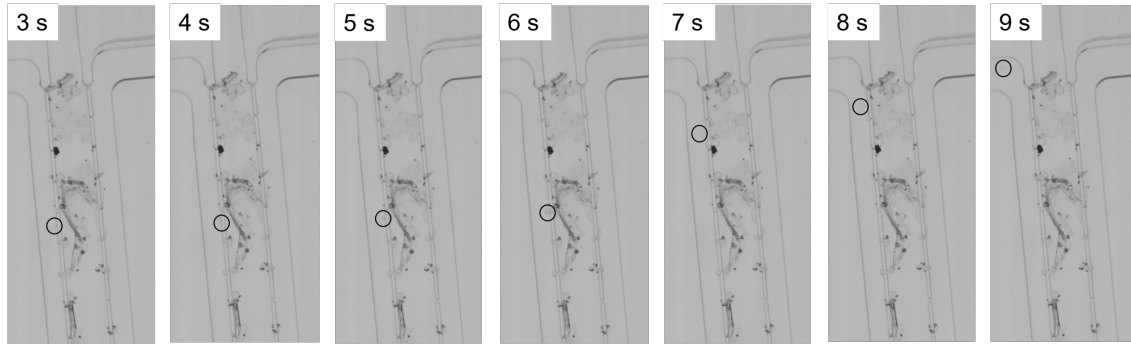


Figure 3.44: Screenshots of a video of an early experiment in which megakaryocytes in the medium were infused through the bioreactor with a flow rate of 200 $\mu\text{l}/\text{h}$.

Since many non-satisfying results were determined and most of the experiments had to be interrupted due to blockages in the channels, some design changes have been made.

1. The design was changed from a 2-layer- to a 1-layer-design, so that the gaps could extend to the entire channel height. As a result, it was hoped, that there would be less blockages in the microfluidic channel at these points and the contaminants would be washed away if necessary.
2. To get fewer impurities into the main channel, more filters were integrated into the design.
3. The number of channel outlets was reduced to one, as a result of previous experiments in which always one channel outlet was closed, because there was no use for it.
4. Another change was variations in channel width.

Figure 3.45 shows exemplary one of the microfluidic bioreactors of the second design step. The channel length is 2.5 cm, the channel height 35 μm and the channel width 500 μm , which is divided into 3 areas.

The outer channels are each 60 μm wide and the inner region 360 μm . The gap dimensions are 2 μm , the partitions have a dimension of 10 x 90 μm . Due to the 1-layer-design the gaps extend to the entire channel height.

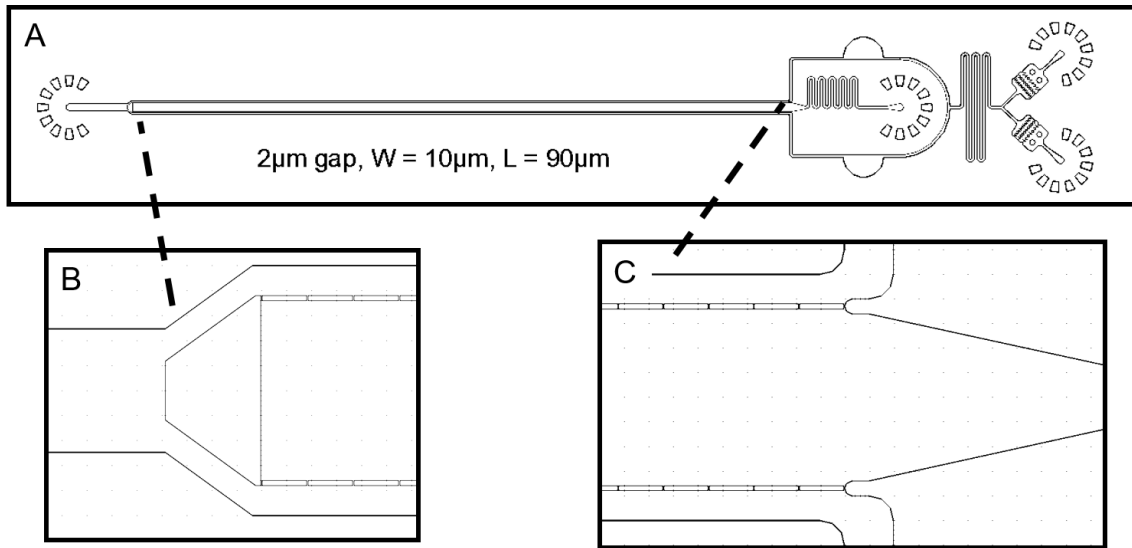


Figure 3.45: Exemplary sketch of one of channel structures of the second design step (A) with more filters and just one channel outlet (B). The total length of the channel is 2.5 cm, the total width 500 µm. Here, the channel width is also divided into 3 areas. (C)

Figure 3.46 displays some screenshots of an high-speed camera video of an experiment with such a new channel structure. Formation and extension of proplatelets could be studied as the changes of the positions of the colored marks this figure.

The megakaryocytes in the medium where infused through the bioreactor with a flow rate of 200 µL/h.

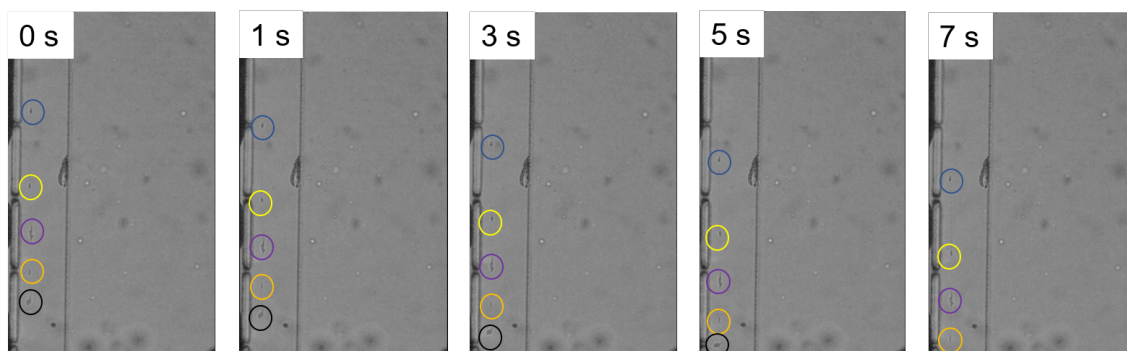


Figure 3.46: Screenshots of a high-speed camera video of a moment of an experiment where the string of beads-like cutting off process is studied.

In addition to this used channel structure (figure 3.47 D), there were other structures in this step of design development where a very large area of pillars was attached to the end of the main channel (figure 3.47 A and B).

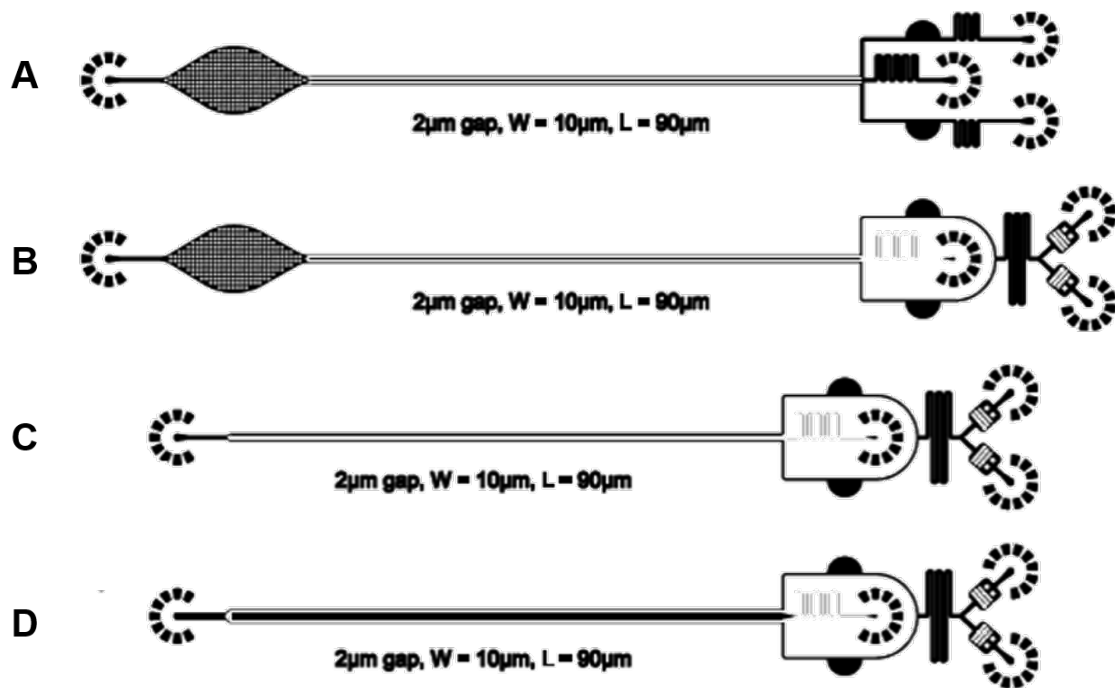


Figure 3.47: Summary of all new designed microfluidic bioreactor structures of this development step.

In these areas no new observations could be made. There was the consideration that maybe between the pillars also constrictions of proplatelets to platelets could result. But it only collects the contaminants. Due to this findings, in another step of design development (and the last one during this work), which is shown in figure 3.48, the number of filters was reduced or completely omitted and the size of the gap was increased to 3 µm partially. This should simplify the handling when producing the chips and is now again similar to the as a guideline used design by Thon et al.^[16]

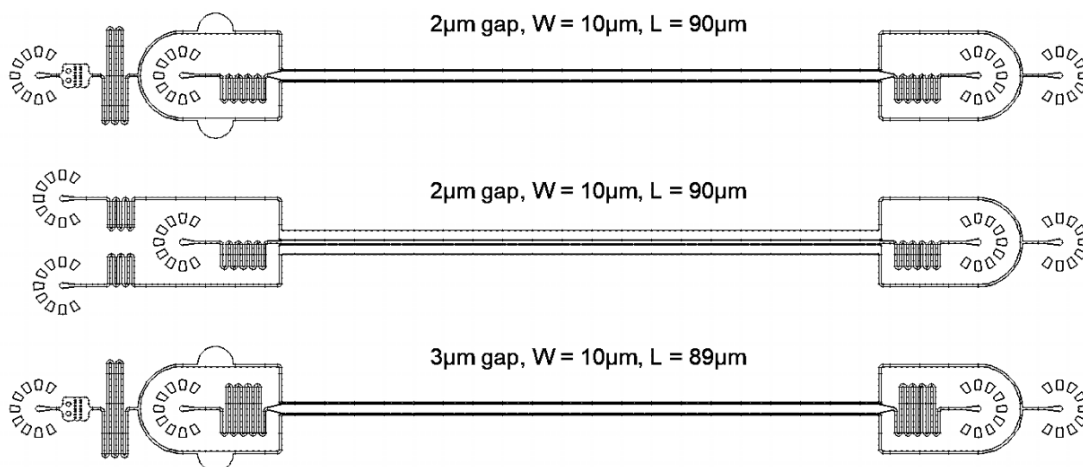


Figure 3.48: Sketches of the last design change during this work of the microfluidic bioreactor structures.

4 Conclusion and future perspective

Due to successful measurements by means of the combination of time-resolved in situ SAXS, WAXS and UV-Vis measurements, the kinetic of nucleation and growth of ZnO nanoparticles was investigated during this work. Two different set-ups were used: a microfluidic capillary with a mixer for short time scales and a "steady" capillary for longer times.

An important point of my work was that the in situ investigation has been performed using a lab based instrument, which is one of the first example of in situ SAXS/WAXS study with a lab instrument.

I also reported on palladium nanoparticles and how the first steps of their formation proceed in solution. For this I applied SAXS measurements at the DESY synchrotron in Hamburg.

The kinetic studies of the nanoparticle syntheses during this work have shown that current X-ray laboratory technology is sufficient to conduct in situ SAXS/WAXS studies previously available only in synchrotron X-ray equipment.

However, the synchrotron measurements are necessary to perform measurements in very low concentration solutions and to measure scattering curves with higher temporal resolution (0.5 seconds) and higher signal-to-noise ratio.

Furthermore, 2D microfluidic chips were designed, developed and produced for the use in biological and medical experiments in vitro under dynamic conditions.

In summary this work describes following significant results, which were accomplished:

1. The experimental set-up for performing in situ kinetics measurements has been optimized, making it possible to study nanoparticle syntheses with high reaction temperatures, using the largest possible number of analysis and characterization methods.
2. In-situ SAXS/WAXS/UV-Vis-experiments were performed to follow the nucleation and growth of ZnO nanoparticles from oleate precursors in-situ over time scales from 30 seconds to 18 hours to cover the whole nucleation as well as the early and late growth period.

3. The in situ investigation of the ZnO nanoparticles has been performed using a lab based X-ray scattering instrument.
4. To observe the growth of Pd nanoparticles in millisecond time steps, in-situ SAXS-experiments were performed at a synchrotron.
5. Two-dimensional microfluidic chips made out of PDMS and glass have been optimized and designed that stenosis experiments could be carried out in vitro under dynamic conditions and large-scale thrombi could be formed.
6. The design of two-dimensional PDMS and glass microfluidic bioreactors was optimized to enable experiments to be performed to closely observe the formation of megakaryocytes to platelets in vitro under dynamic conditions.

Due to the optimization of the capillary holder for the in-situ kinetic experiments, numerous further investigations of high-temperature nanoparticle syntheses are possible. The possibilities offered by a 3D printer are meanwhile so far advanced that it is also possible to print capillary holders made of high-temperature-stable polymers (for example polyimides). They withstand very high temperatures and furthermore there is a lower heat loss due to the smaller amount of metal used in the setup.

Thus, it should even be possible to investigate the kinetics of, for example, iron oxide nanoparticles at a reaction temperature more than 200 °C, in order to be able to deal more closely with the shape change from spherical to cubic iron oxide nanoparticles.

Even in the case of the stenosis experiments and the experiments in the bioreactors, there is still a number of challenges for future work to solve:

1. Another aspect of future stenosis experiments could be the change in flow rate during the experiment. This could model the pulsation of the heart. In low regions with time-varying shear stresses, low shear stress follows high shear stress due to the blood pulse. This can also lead to platelet aggregation.
2. Equally the blood from different knockout mouse lines can be used to investigate how important individual proteins are.
3. A big goal in the further optimization and research with the bioreactor can be the enabling of donor independent blood transfusion.

The presented ideas show that there is still a broad implication for future work in this field of study.

Nevertheless, the results of this work extend the knowledge about the kinetics of high-temperature nanoparticle syntheses and the using of microfluidic chips as bioreactors. During this work, promising results were shown for future applications.

5 Experimental Methods

This chapter includes general description of the experimental methods and instrumentation used throughout this work. The details of the experiments and the techniques relevant for the respective experiment are described in the corresponding chapter in "Results and Discussion".

5.1 Materials

All chemicals were used as received in the highest available purity, which are summarized in table 5.1. The microfluidic devices (PDMS-chips and quartz capillaries) were connected to the syringe pumps via LDPE tubing (SCI Science Commodities Inc.).

For the X-ray scattering experiments 1 mm quartz capillaries with a wall thickness of 10 μm from Hilgenberg GmbH were used as analysis cells. The capillary holder was 3D-printed using ABS (iGo3D).

Table 5.1: List of manufacturers and purities of the used chemicals

Substance	Purity	Manufacturer
sodium oleate	>97.0 %	TCI Europe
zinc chloride	98 %	Grüssing GmbH
tetrahydrofuran	99.9 %	Sigma-Aldrich
tetrabutylammonium hydroxide	1 M in methanol	Sigma-Aldrich
oleylamine	>98.0 %	Sigma-Aldrich
palladium(II) acetylacetonate	99 %	Sigma-Aldrich
borane tert-butylamine complex	97 %	Sigma-Aldrich
Sylgard® 184	-	Dow Corning
2-propanol	99,95 %	Carl Roth GmbH + Co. KG
NANO™ SU photo resist	-	MicroChem Corporation obtained from: micro resist technology GmbH
developer mr-DEV 600	-	Dow Corning

5.2 Synthesis regulations

5.2.1 Zinc oxide nanoparticles

5.2.1.1 Syntheses of zinc oleate

For the synthesis first 2.73 g (20 mmol) of zinc chloride was dissolved in 75 mL water. In addition, 12.16 g (40 mmol) of sodium oleate must be dissolved in 75 mL water at a temperature between 50 °C and 60 °C.

The zinc oleate was synthesized by adding the solution of sodium oleate to a solution of zinc chloride. The resulting precipitate was filtered, washed with warm water (~45 °C) and dried over night at 50 °C in a vacuum oven.

5.2.1.2 Syntheses of zinc oxide nanoparticles

In a standard experiment, zinc oleate was prepared in THF by sonication at 45 °C. For fast mixing, the two reaction solutions (oleate solution and the hydrolysis agent) were pumped with a high precision pump from neMESYS through a Y-shaped Teflon mixer via LDPE tubing (inner diameter: 0.38 mm, outer diameter: 1.09 mm) at high flow rates with a volume ratio 1 : 5 (TBAH : oleate solution) into a quartz capillary. This was heated in a 3D-printed in situ holder integrated with a heating copper tube. When the stationary flow conditions were reached, the pumps were stopped.

For longer investigation times the reaction has to be carried out in a closed quartz capillary due to the evaporation of THF at high temperatures. Therefore TBAH was added to the 2 mL zinc oleate solution. After this the capillary was filled with this reaction mixture and closed with hot glue before starting the measurements and the heating.

5.2.2 Palladium nanoparticles

For preparation, palladium(II) acetylacetonate and borane tert-butylamine complex were respectively solved in oleylamine by sonication at 50 °C.

The Pd(acac)₂-solution of 16.41 mM was added to the BTB-solution of 1.14 M or 0.57 M in a ratio of 5 to 1.

After this, the quartz capillary was filled with this reaction mixture and closed with hot glue before starting the heating process in a heating cell (Linkam HT600) and the SAXS measurements.

5.3 Microfluidic device fabrication

5.3.1 Production of moldings by Photolithography

In a ISO 5 class cleanroom, the photolithographic production of casting templates, the silicon masters, was carried out. The exposure by amber light is used to simplify the handling of the UV-sensitiv negative photoresist.

The silicon wafer (type P/Boron <100>, SI-MAT, diameter 50.0 ± 0.5 mm, thickness 256-306 μm) is first cleaned with isopropanol and then dried with compressed air.

The degassed photoresist is applied to the wafer surface (see figure 5.1 A) and distributed according to the summarized values in table 5.2 for the spin coating velocities^[52,53] and then cured in two stages normally, the prebake and softbake.

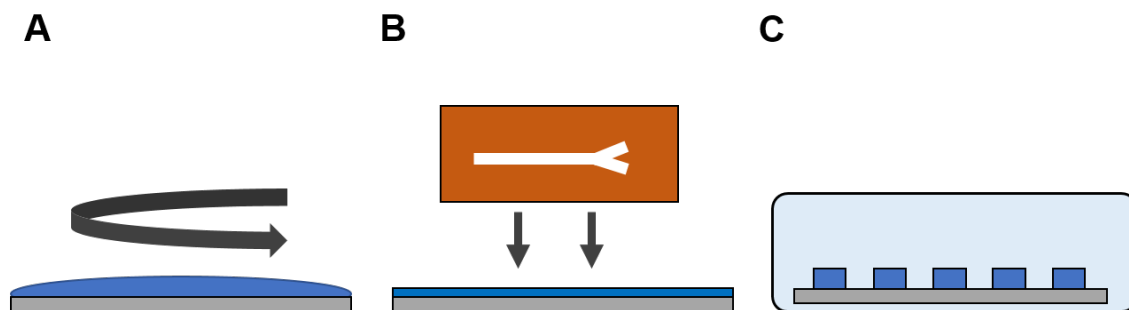


Figure 5.1: Sketches of the production of moldings by photolithography.

This is followed by two exposure-steps with UV light in a mask aligner (Süss MicroTech with Hg lamp, 365 nm), which completes the cross linking of the negative photoresist (see figure 5.1 B). The designed structure was hardened in the post exposure bake. After this the unpolymerized photoresist was removed in a developer bath (mr-DEV 600; Dow Corning) (see figure 5.1 C). Due to the extremely small structures, the use of a chrome photomask (JD Photodata) was necessary.

Table 5.2: Process parameters for the fabrication of microstructured 2D microfluidic channels

Fabricationstep	Parameters			
layer thickness	30 μm	20 μm	10 μm	5 μm
photoresist	SU 8 - 25	SU 8 - 2015	SU 8 - 2015	SU 8 - 2005
spin coating velocities	1650 rpm	2000 rpm	4000 rpm	2500 rpm
prebake (65°C)	4 min	—	—	—
softbake (90°C)	10 min	6 min	12 min	2 min
exposure time (365nm)	2 x 4 s	2 x 4 s	2 x 4 s	2 x 3 s
PEB 1 (65°C)	1 min	—	—	—
PEB 2 (90°C)	3.5 min	8 min	15 min	3 min
developer bath	10 min	10 min	10 min	10 min

5.3.2 Production of channel structure templates by softlithography

The replication of channel structures by PDMS and the fabrication of microfluidic devices was performed in a Scanlaf Flowbox, class 2 with laminar suppression flow.

For soft lithographic replication, the PDMS oligomer Sylgard® 184 was mixed in a weight ratio of 10 : 1 with the associated crosslinker and stirred on the silicon wafer (see figure 5.2 A), placed in a Petri dish. This was degassed for at least 45 min in the desiccator before being cured for 2 hours at 75 °C (see figure 5.2 B).

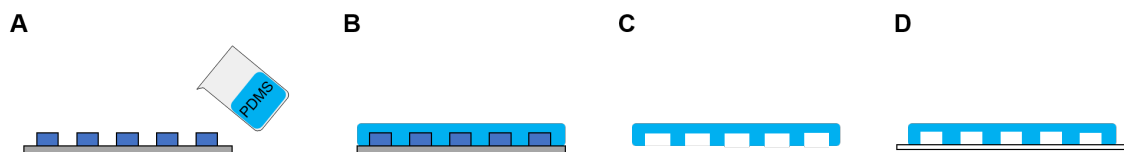


Figure 5.2: Sketches of the production of moldings by photolithography.

With a scalpel, the microstructure was cut out and removed from the mold (see figure 5.2 C). The connections for inlet and outlet were punched out with a hole-puncher (UniCore; 0.75 mm). After all the PDMS structure was cleaned with isopropanol and then dried again with compressed air.

Thereafter, the PDMS structure is sealed with a glass slide that is covalently bonded to the PDMS surface (see figure 5.2 D). This Bonding is generated in a condensation reaction between silanol groups on the PDMS and glass surface^[58] that have been previously induced in an air oxygen plasma-oven (MiniFlecto® PC-MFC, Plasma Technology GmbH).

5.3.3 Device handling

Before each experiment, the devices were checked for leak tightness as well as the tubing connections by the corresponding solvent through the microfluidic system. For the control and manipulation of laminar flowprofiles in microfluidic devices, the modular syringe pump system neMESYS®, New Modular Exptensible Syringe pump System (Cetoni GmbH) was used.

According to the microfluidic system geometry, a corresponding number of dosing units were deployed, whose servomotors could be operated individually via the neMESYS user interface. Hamilton syringes (gas-tight glass syringes) in the sizes of 0.5 mL and 1.0 mL were used for the microfluidic kinetic experiments and 1.0 mL PE syringes (BBraun) for the stenosis and the bioreactor experiments.

The syringes were connected with dialysis tube ends (BBraun) and PE-tubing (Scientific Commodities Inc.) to the microfluidic device inlets and outlets.

5.3.4 Producing of heating foils

For the production of heating foils, a Kapton foil from *Du Pont* was first provided with copper tape (figure 5.3 A). Subsequently, the one-component heating varnish *ACR-100* from *Future Carbon* was applied between the copper strips (figure 5.3 B) and evenly distributed with a glass slide (figure 5.3 C).

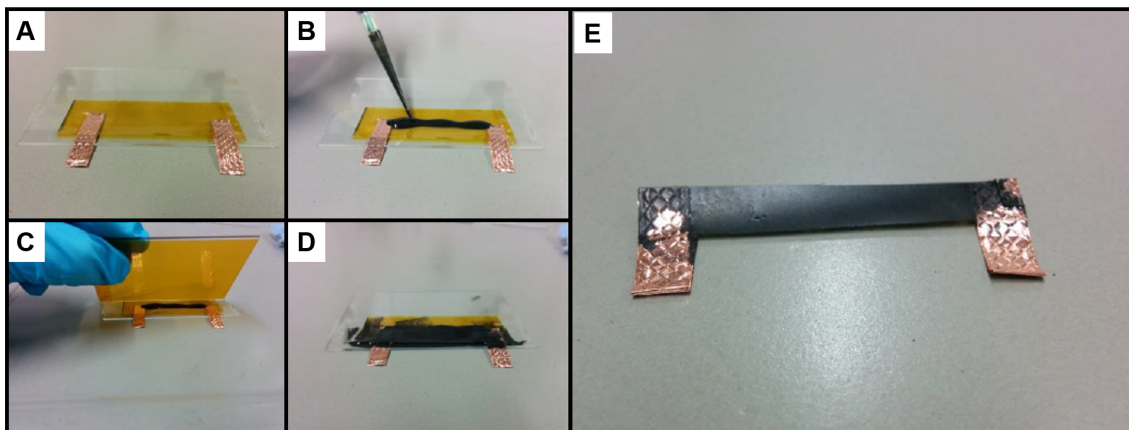


Figure 5.3: Presentation of the production of heating foils for microfluidic high temperature syntheses.

The drying of the heating varnish took place in 24 hours at 100 °C or even at room temperature over a period of 3 days (figure 5.3 D).

The heating foils made in this way (figure 5.3 E) were attached to the tubes with Kapton tape from scotch.

The temperature was controlled by power supply using laboratory power supplies from *Reichelt Elektronik*.

5.4 Instrumentation

5.4.1 Microfluidic SAXS/WAXS/UV-Vis - Ganesha

In situ SAXS/WAXS experiments were performed with a “Double Ganesha AIR” system (SAXSLAB, Denmark). The X-ray source of this laboratory-based system is a rotating anode (copper, MicroMax 007HF, Rigaku Corporation, Japan) providing a microfocused beam at $\lambda = 0.154$ nm.

The scattering data were recorded by position sensitive detectors (Pilatus 300K for SAXS and Pilatus 100K for WAXS, Dectris). The SAXS-detector is located in an evacuated tube with a sample-distance of ca. 40 cm, thus leading a q -range from 0.28 nm to 5 nm⁻¹. Here q is the magnitude of the scattering wave vector defined as

$$q = \frac{4}{\lambda} \sin\left(\frac{\theta}{2}\right), \quad (5.1)$$

where θ is the scattering angle and λ is the wavelength of the X-ray.

The WAXS-detector has an unusual position of ca. 1.8 cm above the microfluidic cell, which is necessary to maximize the signal-noise-ratio.

A fiber optics UV/Vis-spectrometer (light source: Ocean Optics, DH 2000 BAL, spectrometer: Ocean Optics, USB2000+XR1-ES) measures the absorbance-spectra within the scattering volume.

5.4.2 Synchrotron Small-Angle X-ray Scattering

The SAXS experiments were performed at Petra III/DESY Hamburg at the beamline P03 ($\lambda = 0.093$ nm) with a sampledetector distance of ca. 1.60 m. For the detection of the scattering patterns a PILATUS 1 M fast-readout detector was used.

5.4.3 SAXS/WAXS Data Analysis

As a standard for calibration silver behenate with a d -spacing of 58.38 Å was used. The X-ray path is evacuated, except at the position where the sample was set. The 2D patterns for both methods at the Ganesha were acquired at an interval of 30 s, 60 s and 600 s. The interval for the long time measurements in a closed capillary was 1200 s for each data point.

For the SAXS experiments at the DESY beamline P03 the measurement time for each pattern was 0.5 s. The obtained 1D profiles were corrected by the corresponding solvent as a background and analyzed by the software *scatter*^[93].

5.4.4 3D-printing

The capillary holder used for the kinetic experiments was 3D-printed by a Ultimaker UM2 3D-printer. The design was previously drawn with AutoCAD.

5.4.5 Transmission Electron Microscopy

The images of the zinc oxide and palladium nanoparticles were recorded using a Zeiss CEM 922 Omega transmission electron microscope, operating at a high voltage of 200 kV. The samples have been coated on carbon-coated copper grids and examined. The TEM images have been evaluated using the software *Image J*.

5.4.6 Optical microscopy

The light micrographs were acquired with an Olympus XI 71 (Olympus, Hamburg, Germany) using four times magnification lenses. The pictures were taken with an Olympus XC 30 camera (Olympus, Hamburg, Germany). The images have been evaluated using the software *Image J*.

5.4.7 Infrared camera

The thermal images were taken with a *Fluke Ti32* infrared camera. An emissivity of 0.95 was set for the investigation of the experimental equipment assembled from light transmittance plastics. The evaluation of the data was done with the software *Smart View 3.4*.

References

- [1] Dieter Vollath. *Nanoparticles-Nanocomposites & Nanomaterials: An Introduction for Beginners*. John Wiley & Sons, 2013.
- [2] Tamás Vicsek. *Fractal growth phenomena*. World scientific, 1992.
- [3] Martin Trebbin. *Microfluidics at high-intensity X-ray sources: from microflow chips to microfluidic liquid jet systems*. PhD dissertation, University of Bayreuth, 2013.
- [4] Tao Li, Andrew J Senesi, and Byeongdu Lee. Small angle x-ray scattering for nanoparticle research. *Chemical reviews*, 116(18):11128–11180, 2016.
- [5] George M Whitesides. The origins and the future of microfluidics. *Nature*, 442(7101):368, 2006.
- [6] Thomas Franke and Achim Wixforth. Das labor auf dem chip: Mikrofluidik. *Physik in unserer Zeit*, 38(2):88–94, 2007.
- [7] Yujun Song, Josef Hormes, and Challa SSR Kumar. Microfluidic synthesis of nanomaterials. *small*, 4(6):698–711, 2008.
- [8] Yujun Song, EE Doomes, John Prindle, Roland Tittsworth, Josef Hormes, and Challa SS R Kumar. Investigations into sulfobetaine-stabilized cu nanoparticle formation: toward development of a microfluidic synthesis. *The Journal of Physical Chemistry B*, 109(19):9330–9338, 2005.
- [9] Martin Pumera. Nanomaterials meet microfluidics. *Chemical Communications*, 47(20):5671–5680, 2011.
- [10] Sang Hyun Lee, Hyun Jung Lee, Dongcheol Oh, Seog Woo Lee, Hiroki Goto, Ryan Buckmaster, Tomoyuki Yasukawa, Tomokazu Matsue, Soon-Ku Hong, HyunChul Ko, et al. Control of the zno nanowires nucleation site using microfluidic channels. *The Journal of Physical Chemistry B*, 110(9):3856–3859, 2006.
- [11] Susanne Seibt, Paul Mulvaney, and Stephan Förster. Millisecond cds nanocrystal nucleation and growth studied by microfluidics with in situ spectroscopy. *Colloids and Surfaces A: Physicochemical and Engineering Aspects*, 562:263–269, 2019.
- [12] Yujun Song, Daojian Cheng, and Liang Zhao. *Microfluidics: Fundamentals, Devices, and Applications*. John Wiley & Sons, 2018.

-
- [13] Limin Qi, Helmut Cölfen, and Markus Antonietti. Synthesis and characterization of cds nanoparticles stabilized by double-hydrophilic block copolymers. *Nano Letters*, 1(2):61–65, 2001.
- [14] Sruti Hemachandran Menon. Pbs quantum dots: Synthesis and optical properties.
- [15] Xuelian Chen, Jan Schröder, Stephan Hauschild, Sabine Rosenfeldt, Martin Dulle, and Stephan Förster. Simultaneous saxs/waxs/uv-vis study of the nucleation and growth of nanoparticles: a test of classical nucleation theory. *Langmuir*, 31.
- [16] Jonathan N Thon, Linas Mazutis, Stephen Wu, Joanna L Sylman, Allen Ehrlicher, Kellie R Machlus, Qiang Feng, Shijiang Lu, Robert Lanza, Keith B Neeves, et al. Platelet bioreactor-on-a-chip. *Blood*, pages blood–2014, 2014.
- [17] Jonathan N Thon, Douglas A Medvetz, SM Karlsson, and Joseph E Italiano Jr. Road blocks in making platelets for transfusion. *Journal of Thrombosis and Haemostasis*, 13:S55–S62, 2015.
- [18] Michele P Lambert, Spencer K Sullivan, Rudy Fuentes, Deborah L French, and Mortimer Poncz. Challenges and promises for the development of donor-independent platelet transfusions. *Blood*, 121(17):3319–3324, 2013.
- [19] Sascha Ehlert, Thomas Lunkenbein, Josef Breu, and Stephan Förster. Facile large-scale synthetic route to monodisperse zno nanocrystals. *Colloids and Surfaces A: Physicochemical and Engineering Aspects*, 444:76–80, 2014.
- [20] Ranjani Viswanatha, Sameer Sapra, B Satpati, PV Satyam, BN Dev, and DD Sarma. Understanding the quantum size effects in zno nanocrystals. *Journal of Materials Chemistry*, 14(4):661–668, 2004.
- [21] S Monticone, R Tufeu, and AV Kanaev. Complex nature of the uv and visible fluorescence of colloidal zno nanoparticles. *The Journal of Physical Chemistry B*, 102(16):2854–2862, 1998.
- [22] Doris Segets, Lars Martinez Tomalino, Johannes Gradl, and Wolfgang Peukert. Real-time monitoring of the nucleation and growth of zno nanoparticles using an optical hyper-rayleigh scattering method. *The Journal of Physical Chemistry C*, 113(28):11995–12001, 2009.
- [23] Marko Bitenc, Peter Podbršek, Pavo Dubek, Sigrid Bernstorff, Goran Draži, Bojan Orel, and Zorica Crnjak Orel. The growth mechanism of zinc oxide and hydrozincite: a study using electron microscopies and in situ saxs. *CrystEngComm*, 14(9):3080–3088, 2012.

- [24] Mirijam Zobel, Anna Windmüller, Ella M Schmidt, Klaus Götz, Theodor Milek, Dirk Zahn, Simon AJ Kimber, Jessica M Hudspeth, and Reinhard B Neder. The evolution of crystalline ordering for ligand-ornamented zinc oxide nanoparticles. *CrystEngComm*, 18(12):2163–2172, 2016.
- [25] Ivan Saldan, Yuriy Semenyuk, Iryna Marchuk, and Oleksandr Reshetnyak. Chemical synthesis and application of palladium nanoparticles. *Journal of materials science*, 50(6):2337–2354, 2015.
- [26] Sang-Wook Kim, Jongnam Park, Youngjin Jang, Yunhee Chung, Sujin Hwang, Taeghwan Hyeon, and Young Woon Kim. Synthesis of monodisperse palladium nanoparticles. *Nano Letters*, 3(9):1289–1291, 2003.
- [27] Vismadeb Mazumder and Shouheng Sun. Oleylamine-mediated synthesis of pd nanoparticles for catalytic formic acid oxidation. *Journal of the American Chemical Society*, 131(13):4588–4589, 2009.
- [28] F Bonet, S Grugeon, R Herrera Urbina, K Tekaia-Elhsissen, and J-M Tarascon. In situ deposition of silver and palladium nanoparticles prepared by the polyol process, and their performance as catalytic converters of automobile exhaust gases. *Solid state sciences*, 4(5):665–670, 2002.
- [29] Karl Winnacker and Leopold Küchler. *Chemische Technik: Prozesse und Produkte*. Wiley-VCH-Verlag, 2004.
- [30] Didier Astruc, Feng Lu, and Jaime Ruiz Aranzaes. Nanoparticles as recyclable catalysts: the frontier between homogeneous and heterogeneous catalysis. *Angewandte Chemie International Edition*, 44(48):7852–7872, 2005.
- [31] An-Hui Lu, Elena Lorena Salabas, and Ferdi Schüth. Magnetische nanopartikel: synthese, stabilisierung, funktionalisierung und anwendung. *Angewandte Chemie*, 119(8):1242–1266, 2007.
- [32] Manuela Gehring. *Untersuchungen zur Stabilität von Halbleiternanopartikeln, deren Biokonjugationen mittels Staudinger Ligation und Zellaufnahmestudien solcher Systeme*. PhD dissertation, University of Hamburg, 2014.
- [33] D Mijatovic, Jan CT Eijkel, and Albert van den Berg. Technologies for nanofluidic systems: top-down vs. bottom-up—a review. *Lab on a Chip*, 5(5):492–500, 2005.
- [34] C Raab, M Simkó, A Gázsó, U Fiedeler, and M Nentwich. Was sind synthetische nanopartikel. *NanoTrust-Dossiers Nr, 2*, 2008.

- [35] Victor K LaMer and Robert H Dinegar. Theory, production and mechanism of formation of monodispersed hydrosols. *Journal of the American Chemical Society*, 72(11):4847–4854, 1950.
- [36] Jongnam Park, Jin Joo, Soon Gu Kwon, Youngjin Jang, and Taeghwan Hyeon. Synthesis of monodisperse spherical nanocrystals. *Angewandte Chemie International Edition*, 46(25):4630–4660, 2007.
- [37] Peter William Atkins and Julio De Paula. *Physikalische chemie*. John Wiley & Sons, 2013.
- [38] Young-wook Jun, Jin-sil Choi, and Jinwoo Cheon. Shape control of semiconductor and metal oxide nanocrystals through nonhydrolytic colloidal routes. *Angewandte Chemie International Edition*, 45(21):3414–3439, 2006.
- [39] Nastassja Lewinski, Vicki Colvin, and Rebekah Drezek. Cytotoxicity of nanoparticles. *small*, 4(1):26–49, 2008.
- [40] Bruno L Caetano, Valerie Briois, Sandra H Pulcinelli, Florian Meneau, and Celso V Santilli. Revisiting the zno q-dot formation toward an integrated growth model: From coupled time resolved uv-vis/saxs/xas data to multivariate analysis. *The Journal of Physical Chemistry C*, 121(1):886–895, 2016.
- [41] Diana Yanover, Richard K Capek, Anna Rubin-Brusilovski, Roman Vaxenburg, Nathan Grumbach, Georgy I Maikov, Olga Solomeshch, Aldona Sashchiuk, and Efrat Lifshitz. Small-sized pbse/pbs core/shell colloidal quantum dots. *Chemistry of Materials*, 24(22):4417–4423, 2012.
- [42] Abdelrazek Mousa. *Synthesis and Characterization of PbS Quantum Dots*. PhD dissertation, Lund University, 2011.
- [43] Sascha Ehlert. *Preparation of Fully Miscible Nanocomposites*. PhD dissertation, University of Bayreuth, 2014.
- [44] E Riedel and C Janiak. *Anorganische Chemie, 7. Auflage*. Walter de Gruyter, Berlin, 2007.
- [45] Stephan Förster. Amphiphilic block copolymers for templating applications. In *Colloid Chemistry I*, pages 1–28. Springer, 2003.
- [46] Daniel L Fedlheim and Colby A Foss. *Metal nanoparticles: synthesis, characterization, and applications*. CRC press, 2001.

- [47] Todd M Squires and Stephen R Quake. Microfluidics: Fluid physics at the nanoliter scale. *Reviews of modern physics*, 77(3):977, 2005.
- [48] Thomas Pfohl, Frieder Mugele, Ralf Seemann, and Stephan Herminghaus. Trends in microfluidics with complex fluids. *ChemPhysChem*, 4(12):1291–1298, 2003.
- [49] David C Duffy, J Cooper McDonald, Olivier JA Schueller, and George M Whitesides. Rapid prototyping of microfluidic systems in poly (dimethylsiloxane). *Analytical chemistry*, 70(23):4974–4984, 1998.
- [50] Younan Xia and George M Whitesides. Soft lithography. *Angewandte Chemie International Edition*, 37(5):550–575, 1998.
- [51] Nano MicroChem. Su-8, negative tone photoresist formulations 50-100, 4 pages, feb. 2002.
- [52] Nano MicroChem. Su-8, negative tone photoresist formulations 2-25, 4 pages, feb. 2002.
- [53] MicroChem. Su-8, su-8 2000 permanent epoxy negative photoresist processing guidelines for su-8 2000.5, su-8 2002, su-8 2005, su-8 2007, su-8 2010 and su-8 2015, 5 pages.
- [54] MicroChem. Su-8, su-8 2000 permanent epoxy negative photoresist processing guidelines for su-8 2025, su-8 2035, su-8 2050 and su-8 2075, 5 pages.
- [55] J Cooper McDonald, David C Duffy, Janelle R Anderson, Daniel T Chiu, Hongkai Wu, Olivier JA Schueller, and George M Whitesides. Fabrication of microfluidic systems in poly (dimethylsiloxane). *ELECTROPHORESIS: An International Journal*, 21(1):27–40, 2000.
- [56] J Cooper McDonald and George M Whitesides. Poly (dimethylsiloxane) as a material for fabricating microfluidic devices. *Accounts of chemical research*, 35(7):491–499, 2002.
- [57] Janelle R Anderson, Daniel T Chiu, Rebecca J Jackman, Oksana Cherniavskaya, J Cooper McDonald, Hongkai Wu, Sue H Whitesides, and George M Whitesides. Fabrication of topologically complex three-dimensional microfluidic systems in pdms by rapid prototyping. *Analytical chemistry*, 72(14):3158–3164, 2000.
- [58] Shantanu Bhattacharya, Arindom Datta, Jordan M Berg, and Shubhra Gangopadhyay. Studies on surface wettability of poly (dimethyl) siloxane (pdms) and glass under oxygen-plasma treatment and correlation with bond strength. *Journal of microelectromechanical systems*, 14(3):590–597, 2005.

- [59] Hongzhi Wang, Hiroyuki Nakamura, Masato Uehara, Masaya Miyazaki, and Hideaki Maeda. Preparation of titania particles utilizing the insoluble phase interface in a microchannel reactor. *Chemical Communications*, (14):1462–1463, 2002.
- [60] Saif A Khan, Axel Günther, Martin A Schmidt, and Klavs F Jensen. Microfluidic synthesis of colloidal silica. *Langmuir*, 20(20):8604–8611, 2004.
- [61] S Krishnadasan, J Tovilla, R Vilar, et al. On-line analysis of cdse nanoparticle formation in a continuous flow chip-based microreactor. *Journal of Materials Chemistry*, 14(17):2655–2660, 2004.
- [62] Hiroyuki Nakamura, Yoshiko Yamaguchi, Masaya Miyazaki, Hideaki Maeda, Masato Uehara, and Paul Mulvaney. Preparation of cdse nanocrystals in a micro-flow-reactor. *Chemical Communications*, (23):2844–2845, 2002.
- [63] JM Köhler, J Wagner, and J Albert. Formation of isolated and clustered au nanoparticles in the presence of polyelectrolyte molecules using a flow-through si chip reactor. *Journal of Materials Chemistry*, 15(19):1924–1930, 2005.
- [64] Lung-Hsin Hung and Abraham Phillip Lee. Microfluidic devices for the synthesis of nanoparticles and biomaterials. *Journal of Medical and Biological Engineering*, 27(1):1, 2007.
- [65] Chia-Yen Lee, Chin-Lung Chang, Yao-Nan Wang, and Lung-Ming Fu. Microfluidic mixing: a review. *International journal of molecular sciences*, 12(5):3263–3287, 2011.
- [66] Timothy J Johnson, David Ross, and Laurie E Locascio. Rapid microfluidic mixing. *Analytical chemistry*, 74(1):45–51, 2002.
- [67] Aliaksandr Mialdun, Viktor Yasnou, Valentina Shevtsova, A Königer, W Köhler, D Alonso de Mezquia, and MM Bou-Ali. A comprehensive study of diffusion, thermodiffusion, and soret coefficients of water-isopropanol mixtures. *The Journal of chemical physics*, 136(24):244512, 2012.
- [68] Henry John Valentine Tyrrell and KR Harris. *Diffusion in liquids: a theoretical and experimental study*. Butterworth-Heinemann, 2013.
- [69] Herbert Oertel and Sebastian Ruck. *Bioströmungsmechanik: Grundlagen, methoden und phänomene*. Springer, 2012.
- [70] Jagannath Mazumdar. *Biofluid mechanics*. World Scientific, 2015.
- [71] Charles S Peskin. Numerical analysis of blood flow in the heart. *Journal of computational physics*, 25(3):220–252, 1977.

-
- [72] R Skalak, N Ozkaya, and T C Skalak. Biofluid mechanics. *Annual Review of Fluid Mechanics*, 21(1):167–200, 1989.
- [73] Nico Dingenouts. *Röntgenkleinwinkelstreuung als Methodik der Strukturanalyse teilgeordneter kolloidaler Systeme*. Shaker, 1999.
- [74] anton paar.com. <https://wiki.anton-paar.com/en/saxs-nanostructure-analysis/> Accessed: 2019-03-19.
- [75] Sara Mehdizadeh Taheri. *Herstellung und Charakterisierung von monodispersen sphärischen und kubischen Eisenoxid-Nanopartikeln und hochgeordneten Polymer-Nanokompositen*. PhD dissertation, University of Bayreuth, 2013.
- [76] Prof. Erich Sackmann and Prof. Rudolf Merkel. <http://www.biophy.de/?p=500>, Accessed: 2019-03-19.
- [77] J Teixeira. Small-angle scattering by fractal systems. *Journal of Applied Crystallography*, 21(6):781–785, 1988.
- [78] Christfried-Alexander Kurz and Anne Lorenz. *Das elektronenmikroskop (raster- und transmissionsmikroskopie)*, 2004.
- [79] Ludwig Reimer. *Transmission electron microscopy: physics of image formation and microanalysis*, volume 36. Springer, 2013.
- [80] Ernst Abbe. *Die Lehre von der Bildentstehung im Mikroskop: mit 57 Abbildungen und einem Bildnis Ernst Abbe's*. F. Vieweg, 1910.
- [81] Rainer Danz. Numerische apertur, immersion und förderliche vergrößerung. *Innovation*, 15:12–16, 2005.
- [82] Denise Barelmann-Kahlbohm. *Räumlich definierte Homo- und Blockcopolymer Nanokomposite*. PhD dissertation, University of Bayreuth, 2014.
- [83] Helmut Kohl and Ludwig Reimer. *Transmission electron microscopy: physics of image formation*. Springer, 2008.
- [84] Christian Colliex. *Elektronenmikroskopie: eine anwendungsbezogene Einführung*. Wiss. Verlag-Ges., 2008.
- [85] C Bliefert and J Kwiatkowski. *Kinetische analyse mit hilfe der uv-vis-spektrometrie*, 1991.
- [86] Wolfgang Häfner. *Praktikumsskript theoretischer versuch uv/vis teil 1*. 2010.

-
- [87] T. Lehmann. *Uv-vis-spektroskopie*, 1997.
- [88] Wolfgang Kaiser. *Kunststoffchemie für Ingenieure: von der Synthese bis zur Anwendung*. Carl Hanser Verlag GmbH Co KG, 2015.
- [89] AL Patterson. The scherrer formula for x-ray particle size determination. *Physical review*, 56(10):978, 1939.
- [90] Lubomir Spanhel. Colloidal zno nanostructures and functional coatings: A survey. *Journal of sol-gel science and technology*, 39(1):7–24, 2006.
- [91] Zhiqiang Niu, Qing Peng, Ming Gong, Hongpan Rong, and Yadong Li. Oleylamine-mediated shape evolution of palladium nanocrystals. *Angewandte Chemie International Edition*, 50(28):6315–6319, 2011.
- [92] Cecilia Sanna, Armida Sodo, Giuseppe Laguzzi, Giovanna Mancini, and Marina Bicchieri. Tert-butyl amine borane complex: an unusual application of a reducing agent on model molecules of cellulose based materials. *Journal of Cultural Heritage*, 10(3):356–361, 2009.
- [93] S Förster, L Apostol, and W Bras. Scatter: software for the analysis of nano-and mesoscale small-angle scattering. *Journal of Applied Crystallography*, 43(3):639–646, 2010.

List of Figures

2.1	Schematic illustrations of the top-down (A) and bottom-up (B) method to produce nanoparticles	6
2.2	LAMER model for the synthesis of monodisperse nanoparticles with primary stage (I), nucleation (II) and growth (III)	7
2.3	Schematic illustration of the nucleation-dependent formation enthalpy curve, whereby nucleation starts earlier at high temperatures (red curve) than at lower temperatures (blue curve)	10
2.4	Schematic representation of the energy level diagrams for macroscopic semiconductors (solids), nanoparticles and molecules. It can be seen that nanoparticles have an increased bandgap and quantified energy states	13
2.5	Schematic representation of the wurtzite crystal structure	14
2.6	Schematic illustrations of the difference between laminar flow (A) and turbulence (B)	15
2.7	Schematic illustrations of different channel designs with main focus on the possibilities of focusing the solutions in the microfluidic chip	17
2.8	Schematic illustrations of the difference between SAXS and WAXS	23
2.9	Schematic illustration of the scattering geometry	24
2.10	Schematic sketch of the construction of a transmission electron microscope	30
2.11	Schematic representation of the excitation of electrons by absorbance of photons of the energy $\Delta E^{[86]}$	32
3.1	Schematic illustration of the synthesis of the zinc oleate precursor: sodium oleate (1) reacts with zinc chloride (2) to zinc oleate (3) and sodium chloride (4).	33
3.2	Schematic illustration of the synthesis of the ZnO nanoparticles: zinc oleate (3) reacts with tetrabutylammonium hydroxide (5) to ZnO nanoparticles (6).	33
3.3	exemplary AutoCAD-sketches of the capillary holder: overall view (A) and top view (B) with marks of possible application methods (yellow - sample direction; red - SAXS; blue - WAXS; purple - UV-Vis; green - photoluminescence	35
3.4	graphical illustration of the differences between the temperature set at the capillary holder and the actual temperature measured at the capillary (A) and image of a infrared camera at a set temperature of 55 °C (B)	35

3.5	exemplary images of the capillary holder made of copper	36
3.6	Demonstration of the experimental setup of the microfluidic ZnO-nanoparticle synthesis: experimental setup at the laboratory based Ganesha (A), closeup view of the 3D-printed in situ capillary holder integrated with a heating copper tube (B), experimental setup at Petra III/DESY Hamburg at the beamline P03.	37
3.7	Stack-plots of the measured SAXS curves recorded in situ during the formation of the ZnO nanoparticles: A) $[\text{Zn}^{2+}]_{\text{prec}} = 160 \text{ mM}$, $T = 40 \text{ }^\circ\text{C}$; B) $[\text{Zn}^{2+}]_{\text{prec}} = 160 \text{ mM}$, $T = 50 \text{ }^\circ\text{C}$; C) $[\text{Zn}^{2+}]_{\text{prec}} = 53 \text{ mM}$, $T = 40 \text{ }^\circ\text{C}$; D) $[\text{Zn}^{2+}]_{\text{prec}} = 53 \text{ mM}$, $T = 50 \text{ }^\circ\text{C}$	38
3.8	Stack-plots of the SAXS curves recorded in situ during the first 300 - 400 s of the formation of the ZnO nanoparticles at the Petra III P03-beamline: A) $[\text{Zn}^{2+}]_{\text{prec}} = 53 \text{ mM}$, $T = 40 \text{ }^\circ\text{C}$; B) $[\text{Zn}^{2+}]_{\text{prec}} = 53 \text{ mM}$, $T = 50 \text{ }^\circ\text{C}$; C) $[\text{Zn}^{2+}]_{\text{prec}} = 160 \text{ mM}$, $T = 40 \text{ }^\circ\text{C}$; D) $[\text{Zn}^{2+}]_{\text{prec}} = 160 \text{ mM}$, $T = 50 \text{ }^\circ\text{C}$	40
3.9	Comparison of some measurements by both beamlines of the first five minutes of the ZnO nanoparticle formation. The black graphs are the SAXS-experiments measured at the Ganesha, the blue graphs are the SAXS-experiments measured at the DESY, PETRA III P03: A) $[\text{Zn}^{2+}]_{\text{prec}} = 160 \text{ mM}$, $T = 40 \text{ }^\circ\text{C}$, $t = 30\text{s}$, B) $[\text{Zn}^{2+}]_{\text{prec}} = 160 \text{ mM}$, $T = 40 \text{ }^\circ\text{C}$, $t = 60\text{s}$, C) $[\text{Zn}^{2+}]_{\text{prec}} = 160 \text{ mM}$, $T = 40 \text{ }^\circ\text{C}$, $t = 90\text{s}$, D) $[\text{Zn}^{2+}]_{\text{prec}} = 160 \text{ mM}$, $T = 40 \text{ }^\circ\text{C}$, $t = 120\text{s}$, E) $[\text{Zn}^{2+}]_{\text{prec}} = 160 \text{ mM}$, $T = 40 \text{ }^\circ\text{C}$, $t = 150\text{s}$, F) $[\text{Zn}^{2+}]_{\text{prec}} = 160 \text{ mM}$, $T = 40 \text{ }^\circ\text{C}$, $t = 180\text{s}$, G) $[\text{Zn}^{2+}]_{\text{prec}} = 160 \text{ mM}$, $T = 40 \text{ }^\circ\text{C}$, $t = 240\text{s}$, H) $[\text{Zn}^{2+}]_{\text{prec}} = 160 \text{ mM}$, $T = 40 \text{ }^\circ\text{C}$, $t = 300\text{s}$	41
3.10	Selected SAXS-curves of the ZnO nanoparticle formation at $40 \text{ }^\circ\text{C}$ with a Zn^{2+} -precursor concentration of $[\text{Zn}^{2+}]_{\text{prec}} = 160 \text{ mM}$ at different times measured at the Ganesha-beamline. The dotted red lines indicate the fits to the measured scattering curves.	42
3.11	Time evolution of the average ZnO nanoparticle radius determined from the fitted SAXS-curves for the different concentrations and temperatures investigated in the present study. (up to 240min, constant)	43
3.12	Time evolution of the average ZnO-nanoparticle radius over a period of 270 min	47
3.13	Three-dimensional plot of the time-dependent WAXS-curves recorded in situ during the formation of the ZnO nanoparticles with a concentration of 160 mM at $40 \text{ }^\circ\text{C}$ (A) and $50 \text{ }^\circ\text{C}$ (B).	48

3.14	Wide-angle diffraction data for the first 20 min frame (black symbols) and after ten hours (blue symbols). The solid line is the fit to determine the mean crystalline domain size $D = 0.65$ nm using a Gaussian peak shape.	49
3.15	Exemplary selection of two-dimensional time-dependent WAXS images of the in situ measurements of the formation of the ZnO nanoparticles with a concentration of $[\text{Zn}^{2+}]_{\text{prec}} = 160$ mM at 40 °C.	49
3.16	Three-dimensional plot of the UV-Vis spectra as a function of time recorded in situ during the formation of the ZnO nanoparticles with a $[\text{Zn}^{2+}]_{\text{prec}}$ -concentration of 160 mM at 40 °C (A) and 50 °C (B). The blue arrows indicate exemplary turning points, which determination was used to calculate the bandgap.	51
3.17	Time evolution of the band gap energy (A) and the diameter (B) determined from the UV-vis spectra (including a comparison with the SAXS data in B) of the ZnO nanoparticles with a concentration of 160 mM at different temperatures.	52
3.18	TEM-images of ZnO nanoparticles with an average particle diameter between 3 nm and 4 nm: A) $[\text{Zn}^{2+}]_{\text{prec}} = 53$ mM, $T = 40$ °C, B) $[\text{Zn}^{2+}]_{\text{prec}} = 160$ mM, $T = 40$ °C, C) $[\text{Zn}^{2+}]_{\text{prec}} = 53$ mM, $T = 50$ °C, D) $[\text{Zn}^{2+}]_{\text{prec}} = 160$ mM, $T = 50$ °C. [scale bar: 10 nm]	53
3.19	Schematic illustration of the synthesis of the palladium nanoparticles: $\text{Pd}(\text{acac})_2$ (1) reacts with OAm (2) and BTB (4) to Pd nanoparticles (6). . .	55
3.20	Photos of the experimental setup for Pd nanoparticle synthesis in a two-dimensional PDMS glass microfluidic chip with different heating methods for the tubes: A) self-made Kapton heating foils [with a close-up view of this (B)], C) copper heating block.	56
3.21	Image of a infrared camera at set temperature of 80 °C for reaching 70 °C as a reaction temperature for the Pd nanoparticle synthesis . . .	57
3.22	Demonstration of the experimental setup for the Pd nanoparticle synthesis in a closed quartz capillary in a heating cell (marked with a red frame) at the synchrotron. This photo was made and provided by Vanessa Leffler.	58
3.23	Stack-plots of selected measurement data of the SAXS-curves recorded in situ during the formation of the Pd nanoparticles at a temperature of 90 °C: A) $[\text{Pd}^{2+}]_{\text{prec}} = 16.41$ mM, $[\text{BTB}]_{\text{prec}} = 1.14$ M, $\Delta T = 3$ °C/min; B) $[\text{Pd}^{2+}]_{\text{prec}} = 16.41$ mM, $[\text{BTB}]_{\text{prec}} = 1.14$ M, $\Delta T = 6$ °C/min; C) $[\text{Pd}^{2+}]_{\text{prec}} = 16.41$ mM, $[\text{BTB}]_{\text{prec}} = 0.57$ M, $\Delta T = 3$ °C/min; D) $[\text{Pd}^{2+}]_{\text{prec}} = 16.41$ mM, $[\text{BTB}]_{\text{prec}} = 0.57$ M, $\Delta T = 6$ °C/min.	59

3.24	Stack-plots of selected measurement data of the SAXS-curves recorded in situ during the formation of the Pd nanoparticles at a temperature of 70 °C: A) $[Pd^{2+}]_{prec} = 16.41$ mM, $[BTB]_{prec} = 1.14$ M, $\Delta T = 3$ °C/min; B) $[Pd^{2+}]_{prec} = 16.41$ mM, $[BTB]_{prec} = 1.14$ M, $\Delta T = 6$ °C/min; C) $[Pd^{2+}]_{prec} = 16.41$ mM, $[BTB]_{prec} = 0.57$ M, $\Delta T = 3$ °C/min; D) $[Pd^{2+}]_{prec} = 16.41$ mM, $[BTB]_{prec} = 0.57$ M, $\Delta T = 6$ °C/min.	61
3.25	Selected SAXS-curves of the Pd-nanoparticle formation at 90 °C with $[Pd^{2+}]_{prec} = 16.41$ mM, $[BTB]_{prec} = 0.57$ M and $\Delta T = 3$ °C/min at different times. The red dotted lines indicate the fits to the measured scattering curves.	63
3.26	Time evolution of the average Pd-nanoparticle radius determined from the fitted SAXS-curves for different temperatures and heating rates with a $[BTB]_{prec} = 1.14$ M (A) and with a $[BTB]_{prec} = 0.57$ M (B). The black and green data indicate the syntheses with a heating rate $\Delta T = 3$ °C/min, the red and blue data the syntheses with a heating rate $\Delta T = 6$ °C/min. The black and red dotted data indicate the syntheses at 90 °C, the green and blue dotted data the syntheses at 70 °C. The solid lines indicate the calculation to the determined data.	63
3.27	Time evolution of the average Pd-nanoparticle radius determined from the fitted SAXS-curves for different BTB-concentrations and heating rates at a synthesis temperature of 70 °C (A) and 90 °C (B). The black and dark blue data indicate the syntheses with a heating rate $\Delta T = 3$ °C/min, the grey and light blue data the syntheses with a heating rate $\Delta T = 6$ °C/min. The black and grey dotted data indicate the syntheses with a high BTB-concentration $[BTB]_{prec} = 1.14$ M, the dark and light blue dotted data the syntheses with a low BTB-concentration $[BTB]_{prec} = 0.57$ M. The solid lines indicate the calculation to the determined data.	64
3.28	Time evolution of the average Pd-nanoparticle radius determined from the fitted SAXS-curves for different concentrations, heating rates and syntheses temperatures	67
3.29	TEM-images of Pd nanoparticles with an average particle diameter between 2.0 nm and 3.5 nm: A) $[Pd^{2+}]_{prec} = 16.41$ mM, $[BTB]_{prec} = 1.14$ M, T = 90 °C; $\Delta T = 3$ °C/min; B) $[Pd^{2+}]_{prec} = 16.41$ mM, $[BTB]_{prec} = 0.57$ M, T = 90 °C; $\Delta T = 3$ °C/min; C) $[Pd^{2+}]_{prec} = 16.41$ mM, $[BTB]_{prec} = 1.14$ M, T = 70 °C; $\Delta T = 3$ °C/min; D) $[Pd^{2+}]_{prec} = 16.41$ mM, $[BTB]_{prec} = 1.14$ M, T = 90 °C; $\Delta T = 6$ °C/min;	70
3.30	Schematic illustration of the experimental procedure to investigate thrombus formation	73

3.31	Exemplary sketch of one of the first channel designs (scale bar: 30 μm) for the stenosis experiments (A) and a corresponding screenshot of a video of an experiment, where mice blood was infused through the channel with a flow rate of 50 $\mu\text{L/h}$ (B). The arrow indicates the direction of the flow.	73
3.32	Screenshots of a video of an experiment where GFP positive blood cells were infused with a flow rate of 15 $\mu\text{L/h}$ through the microfluidic chip. The arrow indicates the direction of the flow.	74
3.33	Exemplary sketch of channel designs (Design V3) with larger tapers (scale bar: 10 μm)	75
3.34	A screenshot of a video of an experiment where fluorescent mouse blood was infused with a flow rate of 15 $\mu\text{L/h}$ through the microfluidic chip shows a blockage in the channel and, as a result of this, the PDMS under pressure. The arrow indicates the direction of the flow.	75
3.35	Sketch of channel designs with larger geometry and channel tapers (Design V4).	76
3.36	Screenshots of a high-speed camera video of an experiment where mouse blood was infused with a flow rate of 200 $\mu\text{L/h}$ through a microfluidic chip with a channel taper of 80 %. The arrow indicates the direction of the flow.	76
3.37	Comparison of two new channel designs with an angle at the channel tapering of 17° (A) and 55° (B), scale bars: 20 μm . This graphic was provided by Ruth Kranz.	77
3.38	Comparison of the area coverage of the two channel structures that led to the best experimental results, channel width of 100 μm (left) and 80 μm (right) with a channel tapering of 90 % each. These graphics were made and provided by Ruth Kranz.	77
3.39	Screenshots of a high-speed camera video of an experiment where mice blood was infused with a flow rate of 200 $\mu\text{L/h}$ through the microfluidic chip. The channel width was 80 μm , the channel height 30 μm . The arrow indicates the direction of the flow.	78
3.40	Simulation of a thrombus formation made and provided by Prof. Dr. S. Gekle. Order of images: from left to right and from top to bottom. The arrow indicates the direction of the flow.	78

3.41	Sketches of the excerpts of the designs of the microfluidic channels with a channel width of 80 μm and a longer plateau at the channel tapering (scale bar: 20 μm). From left (A) to right (D): plateau length = 8 μm (original), plateau length = 24 μm (factor 3), plateau length = 32 μm (factor 4) and plateau length = 40 μm (factor 5).	79
3.42	Demonstration of the experimental setup (A) and illustration of the bioreactor experiments (B). The lower photo of (A) and the lower sketch of (B) were made and provided by Dr. Markus Bender.	80
3.43	Exemplary sketch of one of the first bioreactor-designs (A) with two inlets, one with a filter (B), and two outlets. The total length of the channel is 2.5 cm, the total width 260 μm . Here, the channel width is divided into 3 areas (C) (scale bar: 50 μm).	81
3.44	Screenshots of a video of an early experiment in which megakaryocytes in the medium were infused through the bioreactor with a flow rate of 200 $\mu\text{l/h}$	82
3.45	Exemplary sketch of one of channel structures of the second design step (A) with more filters and just one channel outlet (B). The total length of the channel is 2.5 cm, the total width 500 μm . Here, the channel width is also divided into 3 areas. (C)	83
3.46	Screenshots of a high-speed camera video of a moment of an experiment where the string of beads-like cutting off process is studied. . . .	83
3.47	Summary of all new designed microfluidic bioreactor structures of this development step.	84
3.48	Sketches of the last design change during this work of the microfluidic bioreactor structures.	84
5.1	Sketches of the production of moldings by photolithography.	90
5.2	Sketches of the production of moldings by photolithography.	91
5.3	Presentation of the production of heating foils for microfluidic high temperature syntheses.	92

List of Tables

2.1	Examples of semiconductor nanoparticles	12
3.1	Summary of the synthesis parameters for the microfluidic ZnO-nanoparticle synthesis	34
3.2	Values for k_1 , k_{gr} , γ and $[ZnO]_{sat}$ for which the best fit to the experimental data was obtained	46
3.3	Summary of the results of the evaluation of the TEM-images	54
3.4	Summary of the synthesis parameters for the Pd-nanoparticle synthesis	55
3.5	Values for k_1 , k_{gr} , γ and $[Pd]_{sat}$ for which the best fit to the experimental data was obtained	68
5.1	List of manufacturers and purities of the used chemicals	88
5.2	Process parameters for the fabrication of microstructured 2D microfluidic channels	90

Scientific Contributions

Poster presentations

Chen, X.; Seibt, S.; Michaelis, M.; Förster, S.

International Association of Colloid and Interface Scientists,
Mainz (Germany), May, 24.-29., 2015

SAXS/WAXS/UV-Vis Life-Monitoring of Nanoparticle Nucleation and Growth

Güttler, T.; Michaelis, M.; Förster, S.

European Polymer Congress, Dresden (Germany), June, 21.-26., 2015

Block Copolymer Vesicles with Bioadhesion

Publications

Mehdizadeh Taheri, S.; Michaelis, M.; Friedrich, T.; Förster, B.; Drechsler, M.; Römer, F.

M.; Bösecke, P.; Narayanan, T.; Weber, B.; Rehberg, I.; Rosenfeldt, S.; Förster, S.

Self-assembly of smallest magnetic particles. *PNAS*, **2015**, 112, 14484-14489

Herbst, M.; Hofmann, E.; Förster, S.

Nucleation and growth of ZnO nanoparticles studied by in-situ microfluidic SAXS/WAXS/UV-Vis-experiments. *Langmuir*, **2019**, 35, 36, 11702–11709

Acknowledgements

An dieser Stelle möchte ich den Menschen danken, die mich im Rahmen dieser Arbeit unterstützt und somit zum Erfolg beigetragen haben.

An erster Stelle bedanke ich mich bei meinem Doktorvater Prof. Dr. Stephan Förster für die Bereitstellung des interessanten Themas, die Motivation und die vielen Anregungen. Ganz besonders möchte ich mich dafür bei dir bedanken, dass du es mir ermöglicht hast, "junges Familienleben" und "Doktorarbeit beenden" unter einen Hut zu bekommen. Das ist nicht unbedingt selbstverständlich und ich weiß es sehr zu schätzen!

Dr. Markus Bender danke ich für die sehr angenehme Zusammenarbeit, das Bereitstellen einiger Abbildungen und Grafiken und insbesondere für das "an die Hand nehmen" bei dem biologischen/medizinischen Themengebiet meiner Doktorarbeit.

Dr. Susanne Seibt und Dr. Miriam Hummel gilt mein besonderer Dank für ihre Freundschaften, die tolle Zeit und super Zusammenarbeit, die wir gemeinsam in "unserem Kellerlabor" hatten.

Dr. Sascha Ehlert und Vanessa Leffler - Danke für so, sooo vieles! Danke, dass ihr für mich während meiner Elternzeit am DESY SAXS-Messungen durchgeführt habt und meine geplanten Experimente genauso umgesetzt habt, dass ich super mit den Daten arbeiten konnte! Danke auch dafür, dass ihr mein "heißer Draht" nach Jülich gewesen seid!

Eddie Hofmann und Dr. Mathias Schlenk danke ich für die tolle Zusammenarbeit bei dem "Mäuse-Projekt" und den vielen gemeinsamen Messzeiten. Ein besonderer Dank geht an meinen "Lieblingsnachtschichtskollegen" Eddie für seine ruhige, gelassene Art und die super Mithilfe!

Dr. Stephan Hauschild - Danke für all deine Hilfe, ob bei den 3D-Druckern oder anderweitig, du bist super!

Familie Dr. Schröder - Sara und Jan...vielen lieben Dank für alles. Ohne euch, wäre es nie zu dieser Doktorarbeit gekommen. Ich habe von euch schon während meines Studiums unglaublich viel gelernt und bin sehr froh, euch kennen gelernt zu haben und bin sehr dankbar für eure Freundschaft!

Prof. Dr. Matthias Karg und Prof. Dr. Markus Retsch danke ich sehr für die wertvollen Tipps und die "Betreuung" während der Zeit mit einer größeren örtlichen Distanz zwischen Prof. Dr. Stephan Förster und mir.

Prof. Dr. S. Gekle danke ich für die gute Zusammenarbeit und die Bereitstellung der Simulationen für meine Doktorarbeit.

Ruth Kranz danke ich ebenso für die gute und vor allem sehr produktive Zusammenarbeit während ihrer Zeit bei unserer Kooperation und für die Bereitstellung einiger Abbildungen und Grafiken für meine Doktorarbeit.

Dr. Sabine Rosenfeld und Dr. Martin Dulle danke ich sehr für die nette Einweisung und Hilfestellung bei der Ganesha in Bayreuth.

Ich bedanke mich auch bei den technischen Angestellten Karl-Heinz Lauterbach, Julia Moßner, den Sekretärinnen in Jülich und Bayreuth Laura Diart, Jennifer Hennessy und Elisabeth Düngfelder für die Hilfe bei vielen alltäglichen Problemen im Labor oder im organisatorischen Bereich.

Bei Dr. Olga Isakin bedanke ich mich sehr für ihre Freundschaft, die Hilfe und Unterstützung beim morgendlichen Kampf mit dem TEM, die tollen Gespräche und unseren vielen Kaffe-Kakao- und Mittagessendates.

Tobias Güttler danke ich sehr für die angenehme Zusammenarbeit und für die tolle, wenn auch sehr kurze gemeinsame Zeit im Büro.

Kilian Krüger, Tobias Jurczyk, Dr. Maria Ritter und allen nicht namentlich genannten „ehemaligen Bayreuthern und Hamburgern“, den „Retschi's“ und den „Kargi's“ danke ich für die schöne Zeit in Bayreuth.

Meinen Eltern danke ich für ihre immer andauernde Unterstützung jeglicher Art und dass sie mir das Studium in Bayreuth ermöglicht haben.

Der größte Dank geht natürlich an Dirk und Paul, den zwei wichtigsten Menschen in meinem Leben, die größte Motivation für alles! Danke für die Unterstützung und das Aushalten meiner Launen bei den Höhen und Tiefen, die das Doktorandinnenleben mit sich gebracht hat.

Declaration/Eidesstattliche Erklärung

§9 Satz 2 Nr. 3 PromO BayNAT

Hiermit versichere ich eidesstattlich, dass ich die Arbeit selbstständig verfasst und keine anderen als die von mir angegebenen Quellen und Hilfsmittel benutzt habe (vgl. Art. 64 Abs 1 Satz 6 BayHSchG).

§9 Satz 2 Nr. 3 PromO BayNAT

Hiermit erkläre ich, dass ich die Dissertation nicht bereits zur Erlangung eines akademischen Grades eingereicht habe und dass ich nicht bereits diese oder eine gleichartige Doktorprüfung endgültig nicht bestanden habe.

§9 Satz 2 Nr. 4 PromO BayNAT

Hiermit erkläre ich, dass ich Hilfe von gewerblichen Promotionsberatern bzw. -vermittlern oder ähnlichen Dienstleistern weder bisher in Anspruch genommen habe noch künftig in Anspruch nehmen werde.

§9 Satz 2 Nr. 7 PromO BayNAT

Hiermit erkläre ich mein Einverständnis, dass die elektronische Fassung meiner Dissertation unter Wahrung meiner Urheberrechte und des Datenschutzes einer gesonderten Überprüfung unterzogen werden kann.

§9 Satz 2 Nr. 8 PromO BayNAT

Hiermit erkläre ich mein Einverständnis, dass bei Verdacht wissenschaftlichen Fehlverhaltens Ermittlungen durch universitätsinterne Organe der wissenschaftlichen Selbstkontrolle stattfinden können.

Ort, Datum

Unterschrift